

# ScholarWorks@GSU

## Detection And Characterization Of Hot Subdwarf Companions Of Massive Stars

Authors	Wang, Luqian
Citation	Wang, Luqian. "Detection And Characterization Of Hot Subdwarf Companions Of Massive Stars." 2019. Dissertation, Georgia State University. <a href="https://doi.org/10.57709/14972955">https://doi.org/10.57709/14972955</a>
DOI	<a href="https://doi.org/10.57709/14972955">https://doi.org/10.57709/14972955</a>
Download date	2026-04-10 23:46:26
Link to Item	<a href="https://hdl.handle.net/20.500.14694/12264">https://hdl.handle.net/20.500.14694/12264</a>

DETECTION AND CHARACTERIZATION OF HOT SUBDWARF COMPANIONS OF  
MASSIVE STARS

by

LUQIAN WANG

Under the Direction of Douglas R. Gies, PhD

ABSTRACT

Massive stars are born in close binaries, and in the course of their evolution, the initially more massive star will grow and begin to transfer mass and angular momentum to the gainer star. The mass donor star will be stripped of its outer envelope, and it will end up as a faint, hot subdwarf star. Here I present a search for the subdwarf stars in Be binary systems using the *International Ultraviolet Explorer*. Through spectroscopic analysis, I detected the subdwarf star in HR 2142 and 60 Cyg. Further analysis led to the discovery of an additional 12 Be and subdwarf candidate systems. I also investigated the EL CVn binary system, which is the prototype of class of eclipsing binaries that consist of an A- or F-type main sequence star and a low mass subdwarf. From spectroscopic analysis using both the *Hubble Space*

*Telescope* Cosmic Origins Spectrograph and the Apache Point Observatory *ARC* Echelle Spectrograph, I computed the system's radial velocities and orbital parameters. I combined these with photometric measurements from the *pt5m* telescope to obtain the physical properties of the system. The detection of these subdwarf stars only represents a small fraction of their population, and follow up spectroscopy will be needed to estimate their fundamental parameters. Such information will be compared with models to trace their evolutionary history.

INDEX WORDS: Stars: emission-line - Be, Stars: individual (HR 2142, HD 41335) - subdwarfs, Stars: individual (60 Cyg) - subdwarf, Stars: individual (EL CVn, HD 116608), Stars: binaries: spectroscopic, Stars: evolution

DETECTION AND CHARACTERIZATION OF HOT SUBDWARF COMPANIONS OF  
MASSIVE STARS

by

LUQIAN WANG

A Dissertation Submitted in Partial Fulfillment of the Requirements for the Degree of

Doctor of Philosophy

in the College of Arts and Sciences

Georgia State University

2019

Copyright by  
Luqian Wang  
2019

DETECTION AND CHARACTERIZATION OF HOT SUBDWARF COMPANIONS OF  
MASSIVE STARS

by

LUQIAN WANG

Committee Chair: Douglas R. Gies

Committee: Sébastien Lépine

Geraldine J. Peters

Mark Stockman

Russel White

Electronic Version Approved:

Office of Graduate Studies

College of Arts and Sciences

Georgia State University

August 2019

## DEDICATION

To my grandmother Yaohui Cheng and mother Feng Cheng. This dissertation is also dedicated to the memory of my grandfather, Peihua Zhang, who passed away before my graduation.

## ACKNOWLEDGMENTS

It is my great pleasure to thank the many people who made this dissertation possible. First, I would like to express my deepest appreciation and gratitude to my PhD advisor, Dr. Douglas Gies. His deep enthusiasm and passion for astronomy research inspired and encouraged me. For the past six years Dr. Gies has given me instructive guidance, helpful advice, and positive encouragement. I would not have been able to finish the dissertation without his help.

I would like to extend my sincere thanks to the project collaborators, Dr. Geraldine Peters, Kathryn Lester, Dr. Erika Grundstrom, Dr. Zhao Guo, Dr. Rachel Matson, Drew Chojnowski, and Dr. Ylva Götberg. I would like to thank the *pt5m* team members of Dr. Vik Dhillon, Dr. Tim Butterley, Dr. Stuart Littlefair, Dr. Richard Wilson, and the SMARTS team at GSU with members Dr. Todd Henry, Dr. Wei-Chun Jao, Leonardo Paredes, and Hodari James. I also would like to thank my committee members, Dr. Geraldine Peters, Dr. Russel White, Dr. Sébastien Lépine, and Dr. Mark Stockman.

Support for Program number GO-14778 was provided by NASA through a grant from the Space Telescope Science Institute, which is operated by the Association of Universities for Research in Astronomy, incorporated, under NASA contract NAS5-26555. I am grateful for additional support from NASA grant NNX10AD60G and National Science Foundation grant AST-1411654. Institutional support has been provided from the GSU College of Arts and Science and from the Research Program Enhancement fund of the Board of Regents of the

University System of Georgia, administered through the GSU office of the Vice President for Research and Economic Development. Based in part upon observations obtained with the Apache Point Observatory 3.5-meter telescope, which is owned and operated by the Astrophysical Research Consortium. *pt5m* is a collaborative effort between the Universities of Durham and Sheffield. The telescope is kindly hosted by the Issac Newton Group of Telescopes, La Palma.

Last, I would like to express my deep appreciation to my grandmother and mother who cared for me during difficult time. Their guidance and support helped me through the darkest moments.

## TABLE OF CONTENTS

ACKNOWLEDGMENTS . . . . .	v
LIST OF TABLES . . . . .	x
LIST OF FIGURES . . . . .	xi
LIST OF ABBREVIATIONS . . . . .	xix
<b>1 INTRODUCTION . . . . .</b>	<b>1</b>
1.1 Massive star evolution and the binary scenario . . . . .	1
1.2 Be stars and their formation scenarios . . . . .	2
1.3 Other approaches to search for sdO companions in Be binary systems	4
1.4 Population of Be stars in the local Galactic environment . . . . .	7
1.5 Motivation for searching sdO companions of rapidly rotating massive stars . . . . .	8
1.6 Outline of this work . . . . .	9
<b>2 THE HOT COMPANION AND CIRCUMBINARY DISK OF HR 2142</b>	<b>10</b>
2.1 HR 2142 binary system . . . . .	10
2.2 Radial velocities and orbital solution . . . . .	10
2.3 Search for the hot subdwarf companion . . . . .	20
2.4 Shell line features . . . . .	22
2.5 Disk models . . . . .	25
<b>3 DETECTION OF THE HOT SUBDWARF COMPANION OF 60 CYRGN1 FROM A SURVEY . . . . .</b>	<b>32</b>
3.1 A survey of <i>IUE</i> spectra of 6 Be stars . . . . .	32
3.2 Search for the UV flux of hot companions . . . . .	34

3.3	Implications of the detection of the companion of 60 Cyg . . . . .	40
4	DETECTION OF ADDITIONAL BE+SDO SYSTEMS FROM <i>IUE</i> SPECTROSCOPY . . . . .	45
4.1	Search for additional subdwarf companion of Be stars from <i>IUE</i> . . .	45
4.2	Search for sdO companions . . . . .	45
4.2.1	<i>Target selection from CCFs</i> . . . . .	45
4.2.2	<i>Detection criteria for Be+sdO systems</i> . . . . .	49
4.2.3	<i>Detection of the Be+sdO systems</i> . . . . .	51
4.3	Discussion of the candidate Be+sdO systems . . . . .	56
4.4	Population census of the identified Be+sdO candidate systems . . .	62
5	THE HOT SUBDWARF IN THE POST-MASS TRANSFER BINARY EL CVn . . . . .	67
5.1	Introduction . . . . .	67
5.2	Observations and data reduction . . . . .	69
5.2.1	<i>FUV HST/COS spectroscopy</i> . . . . .	70
5.2.2	<i>Optical APO/ARCES spectroscopy</i> . . . . .	71
5.2.3	<i>Optical PT5M light curves</i> . . . . .	72
5.3	Radial velocity measurements . . . . .	74
5.4	Light curve fit . . . . .	80
5.5	Orbital elements, masses, and radii . . . . .	83
5.6	Component Reconstructed Spectra and Physical Properties . . . . .	86
5.7	Evolutionary State of EL CVn . . . . .	96
6	CONCLUSIONS AND FUTURE WORK . . . . .	103
6.1	Implications of the candidate Be+sdO systems and follow-up ob- servations . . . . .	103
6.1.1	<i>Future FUV spectroscopy of Be+sdO candidate systems us- ing the HST/STIS</i> . . . . .	103

6.1.2	<i>Future optical spectroscopy from the SMARTS/CHIRON and APO/ARCES</i>	106
6.1.3	<i>Shell line variations in other Be+sdO systems</i>	108
6.1.4	<i>Resolving the problem of missing late-type Be stars in Be+sdO candidate systems</i>	110
6.2	Implications of the EL CVn binary system	112
6.3	Concluding remarks	114
REFERENCES		116
APPENDIX		127
A	SHELL LINE VARIATIONS IN HR 2142	127
B	SHELL EPISODE OF PLEIONE	145
C	NOTES ON INDIVIDUAL STARS IN THE <i>IUE</i> SUBDWARF SURVEY	148

## LIST OF TABLES

Table 2.1	Spectroscopic Observations of HR 2142 . . . . .	11
Table 2.2	Be Star Radial Velocities . . . . .	15
Table 2.3	Circular Orbital Elements . . . . .	20
Table 3.1	<i>IUE</i> Observations of Be Binary Systems . . . . .	34
Table 3.2	Adopted Orbital Elements . . . . .	36
Table 3.3	Co-moving Stars in the Vicinity of 59 Cyg and 60 Cyg . . . . .	43
Table 4.1	Stars with CCF S/N < 3 . . . . .	47
Table 4.2	<i>IUE</i> Observations of sample stars . . . . .	53
Table 4.3	Radial Velocity Measurements of Candidate sdO Components . . . . .	60
Table 5.1	Radial Velocity Measurements of EL CVn . . . . .	76
Table 5.2	Orbital elements of EL CVn . . . . .	80
Table 5.3	Epochs of A-star Inferior Conjunction . . . . .	85
Table 5.4	Physical Properties . . . . .	95
Table 5.5	$T_{\text{eff}}$ (spectrum) Estimates from Spectral Models . . . . .	96
Table 6.1	Target Table of 5 Be+sdO Candidate Systems For <i>SMARTS/CHIRON</i> . . . . .	108
Table 6.2	Physical properties of known Be+sdO binary systems . . . . .	111

## LIST OF FIGURES

- Figure 2.1 The *IUE* spectrum of HR 2142 with identifying number SWP 02355. 13
- Figure 2.2 The top panel shows the radial velocity plot of HR 2142, solid circles are RV measurements from the *IUE* and open circles are RVs from H $\alpha$  spectroscopy. Phase  $\phi = 0.0$  occurs when the Be star component is at superior conjunction from the observer. The bottom panel displays the velocity residuals between the observations and orbital solution. . . . . 14
- Figure 2.3 The shift-and-subtracted mean CCF computed from all 88 *IUE* spectra with a hot model spectrum over the range of 1150-1189 Å is plotted at bottom. I also grouped spectra into different phase ranges ( $\phi = 0.00-0.75$  and  $\phi = 0.75-1.00$ ) and plotted them above. The middle and top CCFs are offset by +0.02 and +0.04, respectively. A Gaussian fit was applied to the central peak signal and is shown as a dotted line. . . . . 23
- Figure 2.4 The top panel displays the individual spectra of Si II  $\lambda 1193.290$  as a function of the radial velocity, and each spectral flux is offset by its orbital phase. The depth of the absorption features relative to the continuum is shown by the scale in the upper right of the figure. The bottom panel shows the spectra in a gray scale format where black corresponds to the deepest absorption and white to the flux maximum. The lines of S III  $\lambda 1194$  appear shifted to the right. . . . . 26
- Figure 2.5 The top panel displays the individual spectra of H $\alpha$  as a function of the radial velocity, and each spectrum is offset by its orbital phase. The scale of the emission feature relative to the continuum is shown by the bar in the upper right of the figure. The bottom panel shows the spectra in a gray scale format. . . . . 27

Figure 2.6 This figure illustrates the circumstellar disk model of HR 2142. The Be star is indicated as the white circle in the center of the figure, the semi-major axis of the binary system is shown as the horizontal solid line connecting both stellar components, and each outer tick mark has a dimension of  $a/2$ . Based on method described in Grundstrom & Gies (2006) we estimated the Be disk size and plotted it in darkest gray. The lower density part of the disk extends beyond this radius and is shown in medium gray. Both components are smaller than their Roche-lobes, which are indicated by a dashed line. We adopted the tidal wake model of Ogilvie & Lubow (2002) and Bate et al. (2003) to plot the gap in the Be disk due to subdwarf's gravitational force (shown in white) and to estimate the location of the one-armed spiral tidal wake (shown as the solid line spiraling into the Be disk). Gas density enhancements due to the subdwarf's gravity are indicated by the thicker segment, and gas crossing the gap is shown by dotted lines with arrows to show their motion within the disk. At  $\phi = 0.95$ , the gas stream moving towards the Be star (away from us) is redshifted (primary shell phase); right after  $\phi = 0.0$ , the gas flow outwards from the Be disk (towards us) displays blueshifts (secondary shell phase). At  $\phi = 0.5$ , the gas stream moving away from the disk towards the L3 Lagrangian point is shown as a dotted line with an arrow. . . . . 31

Figure 3.1 The reconstructed secondary CCFs of the six Be binary systems derived from the assumed Doppler shifts of the secondary and a model hot reference spectrum ( $T_{\text{eff}} = 45$  kK). A detected peak is only seen in the case of 60 Cyg = HD 200310. . . . . 40

Figure 4.1 Example CCFs for two cases of hot component detection (top row) with several other cases where the peak is associated with the Be component (second and third rows). The top panels show the CCFs for HD 10516, a confirmed system with a hot subdwarf companion (Gies et al. 1998), and HD 58978, a confirmed system with a fainter subdwarf companion (Peters et al. 2008). The middle panels show how the spectrum of the emission-line star contributes more to the CCF for a hot star (HD 155806; O7.5 IIIe) than a mid-range temperature star (HD 174237; B4 IV(e)). The lower row illustrates how the CCF from the rapidly rotating Be component is usually very broad (HD 5394;  $V \sin i = 432$  km s $^{-1}$ ), but sometimes narrow (HD 120991;  $V \sin i = 70$  km s $^{-1}$ ). Examples of the CCFs for blue and red Doppler-shifted spectra are plotted as dotted and solid lines, respectively. The horizontal dashed lines indicate the  $S/N=3$  limit for detection. . . . . 50

Figure 4.2 CCF plots of eight Be+sdO binary candidates in the same format as Fig. 4.1. . . . . 57

Figure 4.3	CCF plots of four potential Be+sdO binary candidates in the same format as Fig. 4.1. . . . .	58
Figure 4.4	Histograms of the spectral type distributions of the full sample (solid line), those with no detections (dotted line), and those with known or candidate Be+sdO systems (line filled). . . . .	64
Figure 5.1	The rectified and normalized <i>HST</i> /COS spectrum observed on HJD 2457717.5985 in both short (B) and long (A) wavelength ranges. . . . .	71
Figure 5.2	The <i>APO</i> /ARCES spectrum observed on HJD 2457800.9918 of the single echelle order recording Mg II $\lambda$ 4481. . . . .	73
Figure 5.3	Plot of cross-correlation functions of EL CVn for each component from the <i>HST</i> /COS spectrum observed on HJD 2457717.5985. The CCF of the A-type component is plotted as a dotted line. The CCF of the pre-He WD companion is indicated as a solid line. . . . .	77
Figure 5.4	Radial velocity curve of EL CVn. In the top panel, the blue dots represent measurements from <i>HST</i> , green dots the measurements from <i>APO</i> , and published data from Maxted et al. (2014) appear as orchid dots. The bottom panel displays the difference between observed and calculated values. Orbital phase $\phi = 0.0$ is the epoch when the A-type star reaches inferior conjunction. . . . .	81
Figure 5.5	The top panel shows the light curve of EL CVn observed on the nights of 2013 May 5 and 15, and the ELC model fit is shown as a red solid line. The bottom panel displays the residuals between the observed and model light curves. . . . .	83
Figure 5.6	The top panel plots the epoch and orbit number of each data set in Table 3 and the corresponding, least-squares, linear fit. The derived slope (i.e., the orbital period) and intercept (global epoch) are listed in Table 2. The bottom panel displays the differences between the observed epochs and the fit. . . . .	86
Figure 5.7	The top panel shows a rebinned, low resolution version of the <i>HST</i> /COS spectrum in black observed on HJD 2457717.5985 with the sum of the model spectra for both components in orange. The bottom panel shows the individual model spectra as described in Section 5.6 (for metallicities of $[M/H] = 0.0$ and $-0.5$ for the A-star and subdwarf, respectively). . . . .	89

- Figure 5.8 The reconstructed spectrum of the pre-He WD component of EL CVn based upon the *HST*/COS short wavelength data. I plot the absolute flux of the reconstructed pre-He WD spectrum in black and the model spectrum in green ( $[M/H] = -0.5$ ; offset by  $+1.0 \times 10^{-13}$ ). . . . . 91
- Figure 5.9 The reconstructed spectrum of the pre-He WD component of EL CVn based upon the *HST*/COS long wavelength data. I plot the absolute flux of the reconstructed pre-He WD spectrum in black and the model spectrum in green ( $[M/H] = -0.5$ ; offset by  $+1.0 \times 10^{-13}$ ). . . . . 92
- Figure 5.10 The reconstructed spectrum of the A-star component of EL CVn based upon the *HST*/COS long wavelength data. I plot the absolute flux of the reconstructed A-star spectrum in black and the model spectrum in green ( $[M/H] = 0.0$ ; offset by  $+1.0 \times 10^{-13}$ ). . . . . 93
- Figure 5.11 The reconstructed spectra of EL CVn in the vicinity of the Mg II  $\lambda 4481$  line (from *APO*/ARCES data). The spectra were rebinned to a lower resolution of  $R \sim 17000$ . The top panel shows the rectified flux of the reconstructed spectrum of the A-star in black and the model spectrum in red ( $[M/H] = 0.0$ ; offset by  $-0.2$ ). The bottom panel displays the reconstructed spectrum of the pre-He WD in black and the model spectrum in blue ( $[M/H] = -1.0$ ; offset by  $-0.2$ ). Note that the He I  $\lambda 4471$  line predicted in the model is absent from the reconstructed spectrum of the subdwarf. . . . . 97
- Figure 5.12 The reconstructed spectra of EL CVn in the vicinity of  $H\beta$  (from *APO*/ARCES data). The spectra were rebinned to a lower resolution of  $R \sim 17000$ . The top panel shows the rectified flux of the reconstructed spectrum of the A-star in black and the model spectrum in red ( $[M/H] = 0.0$ ; offset by  $-0.2$ ). The bottom panel displays the reconstructed spectrum of the pre-He WD in black and the model spectrum in blue ( $[M/H] = -1.0$ ; offset by  $-0.2$ ). 98
- Figure 5.13 The reconstructed spectra of EL CVn in the vicinity of  $H\alpha$  (from *APO*/ARCES data). The spectra were rebinned to a lower resolution of  $R \sim 17000$ . The top panel shows the rectified flux of the reconstructed spectrum of the A-star in black and the model spectrum in red ( $[M/H] = 0.0$ ; offset by  $-0.3$ ). The bottom panel displays the reconstructed spectrum of the pre-He WD in black and the model spectrum in blue ( $[M/H] = -1.0$ ; offset by  $-0.3$ ). 99
- Figure 5.14 Evolutionary tracks from Althaus et al. (2013) in the  $(T_{\text{eff}}, R)$  plane for several assumed masses (labeled in units of  $M_{\odot}$ ). I plot the measured  $T_{\text{eff}}$  and  $R$  of the pre-He WD component (Sections 5.5, 5.6) as an open circle with the associated uncertainties. . . . . 101

Figure A.1 The top panel displays the individual spectra of S III  $\lambda 1200$  against the velocity, with each spectrum offset by its orbital phase. The depth of the absorption features relative to the continuum is shown by the scale on the upper right of the figure. The bottom panels showed the sample spectra interpreted in a gray scale format between deepest absorption (black) and maximum spectra flux (white). This line profile shows the complete shell line variations, which appear at  $\phi = 0.5$ , and they gradually develop strength and reach maximum near  $\phi = 0.95$ . Right after  $\phi = 0.0$ , the shell line features display a short-lived, blue-shifted component. . . . . 128

Figure A.2 The top panel displays the individual spectra of S II  $\lambda 1250$  against the velocity, with each spectrum offset by its orbital phase. The depth of the absorption features relative to the continuum is shown by the scale on the upper right of the figure. The bottom panels showed the sample spectra interpreted in a gray scale format between deepest absorption (black) and maximum spectra flux (white). This line profile shows the partial shell line variations, and only the primary shell line feature near  $\phi = 0.95$  is displayed. 129

Figure A.3 The top panel displays the individual spectra of Si II  $\lambda 1260$  against the velocity, with each spectrum offset by its orbital phase. The depth of the absorption features relative to the continuum is shown by the scale on the upper right of the figure. The bottom panels showed the sample spectra interpreted in a gray scale format between deepest absorption (black) and maximum spectra flux (white). This line profile shows the partial shell line variations, and only the primary shell line feature near  $\phi = 0.95$  is displayed. 130

Figure A.4 The top panel displays the individual spectra of Si II  $\lambda 1264$  against the velocity, with each spectrum offset by its orbital phase. The depth of the absorption features relative to the continuum is shown by the scale on the upper right of the figure. The bottom panels showed the sample spectra interpreted in a gray scale format between deepest absorption (black) and maximum spectra flux (white). This line profile shows the complete shell line variations, which appear at  $\phi = 0.5$ , and they gradually develop strength and reach maximum near  $\phi = 0.95$ . Right after  $\phi = 0.0$ , the shell line features display a short-lived, blue-shifted component. . . . . 131

- Figure A.5 The top panel displays the individual spectra of Si III  $\lambda 1299$  against the velocity, with each spectrum offset by its orbital phase. The depth of the absorption features relative to the continuum is shown by the scale on the upper right of the figure. The bottom panels showed the sample spectra interpreted in a gray scale format between deepest absorption (black) and maximum spectra flux (white). This line profile shows the complete shell line variations, which appear at  $\phi = 0.5$ , and they gradually develop strength and reach maximum near  $\phi = 0.95$ . Right after  $\phi = 0.0$ , the shell line features display a short-lived, blue-shifted component. . . . . 132
- Figure A.6 The top panel displays the individual spectra of Si II  $\lambda 1304$  against the velocity, with each spectrum offset by its orbital phase. The depth of the absorption features relative to the continuum is shown by the scale on the upper right of the figure. The bottom panels showed the sample spectra interpreted in a gray scale format between deepest absorption (black) and maximum spectra flux (white). This line profile shows the partial shell line variations, and only the primary shell line feature near  $\phi = 0.95$  is displayed. 133
- Figure A.7 The top panel displays the individual spectra of C II  $\lambda 1334, 1335$  against the velocity, with each spectrum offset by its orbital phase. The depth of the absorption features relative to the continuum is shown by the scale on the upper right of the figure. The bottom panels showed the sample spectra interpreted in a gray scale format between deepest absorption (black) and maximum spectra flux (white). This line profile shows shell line variations for both blueshifts near  $\phi = 0.5$  (Be star is at inferior conjunction relative to the observer), and extreme redshifts near  $\phi = 0.95$ . . . . . 134
- Figure A.8 The top panel displays the individual spectra of Si IV  $\lambda 1393$  against the velocity, with each spectrum offset by its orbital phase. The depth of the absorption features relative to the continuum is shown by the scale on the upper right of the figure. The bottom panels showed the sample spectra interpreted in a gray scale format between deepest absorption (black) and maximum spectra flux (white). This line profile shows the stellar wind features of the Be star, and the signature of primary absorption shell line features appear near  $\phi = 0.6 - 1.0$ . . . . . 135

Figure A.9 The top panel displays the individual spectra of Si IV  $\lambda 1402$  against the velocity, with each spectrum offset by its orbital phase. The depth of the absorption features relative to the continuum is shown by the scale on the upper right of the figure. The bottom panels showed the sample spectra interpreted in a gray scale format between deepest absorption (black) and maximum spectra flux (white). This line profile shows the stellar wind features of the Be star, and the signature of primary absorption shell line features appear near  $\phi = 0.6 - 1.0$  . . . . . 136

Figure A.10 The top panel displays the individual spectra of Si II  $\lambda 1526$  against the velocity, with each spectrum offset by its orbital phase. The depth of the absorption features relative to the continuum is shown by the scale on the upper right of the figure. The bottom panels showed the sample spectra interpreted in a gray scale format between deepest absorption (black) and maximum spectra flux (white). This line profile shows the partial shell line variations, and only the primary shell line feature near  $\phi = 0.95$  is displayed. 137

Figure A.11 The top panel displays the individual spectra of C IV  $\lambda 1548, 1550$  against the velocity, with each spectrum offset by its orbital phase. The depth of the absorption features relative to the continuum is shown by the scale on the upper right of the figure. The bottom panels showed the sample spectra interpreted in a gray scale format between deepest absorption (black) and maximum spectra flux (white). This line profile shows the stellar wind features of the Be star, the signature of primary absorption shell line features appear near  $\phi = 0.6 - 1.0$ , and blue-shifted absorption features appear near  $\phi = 0.5$ . . . . . 138

Figure A.12 The top panel displays the individual spectra of Al II  $\lambda 1670$  against the velocity, with each spectrum offset by its orbital phase. The depth of the absorption features relative to the continuum is shown by the scale on the upper right of the figure. The bottom panels showed the sample spectra interpreted in a gray scale format between deepest absorption (black) and maximum spectra flux (white). This line profile shows the partial shell line variations, and only the primary shell line feature near  $\phi = 0.95$  is displayed. 139

Figure A.13 The top panel displays the individual spectra of Al III  $\lambda 1854$  against the velocity, with each spectrum offset by its orbital phase. The depth of the absorption features relative to the continuum is shown by the scale on the upper right of the figure. The bottom panels showed the sample spectra interpreted in a gray scale format between deepest absorption (black) and maximum spectra flux (white). This line profile shows shell line variations for both blueshifts near  $\phi = 0.5$  (Be star is at inferior conjunction relative to the observer), and extreme redshifts near  $\phi = 0.95$ . . . . . 140

- Figure A.14 The top panel displays the individual spectra of Al III  $\lambda 1862$  against the velocity, with each spectrum offset by its orbital phase. The depth of the absorption features relative to the continuum is shown by the scale on the upper right of the figure. The bottom panels showed the sample spectra interpreted in a gray scale format between deepest absorption (black) and maximum spectra flux (white). This line profile shows shell line variations for both blueshifts near  $\phi = 0.5$  (Be star is at inferior conjunction relative to the observer), and extreme redshifts near  $\phi = 0.95$ . . . . . 141
- Figure A.15 The top panel displays the individual spectra of Fe III  $\lambda 1895$  against the velocity, with each spectrum offset by its orbital phase. The depth of the absorption features relative to the continuum is shown by the scale on the upper right of the figure. The bottom panels showed the sample spectra interpreted in a gray scale format between deepest absorption (black) and maximum spectra flux (white). This line profile shows shell line variations for both blueshifts near  $\phi = 0.5$  (Be star is at inferior conjunction relative to the observer), and extreme redshifts near  $\phi = 0.95$ . . . . . 142
- Figure A.16 The top panel displays the individual spectra of Mg II  $\lambda 2796$  against the velocity, with each spectrum offset by its orbital phase. The depth of the absorption features relative to the continuum is shown by the scale on the upper right of the figure. The bottom panels showed the sample spectra interpreted in a gray scale format between deepest absorption (black) and maximum spectra flux (white). This line profile shows the partial shell line variations, and only the primary shell line feature near  $\phi = 0.95$  is displayed. 143
- Figure A.17 The top panel displays the individual spectra of Mg II  $\lambda 2803$  against the velocity, with each spectrum offset by its orbital phase. The depth of the absorption features relative to the continuum is shown by the scale on the upper right of the figure. The bottom panels showed the sample spectra interpreted in a gray scale format between deepest absorption (black) and maximum spectra flux (white). This line profile shows the partial shell line variations, and only the primary shell line feature near  $\phi = 0.95$  is displayed. 144
- Figure B.1 The shell line variations of Pleione in UV . . . . . 147

## LIST OF ABBREVIATIONS

- APO: Apache Point Observatory
- ARCES: ARC Echelle Spectrograph
- BeSS: Be Star Spectra database
- BeXRB: Be X-Ray Binary
- BH: Black Hole
- CCF: Cross Correlation Function
- CFT: Coudé Feed Telescope
- COS: Cosmic Origins Spectrograph
- FUV: Far UV
- HD: Henry Draper Memorial Catalogue
- HR: Harvard Observatory Revised Photometry Catalogue
- HRD: Hertzsprung - Russell Diagram
- HST: Hubble Space Telescope
- HIRES: High Resolution Echelle Spectrometer
- IUE: International Ultraviolet Explorer
- KPNO: Kitt Peak National Observatory
- LWP: Low Wavelength range, Prime camera
- LWR: Low Wavelength range, Redundant camera
- MAST: Mikulski Archive for Space Telescopes

NS: Neutron Star

RV: Radial Velocity

sdO: subdwarf O-type star

STIS: Space Telescope Imaging Spectrograph

SWP: Short Wavelength Prime camera

UV: Ultra-Violet

WD: White Dwarf

# CHAPTER 1

## INTRODUCTION

### 1.1 Massive star evolution and the binary scenario

Growing evidence suggests that many massive stars were formed in binary systems that are destined to interact. Sana et al. (2012) conducted a binary population analysis of 71 O-type stars with masses between 8 to 15  $M_{\odot}$  from six nearby Galactic open clusters, and they reported that about 70% of the sample were binary systems and nearly 50% were close binaries. They also estimated that about 33% of the O-type stars are likely to lose their outer atmosphere through binary mass transfer before exploding to become hydrogen-deficient supernova (Type Ib, Ic, and IIb).

The binary system initially starts with two main-sequence type stars with one component that is more massive than the other. As the more massive star evolves away from the main sequence by hydrogen core exhaustion, the star inflates and then starts to transfer its mass and angular momentum to the less massive companion star through Roche-lobe overflow. This leads to the spin up of the companion star. The orbit shrinks until the two stars reach comparable masses, and then subsequent mass transfer expands the orbit again. This process continues until the former donor star has stripped off its outer atmosphere and left a core smaller than the size of its Roche-lobe. If the final stripped star has mass above the Chandrasekhar mass limit of 1.4  $M_{\odot}$ , then the star may explode to form neutron star in a X-ray binary. On the other hand, a stripped star with lower mass may shrink down to the extreme horizontal branch and become a faint, hot subdwarf (sdO) or a white dwarf (WD).

## 1.2 Be stars and their formation scenarios

Be stars are B-type, main-sequence stars that show or have shown hydrogen emission features in their optical spectra (Rivinius et al. 2013). The line emission features originate in a circumstellar disk around the Be star that is inherently variable on timescales from days to centuries. The disk features include the strong hydrogen emission lines, such as Balmer emission line formed from recombination, the continuum excess emission in IR and radio, as products of bound-free and free-free processes, and linear continuum polarization formed from the scattering of free electrons in the inner region of the Be disk. Their disks result from processes that are shedding the stellar angular momentum, and disk formation episodes may be linked to magnetic fields or pulsational mode beating in some Be stars (e.g.,  $\eta$  Cen and  $\mu$  Cen; Baade et al. 2016b), variations in the mass loss rate of the Be star, and binary interaction with a companion star (Rivinius et al. 2013). Be stars are generally fast rotating objects, with equatorial rotating speeds of  $> 70\%$  of the critical velocity, where gravitational and centrifugal forces balance at the equator. The formation of rapidly rotating Be stars could be due to a single star evolutionary channel leading to an increase in rotation at end of the main sequence. At the completion of burning hydrogen core, the core will start to contract and spin up, and this process leads to a re-distribution of angular momentum in the interior of the star. Angular momentum transfer outwards will cause the envelope to spin up close to the critical velocity (Meynet & Maeder 2002; Meynet et al. 2010). Alternatively, their formation may be due in some cases to past mass transfer in an interacting binary system (Pols et al. 1991; Shao & Li 2014) or as a result of binary merger (Vanbeveren &

Mennekens 2017).

Hypothetically, Be stars could be in binary systems with a relatively high mass companion, such as a neutron star or black hole (BH), or paired with low mass counterparts of white dwarfs or subdwarf stars. So far only one Be+BH binary has been detected (Casares et al. 2014). Be binaries are commonly observed in systems with a neutron star companion emitting high energy X-rays, and these binaries are known as Be X-ray binaries (BeXRBs). Reig (2011) reviewed all the known BeXRBs and confirmed 28 such systems in our galaxy. The kinematic features of BeXRBs and their interaction with Be disks were extensively studied by Waters & van Kerkwijk (1989) and Reig (2011). BeXRBs outside the local Galactic environment in the Magellanic Clouds were also investigated, and they display similar properties as those in the Milky Way (Coe et al. 2010; Haberl et al. 2012).

On the other side of the formation tale, Be stars should be abundant in binaries with a white dwarf or subdwarf companion. Observationally, only a few detection have been found so far. Such sdO stars are difficult to detect because they are usually lost in the glare of their massive companions as they contribute only a few percent of flux relative to their Be companion stars. The sdOs having small mass create only a small orbital reflex motion in the Be star. The orbital periods of such Be+sdO binary system span a range of one to ten months, and insufficient temporal coverage will prevent them from being detected. The subdwarfs are hot with  $T_{\text{eff}} \sim 50$  kK, so it is best to search for this type of remnant in the far-ultraviolet because they contribute relatively more flux there and their spectra are rich in highly ionized metallic lines. Such FUV spectroscopy investigations have led to the

detection of a subdwarf companion in three systems. Thaller et al. (1995) discovered the hot subdwarf companion of  $\phi$  Per using a Doppler tomography algorithm, which uses the radial velocities of the components to reconstruct their individual spectra. The highly ionized lines of the sdO star were clearly visible in the reconstructed secondary spectrum based on 16 Short Wavelength Prime (SWP) camera, high dispersion (H) spectra obtained with the *International Ultraviolet Explorer* (*IUE*). This discovery was confirmed by Gies et al. (1998) through *Hubble Space Telescope* (*HST*) spectroscopy, and their study suggested that the subdwarf companion has  $T_{\text{eff}} = 53 \pm 3$  kK,  $\log g = 4.2 \pm 0.1$ , mass ratio of  $q = 0.123$ , and  $f_2/f_1 \sim 16\%$ . Peters et al. (2008) combined optical spectra and 96 *IUE* spectra to confirm the binarity of FY CMa, and they detected the hot companion through analysis of cross-correlation functions (CCFs) of the UV spectra with that for a hot stellar template. Their study indicated that the secondary has  $T_{\text{eff}} = 45 \pm 5$  kK,  $\log g = 4.3 \pm 0.6$ ,  $q = 0.112$ ,  $f_2/f_1 \sim 4\%$ . A similar analysis was done by Peters et al. (2013) for 59 Cyg, and they reported that the detected companion has  $T_{\text{eff}} = 52.1 \pm 4.8$  kK,  $\log g = 5.0 \pm 1.0$ ,  $q = 0.096$ , and  $f_2/f_1 \sim 4\%$  based on a large set of 157 *IUE* spectra.

### 1.3 Other approaches to search for sdO companions in Be binary systems

Spectroscopy is the direct way to measure the radial velocities of a Be+sdO binary system and to reveal the spectroscopic features of both stellar components. Based on the insights from the three known Be+sdO binary systems (FY CMa, 59 Cyg, and  $\phi$  Per), the spectroscopic approach to search for such sdOs are limited mainly by several factors. First, the

sdO stars only contribute a few percent of flux relative to their Be companion star. The brightest subdwarf known is  $\phi$  Per, which has a flux ratio of  $f_2/f_1 \sim 16\%$ . The spectral features of the sdO are generally overwhelmed by its bright Be component. In one special case, the subdwarf alters the disk structure leading to absorption shell line variations in the circumstellar disk of the Be star HR 2142 (discussed in Chapter 2). Second, all the known Be+sdO binary systems have orbital periods that span a range from a month to less than a year. The sdO has small mass compared to its Be primary, with a mass ratio  $\sim 0.1$ . These factors lead to a small reflex orbital motion of the Be star, and thus a large set of spectroscopic observations is needed to cover the complete orbital phase and to trace the orbital motion of the system. Third, radial velocity measurements are needed to determine the orbital information of such binary systems. These are valuable, but the derived orbital parameters contain an unknown projection factor of  $\sin i$  where  $i$  is the orbital inclination. Lastly, the sdOs in known Be+sdO binaries all have  $T_{\text{eff}} \sim 50$  kK, and this limits the direct search for such sdOs to the far-UV regime of spectrum.

One of the three known Be+sdO binary systems is  $\phi$  Per. It is the first and only Be+sdO binary system where the orbit of the sdO has been visually imaged using the MIRC and VEGA instruments of the CHARA Array (Mourard et al. 2015). By tracking the orbital motion of the sdO through radial velocity fitting and image reconstruction of the Be star with its disk in the near-IR H-band, the study refined the orbital solution of this binary system, and estimated that the Be star and the sdO companion have masses of  $M_1 = 9.6 \pm 0.3 M_{\odot}$ ,  $M_2 = 1.2 \pm 0.2 M_{\odot}$ , respectively. They further reported that the flux ratio of the system

decreases from  $\sim 16\%$  in UV (Gies et al. 1998) to  $\sim 3.3\%$  in visible, and down to  $\sim 1.5\%$  in the H-band. The sdO companion in  $\phi$  Per is the brightest companion star has been detected so far in Be+sdO known binary systems. It will be more challenging to resolve and to image both components of such binary systems with relatively faint sdOs.

In addition to the spectroscopic and interferometric ways to search directly for the sdO companion of Be binary systems, another approach is to measure the spectral energy distribution of the Be disk in the IR and radio regime and search for evidence of spectral changes related to the truncation of the disk by the companion star. The circumstellar decretion disk of the Be star is heated by the stellar photosphere, and excess continuum emission from the disk is dominated by bound-free and free-free processes that create relatively more flux towards the mid-IR to radio regime. One of the widespread models to describe the properties of Be disks is the viscous decretion disk model by Lee et al. (1991) and Carciofi (2011). The model suggests that if the Be binary star has a companion, its gravitational force will truncate the outer radius of the circumstellar disk at a distance less than the binary separation. Each radial element of the disk contributes to the spectrum such that larger radii rings add more flux at longer wavelengths. Consequently, the truncation of the disk creates a turndown feature mainly observed in the IR and radio wavelength regime. Vieira et al. (2015) argued that the disk flux is characterized by a power law, i.e.  $F_\nu \propto \lambda^{-\kappa}$ , in which the exponent  $\kappa$  spans a range of  $-0.1$  (optically thin disk) to  $2.0$  (optically thick disk). If the disk is truncated by a companion star, then the SED will decline faster than expected by the power law and eventually attain a spectral slope  $\kappa$  of about 2. Klement et al. (2019, in preparation)

conducted a radio study to search for such an SED turndown among a sample of 57 Be stars, and they detected 24 stars displaying this feature. The advantage of this indirect way to search for companion stars of Be stars is that this approach mainly focuses on the flux distribution of the Be disk, and it is inclination independent. This presumably allows targets with low inclination angle to be detected through SED analysis if a companion is present. However, while this indirect search method is intended to constrain the presence of binary companions, the values of the companion remains unknown.

#### 1.4 Population of Be stars in the local Galactic environment

A theoretical framework was carried out by Schootemeijer et al. (2018), who used a He star evolutionary model to trace the path of the HD 10516 ( $\phi$  Per) system in the Hertzsprung-Russell diagram (HRD). They argued that these companions most likely spend nearly 90% of their post-mass transfer lifetime in a faint, quiescent, He-core burning stage, which makes them difficult to detect observationally. Götberg et al. (2018) conducted a theoretical study to estimate the physical properties of the sdO companions using the MESA evolutionary models. They argued that the features of the final stripped sdO companion stars depend on its progenitor mass and metallicity. The spectral signatures of such sdO stars could be traced from the optical He II  $\lambda 4686$  emission line and also the UV He II  $\lambda 1640$  emission profile. Boubert & Evans (2018) argued that if Be stars were formed under the post-mass-transfer scenario, a certain fraction of them had companions that exploded as supernovae and imparted a runaway speed with peculiar velocity  $> 40 \text{ km s}^{-1}$ . They conducted an

astrometric study of 632 Be stars using the *Gaia* DR1 data to estimate the population of runaway Be stars in the sample through binary evolution simulations. They reported that 17.5% of the stars are runaway stars, and the remaining 82.5% of the sample are bound binaries consisting of Be stars with sdO or WD companions.

### **1.5 Motivation for searching sdO companions of rapidly rotating massive stars**

Be stars are characterized by their near-critical rotational velocity. Many studies suggest that the fast rotation is the product of RLOF of mass accretion from a former mass donor star to the present Be star through transferring mass and angular momentum. In order to observationally confirm this growing hypothesis, I have conducted this dissertation work to search for hot subdwarf companions of rapidly rotating Be stars. These evolved systems are useful to trace the evolutionary processes of massive stars in binaries. It is important to constrain the number of such binary systems in the local galactic environment, through population synthesis models, and such results will provide insights about binary processes in massive stars. The binary frequency of massive stars directly affects the population of high-mass systems, such as Be+BH (Casares et al. 2014), BeXRBs, Wolf-rayet and O-type binaries (Vanbeveren et al. 1998), and double neutron star binaries.

The hot subdwarf companion star in such massive binary systems has stripped off its outer hydrogen envelope and left it as a helium core burning star. Massive helium remnant stars may explode as hydrogen-deficient supernovae (SNIb and SNIc). These subdwarfs could also be potential progenitors of neutron star and neutron star pairs can merge to create luminous

and energetic gravitational wave sources.

## 1.6 Outline of this work

Inspired by the large suggested population of sdO companion stars in binary systems, I expanded the search for additional subdwarfs using archival FUV spectra from the *IUE*. This led the detection of such a companion star in binary system of HR 2142 by Peters et al. (2016), and details are described in Chapter 2. Detection of the subdwarf in the 60 Cyg system from a sample of six known binaries is summarized in Chapter 3 (see also Wang et al. 2017). I also conducted an *IUE* survey of 264 stars to identify another twelve new candidate Be+sdO systems using CCFs with a model spectrum for a hot subdwarf, and details are reported in Chapter 4 (see also Wang et al. 2018b). Lastly, I investigated the spectral and photometric features of the eclipsing binary system EL CVn and determined its orbital and physical properties. EL CVn is the prototype of a class of binaries consisting of A- or F-type primaries and low mass, pre-He WDs. The work on EL CVn is presented in Chapter 5. I then summarize in Chapter 6 my work on searching for the subdwarf companions of massive stars, and I discuss proposed work for future follow-up studies to determine the orbital and stellar parameters of the Be+sdO candidate systems found in this work.

## CHAPTER 2

### THE HOT COMPANION AND CIRCUMBINARY DISK OF HR 2142

#### 2.1 HR 2142 binary system

HR 2142 (HD 41335) is a Be binary system with a spectral type of B1.5 IV-V nne, where the suffix “nn” refers to the very broad absorption features appearing in the spectra. Its spectroscopic emission features were first reported by Campbell (1895). Through radial velocity studies using optical spectra, Peters (1983) found that the system has an orbital period of  $P = 80.86$  days. A long-term photometric monitoring of Be stars conducted by Mennickent et al. (1998) showed that HR 2142 does not display significant long-term photometric variations, but they found evidence of a variation with a period of 344 days. An orbitally modulated absorption feature was observed by Peters (1971, 1972, 2001) in optical spectra in the Balmer line profiles and later in UV spectral lines from *IUE*. These “shell” features are possibly linked to the orbital motion of the He subdwarf in the binary system. Such a hot subdwarf companion star had been detected in the UV spectra for the Be systems  $\phi$  Per (Thaller et al. 1995), FY CMa (Peters et al. 2008), and 59 Cyg (Peters et al. 2013) using archival *IUE* spectra. Consequently, I initiated a search for the hot subdwarf companion star in HR 2142 by using UV and optical spectroscopy.

#### 2.2 Radial velocities and orbital solution

I began by collecting a diverse set of spectra to compute the Doppler shifts and radial velocities to revise the orbital solution of the system. I applied the radial velocity analysis to

four sets of data including 50 optical spectra from Peters (1983) observed at Lick observatory between 1969 and 1975, 88 archived *IUE* spectra from 1978 to 1995, 92 optical spectra obtained from the KPNO Coudé Feed telescope (CFT) between 1985 to 2008, and various optical spectra observed by amateur astronomers from the Be Star Spectra database (BeSS) project (Pollmann 2007; Neiner et al. 2011). The spectral sources, number of observations, resolving power and wavelength range of various spectrographs, observational dates, and names of the observers are tabulated in Table 2.1.

Table 2.1: Spectroscopic Observations of HR 2142

Code	Source	$N$	$\lambda/\Delta\lambda$	$\lambda$ Range (Å)	Dates (BY)	Observer
1	Lick 3 m	50	10000–15000	3200–4700	1969–1975	Peters
2	IUE	88	12000	1150–1950	1978–1995	Peters & others
3	KPNO CFT	84	12000–25000	6400–6700	1985–2001	Peters
4	KPNO CFT	8	9500	6430–7140	2004–2008	Grundstrom
5	BeSS	41	> 10000	6563:	2006–2015	various

I first downloaded 88 high resolution, and SWP HIRES FUV spectra, 49 LWR and LWP near UV spectra from MAST. These spectra were transformed onto uniform heliocentric wavelength grids and were rectified with respect to the relatively line-free continuum regions. The UV spectra record thousands of absorption lines due to the high ionization states of

metallic elements. The archival *IUE* UV spectra therefore display densely arranged and blended line features (see Figure 2.1). It is difficult to measure the Doppler shifts of line features for these UV spectra. I thus adopted the cross-correlation method from Zucker (2003) to compute the radial velocities of these FUV spectra. The cross correlation functions were calculated based on a maximum-likelihood approach, which is to find parameters that maximize the probability distribution of the Doppler shifts of the observed spectra. An similar approach is applied to constrain the uncertainty of the maximum position of the computed cross correlation functions. Because a large set of observations is available over a time span of about 50 years, the average observed spectrum is sufficient to represent the spectral features of the Be star. I thus used this average spectrum as the template to cross correlate with each individual spectrum. The beginning and ending regions and some deep line features formed in the interstellar medium or circumstellar disk of the Be star were excluded from the calculation. The calculated CCFs are very broad as we expected, because the Be star component has a large projected rotational broadening,  $V \sin i = 358 \text{ km s}^{-1}$  from Frémat et al. (2005). I thus adopted the technique described in Shafter et al. (1986) to compute the bisector velocities of the CCFs for the primary Be star through convolution using a pair of oppositely-signed Gaussian functions.

I also measured the radial velocities of the primary Be star using the  $H\alpha$  emission lines recorded in the KPNO spectra. These line features are strong emission lines formed in the circumstellar disk of Be star, and the emission wings represent gas closest to the central Be star. Likewise, I adopted the bisector technique again to measure the line wing velocity.

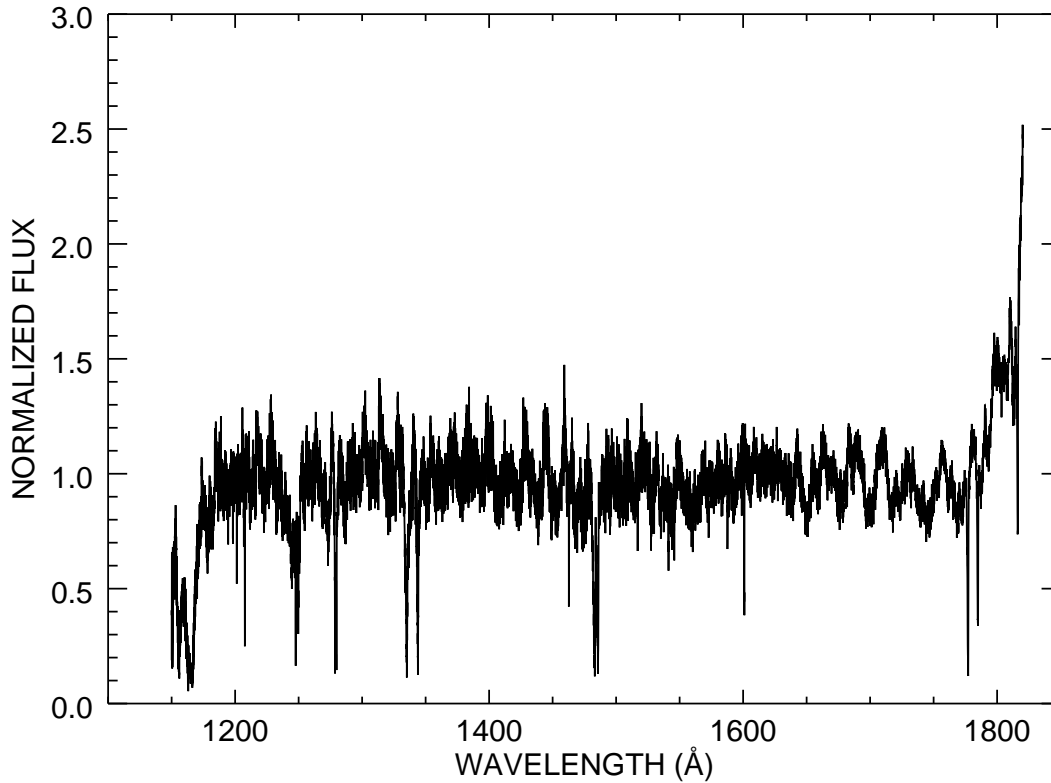


Figure 2.1: The *IUE* spectrum of HR 2142 with identifying number SWP 02355.

In order to combine all five sets of data together to revise the orbit of the binary system, I used the nonlinear, least-square method from Morbey & Brosterhus (1974) to obtain a preliminary orbital solution for each data set. Radial velocity measurements computed from the  $H\alpha$  emission line profile have the lowest errors, so I transformed the velocities to the frame of  $H\alpha$  measurements by adding a systemic velocity offset of  $\Delta\gamma = 28.68 \text{ km s}^{-1}$  to the computed *IUE* velocities and  $\Delta\gamma = 24.16 \text{ km s}^{-1}$  to the velocities reported in Peters (1983). In Table 2.2, I list the heliocentric Julian date of mid-exposure, the corresponding orbital phase, the final edited radial velocity with the associated uncertainty, velocity

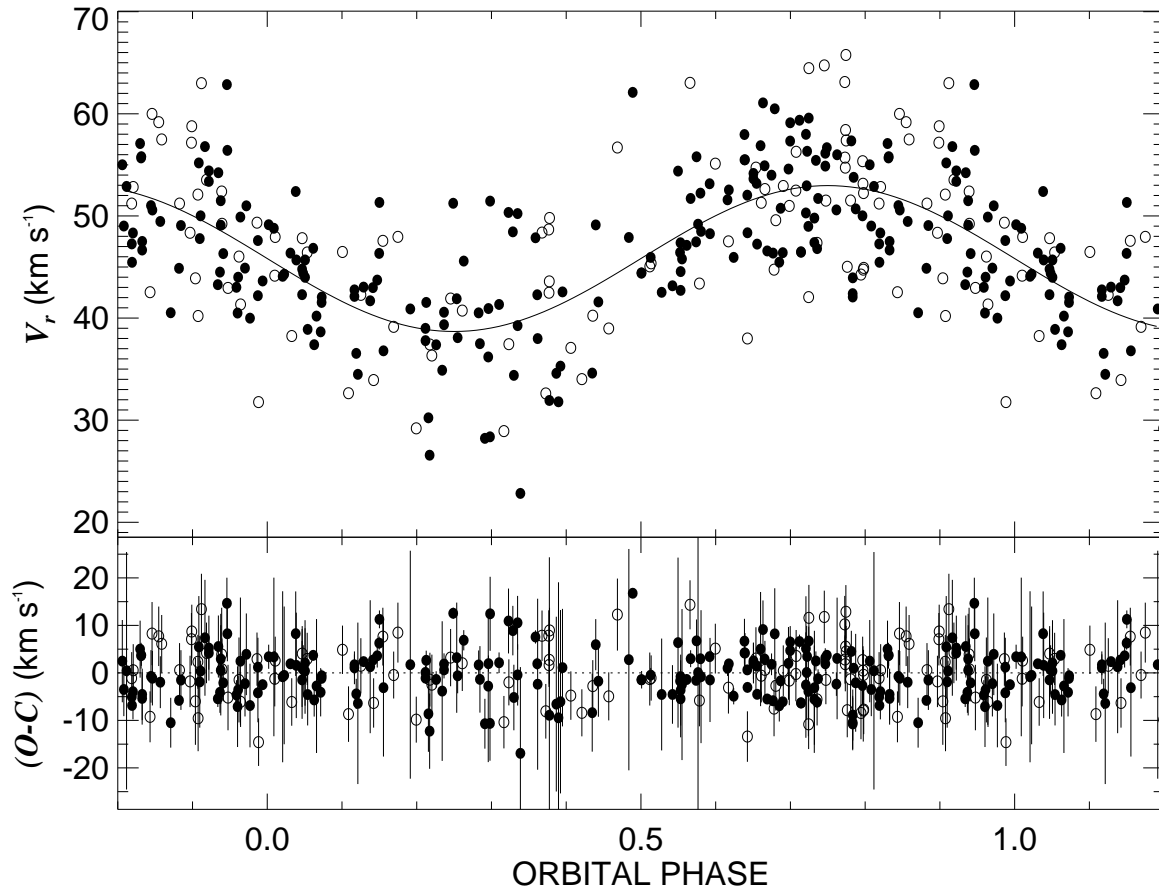


Figure 2.2: The top panel shows the radial velocity plot of HR 2142, solid circles are RV measurements from the *IUE* and open circles are RVs from H $\alpha$  spectroscopy. Phase  $\phi = 0.0$  occurs when the Be star component is at superior conjunction from the observer. The bottom panel displays the velocity residuals between the observations and orbital solution.

residual between observations and orbital solution, and a spectrum source code (spectrum number is given for the measurements from *IUE*). I then fitted the merged radial velocities using the least-squares method. The radial velocities are displayed in Figure 2.2, and the final calculated orbital solutions are collected in Table 2.3.

Table 2.2: Be Star Radial Velocities

Date HJD-2400000	Orbital Phase	$V_r$ km s <sup>-1</sup>	$\sigma$ (km s <sup>-1</sup> )	$O - C$ (km s <sup>-1</sup> )	Source Code <sup>a</sup>
40520.03	0.830	57.1	6.0	5.0	1
40527.05	0.917	56.8	12.2	7.4	1
40544.94	0.138	41.7	14.0	1.3	1
40572.94	0.484	47.9	23.3	2.8	1
40611.80	0.964	49.9	13.4	2.5	1
40637.73	0.285	37.5	7.0	-1.4	1
40638.63	0.296	36.2	16.0	-2.8	1
40659.61	0.555	45.8	15.9	-2.5	1
40850.04	0.908	55.2	10.7	5.5	1
40877.96	0.254	41.9	11.6	3.2	1
40903.92	0.574	55.8	4.5	6.7	1
40996.68	0.721	58.0	11.0	5.1	1
41200.04	0.234	34.9	14.7	-3.8	1
41228.06	0.580	48.5	14.0	-0.8	1
41236.04	0.679	60.5	9.6	8.2	1
41256.98	0.938	49.1	9.5	0.5	1
41256.98	0.938	51.5	8.4	2.9	1
41261.00	0.987	47.6	6.2	1.2	1
41261.00	0.987	42.2	10.7	-4.2	1
41346.70	0.047	44.8	8.2	1.0	1
41346.70	0.047	42.3	11.3	-1.5	1
41374.67	0.392	35.3	19.3	-6.1	1
41404.62	0.762	56.0	12.8	3.0	1
41406.63	0.787	50.7	10.3	-2.1	1
41433.65	0.121	34.5	17.0	-6.4	1
41590.04	0.054	38.9	6.5	-4.6	1
41591.00	0.066	40.2	14.1	-2.8	1
41614.94	0.362	38.0	18.0	-2.4	1
41616.96	0.387	34.6	18.4	-6.6	1
41643.98	0.721	50.3	11.1	-2.6	1
41644.89	0.732	47.4	11.3	-5.5	1
41644.90	0.732	49.8	12.0	-3.1	1
41936.02	0.330	34.4	6.9	-5.2	1
41975.00	0.812	52.9	25.0	0.5	1
41987.02	0.960	40.5	8.5	-7.1	1
41987.97	0.972	51.0	8.6	3.9	1
41990.95	0.009	48.8	16.7	3.4	1
41991.90	0.021	44.1	18.0	-0.8	1
41992.07	0.023	44.3	14.5	-0.5	1
42036.87	0.576	49.2	35.9	0.1	1
42083.73	0.156	36.8	14.5	-3.1	1
42149.65	0.970	44.9	6.9	-2.3	1
42312.02	0.977	40.0	8.8	-6.9	1
42316.97	0.038	52.4	8.9	8.3	1
42317.03	0.039	45.7	11.1	1.6	1
42317.98	0.051	45.7	9.0	2.1	1
42317.98	0.051	44.0	11.3	0.4	1
42318.97	0.063	37.4	3.5	-5.7	1
42682.01	0.550	54.4	17.9	6.4	1
42733.94	0.191	40.9	24.0	1.7	1
43742.3180	0.654	54.7	6.6	3.0	2355
43808.2337	0.468	56.7	7.6	12.3	3162
43844.1164	0.912	63.0	7.5	13.4	3505
43848.1808	0.962	46.0	8.9	-1.5	3537

Continued on next page

Table 2.2 – Continued from previous page

Date (HJD-2400000)	Orbital Phase	$V_r$ (km s <sup>-1</sup> )	$\sigma$ (km s <sup>-1</sup> )	$O - C$ (km s <sup>-1</sup> )	Source Code <sup>a</sup>
44167.1164	0.904	43.9	9.2	-6.0	6929
44169.9608	0.939	52.4	9.8	3.9	6961
44169.9955	0.939	49.2	6.5	0.8	6962
44172.0051	0.964	41.3	5.3	-6.1	6991
44173.7810	0.986	49.3	5.6	2.9	7007
44328.5142	0.899	57.2	5.5	7.1	8596
44328.5478	0.899	58.8	5.6	8.7	8597
44329.2100	0.907	52.1	5.7	2.3	8604
44330.1423	0.919	53.5	6.4	4.2	8616
44332.4697	0.947	43.0	6.9	-5.2	8637
44483.8703	0.819	51.2	5.5	-1.1	9978
44485.8594	0.843	42.5	5.4	-9.2	9992
44511.0631	0.155	47.6	6.1	7.6	10240
44533.7852	0.436	40.2	5.5	-2.8	10436
44612.3243	0.406	37.1	5.1	-4.8	10993
44616.4285	0.457	39.0	5.1	-4.9	11026
44661.2357	0.011	47.9	5.0	2.6	13359
44867.9669	0.566	63.0	5.2	14.3	15054
44891.3648	0.855	59.2	6.3	7.7	15255
44920.7181	0.218	37.4	5.7	-1.4	15477
44972.5984	0.859	57.5	6.1	6.1	15932
44974.5335	0.883	51.2	5.7	0.6	15955
44975.6692	0.897	48.4	5.4	-1.8	15977
45042.6617	0.725	64.5	6.9	11.6	16526
46121.7891	0.062	46.8	1.1	3.7	3
46122.6951	0.073	41.5	1.1	-1.1	3
46122.7103	0.073	42.0	1.3	-0.6	3
46152.6593	0.443	41.6	7.5	-1.7	3
46338.9463	0.745	64.7	5.5	11.8	26809
46734.9250	0.639	55.5	4.2	4.2	3
46737.7984	0.675	54.0	2.3	1.8	3
46820.6364	0.699	51.0	5.2	-1.6	30156
46823.6438	0.736	47.4	5.5	-5.6	30179
46824.5968	0.747	51.5	5.1	-1.5	30188
46826.6402	0.773	63.1	6.0	10.2	30207
46826.6638	0.773	55.7	5.1	2.8	30208
46826.6978	0.773	54.7	5.7	1.8	30209
46826.7272	0.774	58.4	5.7	5.5	30210
46826.7616	0.774	65.8	5.6	12.9	30211
46826.7876	0.775	57.4	5.4	4.5	30212
46828.5744	0.797	55.4	4.9	2.7	30228
46828.6136	0.797	53.1	5.1	0.5	30229
46828.6442	0.797	44.7	6.5	-7.9	30230
46828.6690	0.798	52.2	5.3	-0.4	30231
46828.6952	0.798	44.9	5.2	-7.7	30232
46830.5249	0.821	52.8	5.5	0.6	30250
46832.5591	0.846	60.0	6.7	8.3	30263
46875.5064	0.377	48.7	5.3	7.8	30580
46875.5362	0.377	42.5	4.6	1.6	30581
46875.5655	0.377	43.6	5.0	2.7	30582
46875.5925	0.378	49.8	4.8	8.9	30583
46901.6395	0.700	57.3	3.0	4.7	3
46901.6452	0.700	59.1	3.4	6.5	3
46902.6503	0.712	59.4	1.5	6.6	3
46903.6545	0.725	59.6	3.0	6.7	3
46905.6139	0.749	56.7	1.1	3.7	3

Continued on next page

Table 2.2 – Continued from previous page

Date (HJD-2400000)	Orbital Phase	$V_r$ (km s <sup>-1</sup> )	$\sigma$ (km s <sup>-1</sup> )	$O - C$ (km s <sup>-1</sup> )	Source Code <sup>a</sup>
46918.6402	0.910	47.8	9.7	-1.9	3
46919.6238	0.922	53.4	3.5	4.2	3
46919.6287	0.922	54.4	6.8	5.2	3
46920.6564	0.935	54.2	6.5	5.6	3
47030.9707	0.298	28.4	7.9	-10.6	3
47030.9854	0.298	51.5	7.8	12.4	3
47032.9747	0.323	50.3	6.8	10.9	3
47033.9595	0.335	50.2	5.7	10.6	3
47033.9629	0.335	39.3	6.5	-0.4	3
47103.9017	0.199	29.2	4.8	-9.8	32224
47141.6472	0.666	52.6	6.1	0.6	32507
47169.4943	0.010	44.1	5.8	-1.2	32687
47172.4692	0.047	47.8	5.8	4.1	32701
47198.4327	0.368	48.4	5.3	7.8	32874
47215.4720	0.578	43.4	5.4	-5.8	32970
47258.3965	0.109	32.6	5.8	-8.7	33220
47414.0776	0.033	38.2	5.0	-6.1	34212
47422.9379	0.142	33.9	5.2	-6.3	34267
47464.9085	0.661	51.3	5.6	-0.6	34633
47469.8194	0.722	53.0	9.8	0.1	3
47470.0047	0.724	49.0	9.4	-3.9	3
47470.8213	0.734	55.4	2.0	2.5	3
47471.0573	0.737	51.7	2.0	-1.2	3
47471.8378	0.747	56.1	2.0	3.2	3
47471.8404	0.747	54.9	1.5	1.9	3
47473.0386	0.761	50.6	2.5	-2.4	3
47484.8542	0.907	40.2	6.9	-9.5	34770
47533.7509	0.512	45.1	5.6	-1.3	35282
47550.5978 <sup>b</sup>	0.720	33.7	5.5	-19.1	35400
47556.6147	0.794	44.3	5.5	-8.4	35456
47560.6629	0.844	51.0	5.5	-0.7	3
47560.8172	0.846	50.6	5.7	-1.1	3
47561.6730	0.857	49.5	5.5	-2.0	3
47572.3104	0.988	31.8	5.0	-14.6	35551
47607.3133	0.421	34.0	5.0	-8.4	35833
47636.6277	0.783	42.4	5.6	-10.4	3
47636.6330	0.783	42.1	5.5	-10.8	3
47636.6381	0.783	43.9	5.4	-8.9	3
47638.6422	0.808	49.0	5.6	-3.5	3
47639.6267	0.820	48.3	5.8	-4.0	3
47640.6235	0.833	46.7	5.5	-5.4	3
47640.6276	0.833	47.5	5.4	-4.5	3
47789.9438	0.678	44.7	5.8	-7.5	37091
47871.8559	0.690	52.9	5.3	0.5	37795
47938.4644	0.514	45.4	4.8	-1.1	38198
47939.6030	0.528	42.5	11.8	-4.5	3
47940.7746	0.542	43.2	6.2	-4.5	3
47941.6557	0.553	42.7	8.1	-5.5	3
47941.6606	0.553	44.5	7.5	-3.6	3
47945.4140	0.600	55.1	5.2	5.1	38227
47981.7112	0.048	44.4	5.1	0.7	3
47983.6008	0.071	38.6	5.1	-4.1	3
48121.9663	0.782	57.4	4.3	4.5	3
48123.9556	0.806	55.0	8.7	2.5	3
48124.9817	0.819	47.3	1.5	-5.1	3
48125.0065	0.819	45.5	0.9	-6.8	3

Continued on next page

Table 2.2 – Continued from previous page

Date (HJD-2400000)	Orbital Phase	$V_r$ (km s <sup>-1</sup> )	$\sigma$ (km s <sup>-1</sup> )	$O - C$ (km s <sup>-1</sup> )	Source Code <sup>a</sup>
48125.9833	0.831	55.7	2.7	3.6	3
48126.0140	0.832	55.8	2.3	3.7	3
48228.7021	0.101	46.5	5.1	4.9	40252
48230.6937	0.125	42.3	5.8	1.5	40271
48234.7019	0.175	48.0	6.3	8.5	40292
48313.6160	0.150	51.3	1.9	11.3	3
48318.5967	0.212	39.0	1.4	0.1	3
48318.6029	0.212	37.8	1.2	-1.1	3
48319.7591	0.226	37.4	1.7	-1.4	3
48320.6062	0.236	40.6	2.3	1.9	3
48320.6093	0.237	39.4	1.8	0.6	3
48321.6023	0.249	51.2	1.2	12.6	3
48351.4009	0.617	47.5	5.5	-3.1	41292
48353.4552	0.642	38.0	5.3	-13.4	41312
48356.5255	0.680	49.6	5.2	-2.7	41329
48514.9599	0.638	58.0	4.7	6.7	3
48514.9619	0.639	55.5	2.9	4.2	3
48515.9288	0.650	53.6	4.2	2.0	3
48515.9315	0.650	54.2	3.9	2.5	3
48516.9660	0.663	61.1	6.1	9.1	3
49058.7301	0.359	47.9	1.4	7.6	3
49276.7565	0.053	46.4	5.5	2.9	48925
49335.5789	0.780	51.5	6.7	-1.3	49589
49374.4579	0.261	40.7	5.8	2.0	49862
49379.4985	0.323	37.4	4.8	-2.0	49900
49383.4999	0.373	32.6	5.8	-8.1	49918
49443.6959	0.117	42.1	3.5	1.1	3
49443.6977	0.117	42.8	2.2	1.7	3
49444.6856	0.129	43.0	0.8	2.4	3
49445.7002	0.141	43.0	1.2	2.7	3
49658.8770	0.776	45.0	5.7	-7.9	52713
49690.6816	0.169	39.1	4.9	-0.4	52974
49694.8170	0.220	36.3	6.3	-2.5	53010
49696.8457	0.245	41.9	6.0	3.2	53030
49783.5320	0.317	28.9	5.5	-10.4	54053
49816.5209	0.724	42.0	5.2	-10.8	54339
49976.9670	0.707	52.5	5.7	-0.2	55942
49976.9934	0.708	56.3	5.5	3.6	55943
50445.7157	0.501	44.4	1.1	-1.4	3
50446.7308	0.513	45.9	1.5	-0.5	3
50449.9064	0.552	46.4	1.9	-1.7	3
50449.9519	0.553	47.4	1.6	-0.8	3
50450.6275	0.561	47.1	1.0	-1.4	3
50451.6439	0.574	47.5	0.9	-1.6	3
51191.8840	0.722	56.3	0.6	3.5	3
51196.9206	0.785	53.8	0.9	1.0	3
51502.9245	0.566	51.7	1.8	3.0	3
51503.9888	0.580	52.2	0.7	3.0	3
51504.9810	0.592	53.1	0.6	3.4	3
51507.0622	0.618	52.5	0.6	1.9	3
51509.0572	0.642	52.0	0.9	0.6	3
51510.0615	0.655	53.2	0.9	1.5	3
51510.9336	0.665	54.9	0.7	2.9	3
51913.6433	0.643	48.4	0.5	-3.1	3
51914.6872	0.655	47.2	0.8	-4.5	3
51915.7806	0.669	46.6	0.8	-5.5	3

Continued on next page

Table 2.2 – Continued from previous page

Date (HJD-2400000)	Orbital Phase	$V_r$ (km s <sup>-1</sup> )	$\sigma$ (km s <sup>-1</sup> )	$O - C$ (km s <sup>-1</sup> )	Source Code <sup>a</sup>
53291.9354	0.677	46.4	1.1	-5.9	4
53292.9944	0.690	46.4	1.0	-6.1	4
53294.9640	0.714	46.5	0.9	-6.3	4
53294.9696	0.714	46.4	0.9	-6.3	4
54000.5828	0.435	34.6	8.2	-8.4	5
54020.9788	0.687	50.8	1.3	-1.7	4
54024.9341	0.736	46.8	1.3	-6.1	4
54041.5544	0.941	46.3	3.9	-2.1	5
54360.6253	0.885	49.1	6.3	-1.5	5
54365.6499	0.947	56.4	5.8	8.2	5
54366.6335	0.959	43.0	3.1	-4.6	5
54379.6041	0.119	36.5	3.2	-4.4	5
54387.5470	0.217	26.6	7.9	-12.3	5
54390.5816	0.255	38.1	3.7	-0.6	5
54396.5591	0.329	48.4	5.2	8.9	5
54405.5336	0.440	49.1	5.4	5.9	5
54468.3319	0.216	30.2	8.0	-8.6	5
54478.2873	0.339	22.8	18.2	-16.9	5
54504.2894	0.660	56.9	12.0	5.0	5
54506.3162	0.685	45.5	3.3	-6.9	5
54507.3105	0.697	54.6	7.7	2.0	5
54521.3459	0.871	40.5	5.2	-10.5	5
54527.4288	0.946	62.9	5.4	14.7	5
54555.3556	0.291	28.2	5.2	-10.7	5
54562.3347	0.377	31.9	33.3	-8.9	5
54563.3236	0.390	31.8	28.5	-9.5	5
54764.9840	0.882	44.9	0.6	-5.8	4
54774.0358	0.994	43.6	0.8	-2.5	4
54822.4689	0.592	48.3	8.9	-1.5	5
54879.3956	0.296	40.9	1.7	2.0	5
54887.4120	0.395	42.6	12.4	1.1	5
55576.4532	0.911	50.0	2.2	0.4	5
55988.3921	0.002	49.1	2.5	3.4	5
56000.3542	0.150	46.3	1.4	6.3	5
56271.5006	0.501	44.4	1.8	-1.4	5
56295.4159	0.796	50.0	3.9	-2.7	5
56630.1881	0.934	43.3	1.7	-5.4	5
56647.4494	0.147	43.7	2.5	3.6	5
56685.3676	0.616	51.6	1.6	1.0	5
56686.0369	0.624	45.9	1.7	-4.9	5
56711.3368	0.937	44.5	4.3	-4.1	5
56713.3043	0.961	44.0	2.9	-3.6	5
56733.6663	0.213	41.5	2.0	2.7	5
56739.3400	0.283	40.5	3.0	1.7	5
56741.5539	0.310	41.3	2.2	2.1	5
56745.6829	0.361	42.3	1.3	1.9	5
56998.7604	0.489	62.1	0.7	16.8	5
57042.6163	0.031	46.4	0.7	1.9	5
57061.3817	0.263	45.6	2.1	6.9	5

<sup>a</sup> Source code of the observations were listed in Table 2.1; *IUE* spectrum number is given for the measurements from *IUE*.

<sup>b</sup> This discrepant measurement is assigned a weight of 0.0 for the radial velocity fitting.

Table 2.3: Circular Orbital Elements

Element	This Study	Peters (1983)
$P$ (days)	$80.913 \pm 0.018$	$80.860 \pm 0.005$
$T_{sc}$ (HJD-2400000)	$46845.0 \pm 1.0$	$41990.5 \pm 1.1$
$K_1$ ( $\text{km s}^{-1}$ )	$7.1 \pm 0.5$	$9.4 \pm 0.9$
$\gamma(\text{H}\alpha)$ ( $\text{km s}^{-1}$ )	$45.8 \pm 0.4$	...
$f(m)$ ( $M_\odot$ )	$0.0031 \pm 0.0006$	$0.007 \pm 0.002$
$a_1 \sin i$ ( $10^6$ km)	$7.9 \pm 0.5$	$10.4 \pm 1.0$
rms ( $\text{km s}^{-1}$ )	5.8	4.1

### 2.3 Search for the hot subdwarf companion

I adopted a cross-correlation method to search for the spectral features of the hot subdwarf companion. I first constructed a model spectrum of the hot subdwarf star using the non-LTE TLUSTY/SYNSPEC atmospheric models from Lanz & Hubeny (2003) with  $T_{\text{eff}} = 45$  kK,  $\log g = 4.75$ , solar abundances, and no rotational broadening. Because the hot subdwarf contributes more flux at shorter wavelengths, I thus restricted the search to the far UV range of 1150 – 1189 Å. I excluded the broad C III  $\lambda 1176$  line feature from the Be star in the spectrum. I cross-correlated the constructed model spectrum with the selected region of the observed spectra, and then the average CCF was subtracted to remove the signal contribution from the Be component star. In order to enhance the spectral signal of the

subdwarf star appearing in the computed CCFs, I shifted the individual difference CCF to the expected Doppler reference frame of the companion. To do this I obtained the mass ratio of the binary system using the mass function obtained from the radial velocity curve fitting ( $f(m) = (M_2 \sin i)^3 / (M_1 + M_2)^2$ , see Table 2.3) and assumed that  $M_1 = 10.5 M_\odot$  and that the system has an orbital inclination of  $i = 85^\circ$ . I then used the calculated mass ratio to obtain the expected Doppler shifts of the subdwarf star, and I applied such shifts to the individual CCF. The final mean CCF is shown in Figure 2.3, and a central peak is detected near zero velocity in the secondary reference frame. I thus fitted a Gaussian to the central peak and estimated that it has velocity of  $V_r = 12 \pm 5 \text{ km s}^{-1}$  and dispersion of  $\sigma = 35 \pm 5 \text{ km s}^{-1}$ . The velocity offset is negligible, and the Gaussian dispersion velocity is consistent with that of a CCF for no rotational broadening. If this detection is reliable, the projected rotational broadening of the sdO companion will not exceed  $V \sin i < 30 \text{ km s}^{-1}$ .

I also constrained the temperature of the subdwarf and mass ratio of the system by creating grids of model spectra with different temperatures and by computing the shift-and-subtract mean CCF, fitting Gaussian functions to these CCFs and finding parameters that maximized the peak height of the central signal. I found that the subdwarf has a best-fit temperature of  $T_{\text{eff}} = 43 \pm 5 \text{ kK}$ . Likewise, I varied the mass ratio of the system, applied the associated Doppler shifts, and fitted the CCFs to fit for the peak signal in the final shift-and-subtract mean CCF. I estimate that the optimal mass ratio is  $q = 0.072 \pm 0.021$ .

I noticed that by grouping spectra into different phase ranges (e.g.,  $\phi = 0.0 - 0.75$  and  $\phi = 0.75 - 1.0$ ), the CCF displays a slightly different peak height (shown in Figure 2.3).

This suggests that the detected subdwarf flux feature is phase-dependent, i.e., the relative location of the subdwarf star in the binary orbit affects the observed flux.

Based on the computed temperature of the subdwarf, I also estimated the flux ratio of the system by forming a relation between assumed model  $f_2/f_1$  and the CCF peak height, and this indicates that  $f_2/f_1 > 0.0088 \pm 0.0011$ . I adopted temperatures of  $T_{\text{eff}} = 21$  and 43 kK for the Be star and the subdwarf, respectively. I used the UVBLUE model spectra (Rodríguez-Merino et al. 2005) with the adopted temperatures to estimate that the monochromatic surface flux ratio at 1170 Å is  $F_2/F_1 = 12.8$ . The observed flux ratio  $f_2/f_1$  related to the emitted surface flux ratio and radius ratio by

$$\frac{f_2}{f_1} = \frac{F_2}{F_1} \left( \frac{R_2}{R_1} \right)^2 \quad (2.1)$$

I thus estimated that the system has a radius ratio  $R_2/R_1 > 0.026 \pm 0.002$ . Assuming that the Be star has  $R_1 = 5 R_\odot$  based on its spectral type, this yields an estimate of the secondary radius of  $R_2 > 0.13 R_\odot$ .

## 2.4 Shell line features

A sharp absorption feature embedded in the line profile is known as a shell line feature, based upon the idealization of absorption by tangentially moving gas in a spherical distribution surrounding the star. Peters (1983) detected the shell features of HR 2142 through optical spectral analysis, and she defined the primary shell phase as the epoch prior to the Be star superior conjunction when the shell lines are red-shifted and the secondary shell phase as epoch after conjunction when the shell line features are blue-shifted. I have adopted the

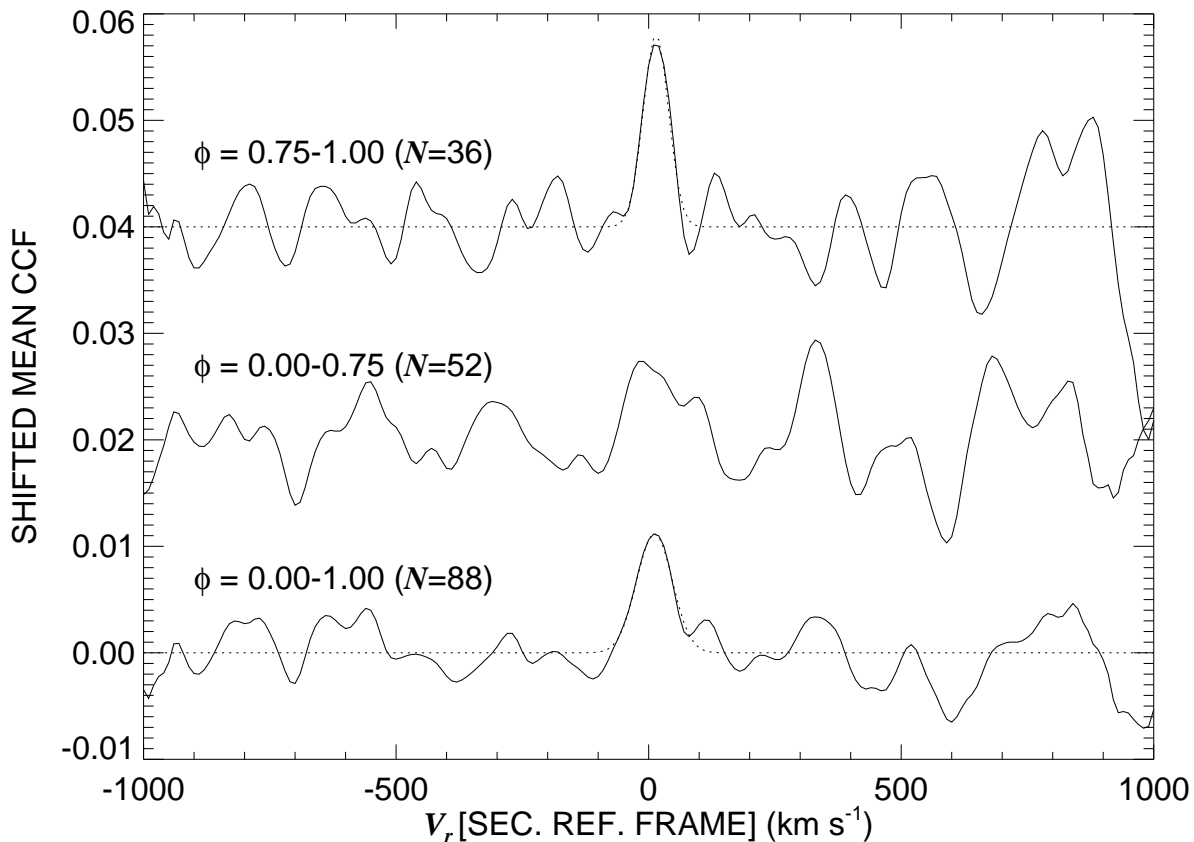


Figure 2.3: The shift-and-subtracted mean CCF computed from all 88 *IUE* spectra with a hot model spectrum over the range of 1150-1189 Å is plotted at bottom. I also grouped spectra into different phase ranges ( $\phi = 0.00-0.75$  and  $\phi = 0.75-1.00$ ) and plotted them above. The middle and top CCFs are offset by +0.02 and +0.04, respectively. A Gaussian fit was applied to the central peak signal and is shown as a dotted line.

phase definition from her work, which sets phase  $\phi = 0.0$  as the epoch when the Be star component is at superior conjunction relative to the observer.

The shell features are suggested to be associated with a gravitational perturbation of the disk gas caused by the subdwarf companion. I investigated the shell features using both the *IUE* FUV spectra and optical H $\alpha$  spectra. I first inspected the shell variations for 18 absorption features recorded in the *IUE* spectra. On the top panel of each plot, I plotted the individual

spectrum of each absorption feature as a function of radial velocity and an offset set by the orbital phase. In lower panel of each plot, I also plotted the spectra in a gray scale format to show shell line variations at different phases. Based on the strength and variability of these shell line features, I grouped them into four types. The first type displays the complete shell line features. Examples are the absorption features of Si II  $\lambda 1193$  and S III  $\lambda 1194$  that are shown in Figure 2.4, and also Figure A.1 of S III  $\lambda 1200$ , and Figure A.5 of Si III  $\lambda 1299$  in Appendix A. The shell line features of these absorption profiles appear at  $\phi = 0.5$ , and they gradually develop strength and reach absorption maximum near  $\phi = 0.95$ . Significant redshifts are seen in the gray scale image with a velocity range of 10 to 160 km s<sup>-1</sup> (primary shell phase). Right after  $\phi = 0.0$ , the shell line feature displays a short-lived, blue-shifted component that spans from  $-40$  to  $+20$  km s<sup>-1</sup> (secondary shell phase). Other components showing no velocity shifts are stationary line features likely formed in the interstellar medium or the Be star's circumstellar disk. The second type shows partial shell line features. These include the weak, low opacity lines of S II  $\lambda 1250$  in Figure A.2, Si II  $\lambda 1304$  in Figure A.6, and Si II  $\lambda 1526$  in Figure A.10. These absorption line profiles only display the primary shell line feature near  $\phi = 0.95$ . The third type mainly captures the stellar wind features of the Be star. Examples include lines of Si IV  $\lambda 1393$  in Figure A.8, Si IV  $\lambda 1402$  in Figure A.9, and C IV  $\lambda 1548, 1550$  doublet in Figure A.11. These wind line features extend up to blueshifts of  $-600$  km s<sup>-1</sup>. The signature of primary absorption shell line features appear near  $\phi = 0.6 - 1.0$ . The last type of shell line features display both significant blueshifts near  $\phi = 0.5$  (Be star is at inferior conjunction relative to the observer) and extreme redshifts

near  $\phi = 0.95$ . This group includes the lines of the C II  $\lambda 1334, 1335$  doublet in Figure A.7, Al III  $\lambda 1854$  in Figure A.13, Al III  $\lambda 1862$  in Figure A.14, and Fe III  $\lambda 1895$  in Figure A.15. I also investigated the optical shell features of the H $\alpha$  emission line from the KPNO observations. In Figure 2.4, a similar plot is shown for individual spectra offset by their orbital phase and plotted as a function of radial velocity. The shell feature is not very prominent due to the fact that the broad H $\alpha$  emission is dominated by the flux contribution from the Be circumstellar disk. Near  $\phi = 0.95$ , the shell absorption appears as a redshifted feature, which is in agreement with the findings from the *IUE* observations.

## 2.5 Disk models

Based on estimation of the secondary radius and the mass ratio of this binary system (see Section 2.3), I realized that the subdwarf is smaller than its Roche radius (Eggleton 1983). This indicates that the shell line features are not likely formed from a gas stream from a Roche-filling subdwarf as suggested by Peters (1983). Instead I adopted a circumstellar disk model to describe the possible formation of such shell features as consequences of the subdwarf's gravitational perturbation of the Be disk.

In Figure 2.6, I first illustrate the geometry of this model. The location of the Be star is indicated by a small white circle in middle of the figure with radius of  $5 R_{\odot}$ , right next to the center of mass of the system (shown as a plus sign). The subdwarf is located to the right of the Be star at  $\phi = 0.0$  (the subdwarf is at inferior conjunction relative to the observer). The major axis connecting both stellar components is shown as the horizontal solid line,

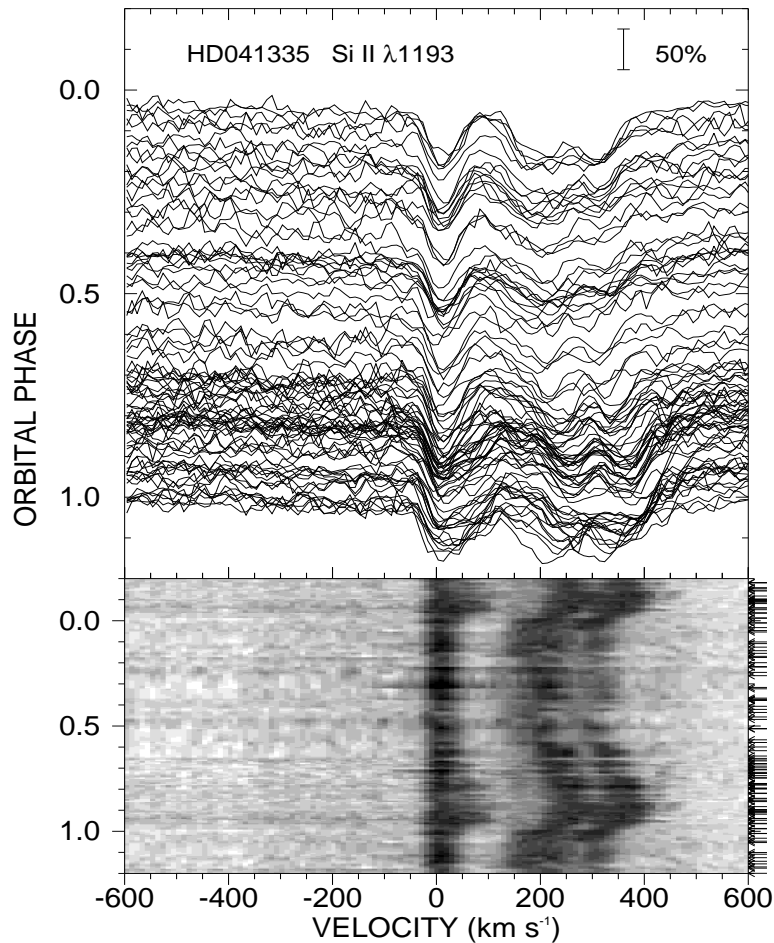


Figure 2.4: The top panel displays the individual spectra of Si II  $\lambda 1193.290$  as a function of the radial velocity, and each spectral flux is offset by its orbital phase. The depth of the absorption features relative to the continuum is shown by the scale in the upper right of the figure. The bottom panel shows the spectra in a gray scale format where black corresponds to the deepest absorption and white to the flux maximum. The lines of S III  $\lambda 1194$  appear shifted to the right.

and each tick mark on both axes has dimension of  $a/2$ . I have adopted the calculation of mass ratio of  $q = 0.072 \pm 0.021$  in Section 2.3 and assumed an inclination of  $i = 85^\circ$  to estimate the dimension of the semi-major axis of  $a = 176 R_\odot$ . Small arrows indicate the orbital motion of each component, and due to the relatively small motion of the Be star

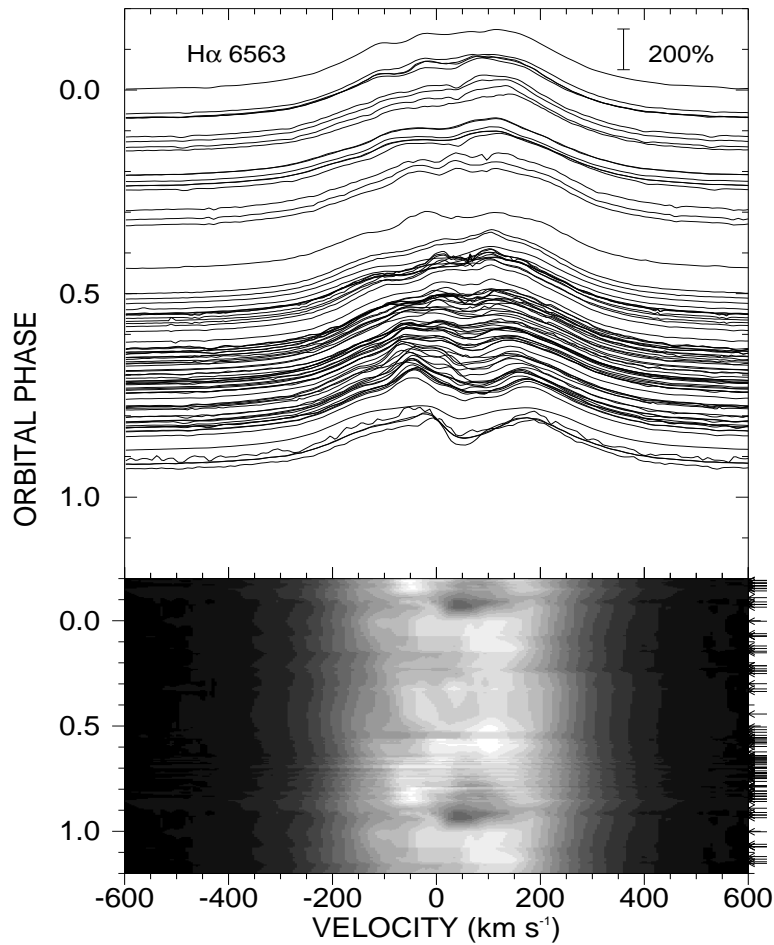


Figure 2.5: The top panel displays the individual spectra of H $\alpha$  as a function of the radial velocity, and each spectrum is offset by its orbital phase. The scale of the emission feature relative to the continuum is shown by the bar in the upper right of the figure. The bottom panel shows the spectra in a gray scale format.

compared to the subdwarf companion, only an arrow head is shown below the white circle for the Be component. The darkest gray region around the white circle is the circumstellar disk closest to the central Be star. Using the method from Grundstrom & Gies (2006), the disk has a radius of  $9.5 R_*$  based on the H $\alpha$  equivalent width ( $W_\lambda = -31 \text{ \AA}$ ). The medium gray shaded region indicates the extended disk beyond this radius with lower density. Both

components have a size smaller than their Roche-lobes, which are shown in dashed lines. The protoplanetary disk model from Bate et al. (2003) suggests that a planet is likely to create a gap in the circumstellar disk of the star. I adopted this model and assumed that the subdwarf acts in the same way as planet to create a gap in the Be disk. For simplicity, I assumed that the gap has the size of Roche-lobe of the subdwarf star along the axis towards the Be star, which is shown in white in the figure. Beyond the gap, the disk attains even lower density as shown in light gray region in the outer part of the figure.

Ogilvie & Lubow (2002) and Bate et al. (2003) argued that the companion may create tidal wakes within the disk due to its gravitational attraction. Based on a two-dimensional technique as described in Ogilvie & Lubow (2002), I estimated the location of the one-armed spiral wake, and this is shown as a solid line that spirals into the Be disk. The dotted lines above and below the subdwarf companion indicate the path of gas flowing either towards or away from the Be star due to the gravitational pull of the subdwarf. This kind of motion is also known as “horseshoe orbit” as introduced by Dermott & Murray (1981). The dotted lines show only part of such an orbit near the subdwarf. As a result of the gravitational attraction of the subdwarf, gas at the outer edge of the gap will be pulled inwards towards the Be star. The gas ahead of the subdwarf will create a tidal wake at the inner edge of the gap (or outer edge of the gray Be disk), and then such gas will follow the trajectory of the horseshoe orbit all the way around the gray Be disk. Due to the conservation of angular momentum, the gas overtaking the subdwarf at inner edge of the gap (or outer edge of the gray Be disk) will be pulled outwards towards the subdwarf with a decreasing azimuthal

speed. This outwards moving gas will enter the outer light-gray region beyond the gap that forms a circumbinary disk.

Due to the gas motion along the horseshoe orbit, near  $\phi = 0.95$  (or  $\phi = 0.0$ ) the tidal wake creates density enhancements in the subdwarf's vicinity. Such enhancements are likely responsible for the shell line features appearing in many of the spectra (in Section 2.4). The primary shell line features start near  $\phi = 0.5$ , when the inward moving gas is gradually projected against the Be star, and these gas stream reach the maximum velocity near  $\phi = 0.95$  (line of sight shown as the dashed dotted line). Thus the inward moving gas ahead of the subdwarf will encounter the Be star disk, create a local density enhancement, and our view through this region to the Be star will form the prominent redshifts showing in the spectra. It is possible that some portion of gas crossing the gap will form an accretion disk around the subdwarf as suggested by Bate et al. (2003). Likewise, near  $\phi = 0.0$  out-flowing gas at outer edge of Be disk is pulled outwards by the subdwarf and creates blueshifts in the spectra. This gas flow will extend outwards to the lower density region of the Be disk (light gray region). The higher density at outer edge of the inner disk (gray region) compared to the lower density at the inner edge of the outer disk (light gray region) may be responsible for the asymmetry appearing in the strengths of the primary and secondary shell phases. A few shell line features displaying blueshifts near  $\phi = 0.5$  were mentioned in Section 2.4, and it is likely that such blueshifts are formed near the L3 point shown in Figure 2.6, where gas moves outwards and towards the observer. However, the two-dimensional circumstellar disk model is only an approximation scheme to describe the shell line variations seen in the

spectra. The actual gap size depends on the disk viscosity, and three-dimensional smoothed particle hydrodynamics simulations conducted by Okazaki et al. (2002) and Panoglou et al. (2016) suggest that the gap size may not be as big as shown in Figure 2.6. More in-depth simulations will be needed to constrain the geometry and dimensions of the circumstellar disk in the HR 2142 binary system.

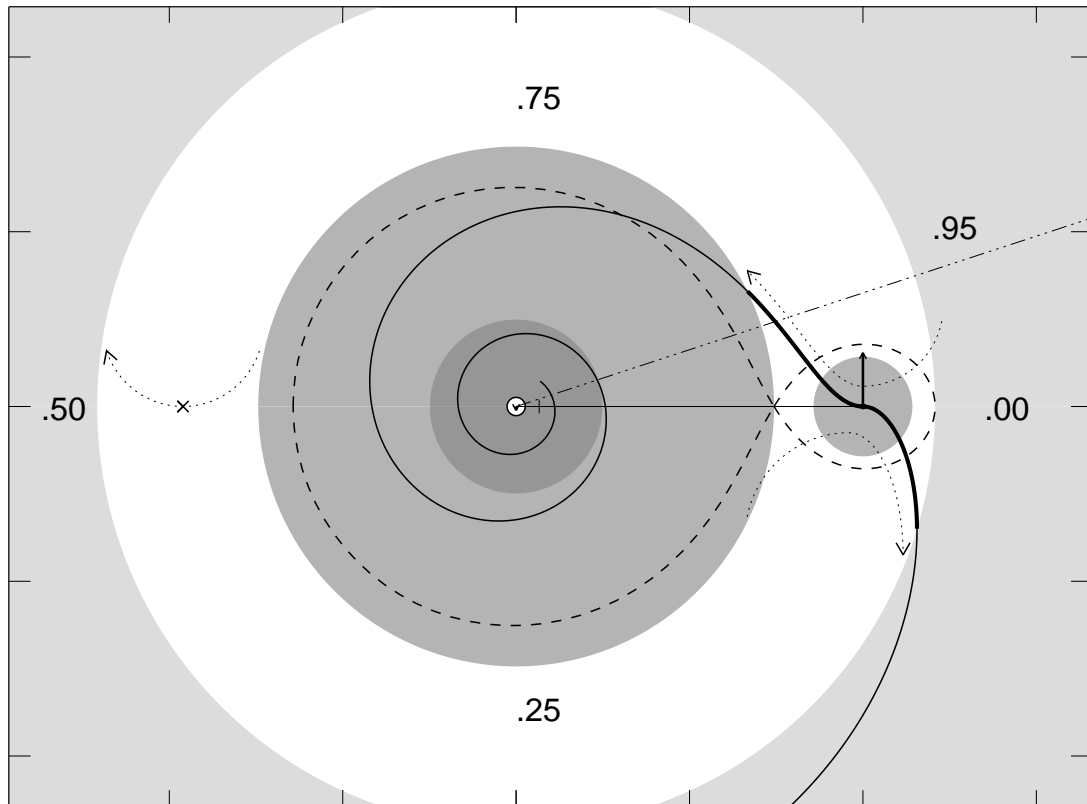


Figure 2.6: This figure illustrates the circumstellar disk model of HR 2142. The Be star is indicated as the white circle in the center of the figure, the semi-major axis of the binary system is shown as the horizontal solid line connecting both stellar components, and each outer tick mark has a dimension of  $a/2$ . Based on method described in Grundstrom & Gies (2006) we estimated the Be disk size and plotted it in darkest gray. The lower density part of the disk extends beyond this radius and is shown in medium gray. Both components are smaller than their Roche-lobes, which are indicated by a dashed line. We adopted the tidal wake model of Ogilvie & Lubow (2002) and Bate et al. (2003) to plot the gap in the Be disk due to subdwarf’s gravitational force (shown in white) and to estimate the location of the one-armed spiral tidal wake (shown as the solid line spiraling into the Be disk). Gas density enhancements due to the subdwarf’s gravity are indicated by the thicker segment, and gas crossing the gap is shown by dotted lines with arrows to show their motion within the disk. At  $\phi = 0.95$ , the gas stream moving towards the Be star (away from us) is redshifted (primary shell phase); right after  $\phi = 0.0$ , the gas flow outwards from the Be disk (towards us) displays blueshifts (secondary shell phase). At  $\phi = 0.5$ , the gas stream moving away from the disk towards the L3 Lagrangian point is shown as a dotted line with an arrow.

## CHAPTER 3

### DETECTION OF THE HOT SUBDWARF COMPANION OF 60 CYRGN1 FROM A SURVEY OF IUE SPECTRA OF BE BINARY STARS

#### 3.1 A survey of *IUE* spectra of 6 Be stars

Based on the positive detection of the subwarf companion in the HR 2142 binary system, I have now increased the number of detected Be+subdwarf binaries to four. Here I extend the search for subdwarfs to another six Be binary systems that were observed many times over the lifetime of *IUE*. All of these targets are known single-lined spectroscopic binaries with hitherto undetected, low mass companions. The targets are listed in Table 3.1 with spectral classifications from Slettebak (1982) and projected rotational velocities from Frémat et al. (2005). I briefly summarize below the key studies on their orbital and physical properties.

**$\gamma$  Cas (HD 5394).** This is the first known Be star from spectroscopy by Secchi (1866). The binarity of the system was confirmed by Nemravová et al. (2012) through a 16.84 year span of optical spectra monitoring. Extensive studies of the star’s X-ray emission and circumstellar environment (Smith et al. 2012; Stee et al. 2012; Hamaguchi et al. 2016) suggest that the X-ray emission is associated with parts of the disk gas of the Be star, so that the companion need not be an accreting neutron star or white dwarf. Several other X-ray emitting Be stars like  $\gamma$  Cas appear to be “blue stragglers” that may have been formed through binary mass transfer (Smith et al. 2016).

**28 Tau (HD 23862).** Pleione is a known shell star with cyclic variability lasting decades. The shell activity that occurred over the duration of the *IUE* observations is discussed in

Appendix B. Nemravová et al. (2010) confirmed Pleione as the primary component of a binary system through Doppler shifts from  $H\alpha$  emission spectroscopy.

$\zeta$  **Tau** (**HD 37202**). Hynek & Struve (1942) confirmed the binarity of the system using radial velocities from Balmer lines measured in photographic plates, and Delplace (1971) estimated the system dimensions by considering the size of the Be disk. Ruždjak et al. (2009) improved the orbital ephemeris of the system from  $H\alpha$  spectroscopy and  $UBV$  photometry observations over about a century.

$\kappa$  **Dra** (**HD 109387**). Saad et al. (2005) determined the orbit of the binary through wide-ranging spectroscopic observations. They found no direct evidence of the companion's spectrum.

**60 Cyg** (**HD 200310**). Plaskett & Pearce (1931) reported that the star belongs to a spectroscopic binary system. Koubský et al. (2000) discussed the long, medium, and short term variability in the observed spectra and light curves, and they presented orbital elements from radial velocity measurements of the Be star.

$\pi$  **Aqr** (**HD 212571**). Bjorkman et al. (2002) discovered the binary nature through a radial velocity analysis of the absorption and emission lines. They suggested that the companion could be an A- or F-type main-sequence star, but the absorption spectrum of the companion was not observed. Zharikov et al. (2013) made an analysis of the orbital variations of the  $H\alpha$  emission line. They estimated that the secondary has a mass  $< 2 M_{\odot}$ .

Table 3.1: *IUE* Observations of Be Binary Systems

Star Name	HD Number	HIP Number	Spectral Classification	$V \sin i$ (km s <sup>-1</sup> )	Number of Observations	Time span (years)
$\gamma$ Cas	5394	4427	B0.5 IVe	432	228	18
28 Tau	23862	17851	B8 Ve shell	286	48	17
$\zeta$ Tau	37202	26451	B1 IVe shell	310	34	17
$\kappa$ Dra	109387	61281	B5 IIIe	200	26	11
60 Cyg	200310	103732	B1 Ve	300	23	15
$\pi$ Aqr	212571	110672	B1 III-IVe	230	22	17

Note. –Spectral classifications and projected rotational velocities are from Slettebak (1982) and Frémat et al. (2005), respectively.

### 3.2 Search for the UV flux of hot companions

The search technique is centered on forming a cross-correlation function (CCF) of the observed spectra with model spectra for the expected effective temperature  $T_{\text{eff}}$  of a hot companion. Two issues make this process difficult. First, any companion is probably relatively faint compared to its Be host star, so given the low S/N of the *IUE* spectra ( $\approx 20$  per resolution element; Nichols & Linsky 1996), it will be hard to identify the signal of the companion in the CCF for any one spectrum. Second, some of the lines in the model spectrum of the hot companion may also be present (although weaker) in the spectrum of the Be star, so the derived CCF may present a composite of companion and Be signals. The solution here is to

apply a Doppler tomography algorithm (Bagnuolo et al. 1994) to the derived CCFs in order to separate both the companion and Be star CCF components and to use all the spectra together to increase the net S/N of the reconstructed CCFs. Below I outline how the spectra are organized, how the trial velocity curves were estimated for the components, and details of the CCF reconstruction process. The final results for the reconstructed secondary CCFs are discussed at the end of the section and are shown in Figure 3.1.

I downloaded the high dispersion, short wavelength prime (SWP) spectra of the selected targets from MAST<sup>1</sup>. The number of available spectra and their time span are listed in Table 3.1. The spectra have a resolving power of  $\lambda/\Delta\lambda = 13,000$ , and the wavelength coverage is from 1150 Å to 1950 Å. The individual echelle orders were merged and placed on a heliocentric grid using the standard *IUE* IDL data reduction pipeline *iuerdaf*. The spectra were then transformed onto a uniform heliocentric wavelength grid in  $\log \lambda$  steps equivalent to 10 km s<sup>-1</sup>, and for the more distant stars (HD 5394, HD 200310, and HD 212571 with  $d > 180$  pc), the wavelength calibration was checked through alignment (and then removal) of interstellar lines. The spectra were rectified with respect to the relatively line-free parts of the spectra into a final matrix of stellar flux as a function of wavelength and time of observation.

---

<sup>1</sup><https://archive.stsci.edu/iue/>

Table 3.2: Adopted Orbital Elements

HD Number	$P$ (days)	$T^a$ (HJD-2,400,000)	$e$	$\omega$ (deg)	$K_1$ (km s <sup>-1</sup> )	$\gamma$ (km s <sup>-1</sup> )	Trial $M_2/M_1$	$f_2/f_1$	Source Reference
5394	$203.523 \pm 0.076$	$52183.65 \pm 0.62$	0.0	...	$4.30 \pm 0.09$	$0.02 \pm 0.06$	0.072	$< 0.006$	Nemravová et al. (2012)
23862	$218.023 \pm 0.023$	$40040.4 \pm 1.6$	$0.596 \pm 0.035$	$147.7 \pm 4.5$	$5.41 \pm 0.35$	$-0.15 \pm 0.1$	0.082	$< 0.026$	Nemravová et al. (2010)
37202	$132.987 \pm 0.050$	$47025.6 \pm 1.8$	0.0	...	$7.43 \pm 0.46$	$20.0 \pm 0.4$	0.084	$< 0.013$	Ruždjak et al. (2009)
109387	$61.555 \pm 0.029$	$49980.22 \pm 0.59$	0.0	...	$6.81 \pm 0.24$	...	0.114	$< 0.010$	Saad et al. (2005)
200310	$146.6 \pm 0.6$	$50016.9 \pm 1.9$	0.0	...	$10.8 \pm 0.1$	-13.4	0.131	0.034	Koubský et al. (2000)
212571	$84.135 \pm 0.004$	$50316.91 \pm 0.04$	0.0	...	$16.7 \pm 0.2$	$-4.9 \pm 0.1$	0.163	$< 0.010$	Bjorkman et al. (2002)

- a For systems with circular orbits, the epoch corresponds to the time of Be star maximum radial velocity, and for the eccentric orbit of HD 23682, the epoch corresponds to the time of periastron.

The next aspect of the process was to estimate the radial velocities of both components at the time of observation. I initially measured radial velocities of the Be components using the CCF methods adopted in past work (Peters et al. 2016), but the scatter in the results (and poor phase coverage in some cases) was too large to offer any improvement over the existing orbital solutions. Consequently I adopted the published orbital elements for the Be star primaries that are summarized in Table 3.2. Then I calculated velocities for the primary Be star at the times of observation using these solutions. The secondary star velocities were derived from the primary velocities using the systemic velocity  $\gamma$  and an assumed mass ratio  $q = M_2/M_1$ . This mass ratio was calculated from the spectroscopic mass function and published estimates of the Be star mass and system inclination. The latter two parameters were taken from Silaj et al. (2014) and the references cited in Table 3.2. The derived values of  $q$  are given in column 8 of Table 3.2. One of the targets HD 23862 (28 Tau or Pleione) shows long term variation in brightness and color during its B, Be, and Be-shell phase transitions. I thus documented the shell activity variation as recorded in the *IUE* spectra, and measurements of its shell line velocities are given in Appendix B.

Each spectrum was cross-correlated with a model spectrum that was derived from the grid of synthetic spectra for hot stars using the non-local thermal equilibrium (non-LTE) atmosphere program TLUSTY and the associated radiative transfer code SYNSPEC from Lanz & Hubeny (2003). The default model temperature was set to  $T_{\text{eff}} = 45$  kK, a value similar to that found for other hot subdwarf systems (Peters et al. 2016), and the gravity was assigned a value of  $\log g = 4.75$ , the highest gravity available in the grid but probably lower

than expected. The model spectrum is based upon a solar abundance and a microturbulent velocity of  $10 \text{ km s}^{-1}$ . The synthetic spectrum was rectified to a unit continuum, rebinned onto the observed  $\log \lambda$  grid, and smoothed to the instrumental broadening of  $\text{FWHM} = 25 \text{ km s}^{-1}$ . No rotational broadening was applied given the sharp appearance of the subdwarf spectra in other Be binary systems. I excluded the beginning and ending regions, plus very broad wind lines from the spectra before calculating the CCF to avoid introduction of troublesome wide structures in the CCF. The regions adjoining the excluded zones were gradually smoothed to a pure continuum using a Tukey filter function, which applies a cosine function to reduce line depths close to the boundaries. The final result is an array of CCF functions corresponding to each observed spectrum.

The derived CCF functions usually display a wide and shallow peak because of some correlation between the broad lines of the Be star spectrum and the model spectrum. I suppose that each CCF is the sum of a broad component from the Be star and a possible narrow component from the subdwarf star, each Doppler-shifted accord to the orbital velocity at the time of observation. Then I performed a reconstruction of these two components using the Doppler tomography algorithm of Bagnuolo et al. (1994). This procedure assumes radial velocity shifts from the adopted orbital elements (Table 3.2), and then uses an iterative scheme to reconstruct the two components that when shifted and co-added make the best fit of the observed CCFs. In this instance, I assumed that both components contribute equally to the combined CCF, and consequently I divided the results by a factor of two so that the CCF amplitude matches that in the observed CCFs. The iterative scheme begins by assuming

that the primary CCF is equal to the simple mean of all the CCFs and that the secondary CCF is flat and featureless (no secondary signal is present).

The reconstructed primary component appears almost flat in the cases of the cooler Be star primaries (28 Tau and  $\kappa$  Dra) because there is very little correlation between the features in their and the model spectra. However, the primary CCFs for the hotter Be stars ( $\gamma$  Cas,  $\zeta$  Tau, 60 Cyg,  $\pi$  Aqr) are broad as expected for the broad and shallow absorption lines in their spectra that are common to those in the hot model spectrum. The trial reconstructed CCFs for the secondaries are generally shallow with some low frequency curvature due to the characteristics of the spectral rectification and line clusters. In order to remove the variations in the background, I first smoothed the secondary CCF by convolution with a Gaussian of  $\text{FWHM} = 350 \text{ km s}^{-1}$ , and then I subtracted this smoothed background variation from the secondary CCF to search for any narrow peak associated with a hot subdwarf spectral component. The resulting secondary CCFs are plotted in Figure 3.1, and they generally appear featureless, with the striking exception of 60 Cyg, in which there is a prominent peak near the expected zero velocity in the frame of reference of the secondary star. Thus, my search method has led to the discovery of one new detection of a hot companion to the Be star 60 Cyg. In the next section, I discuss the properties of the companion of 60 Cyg and consider the flux limits of the companions of the other five targets.

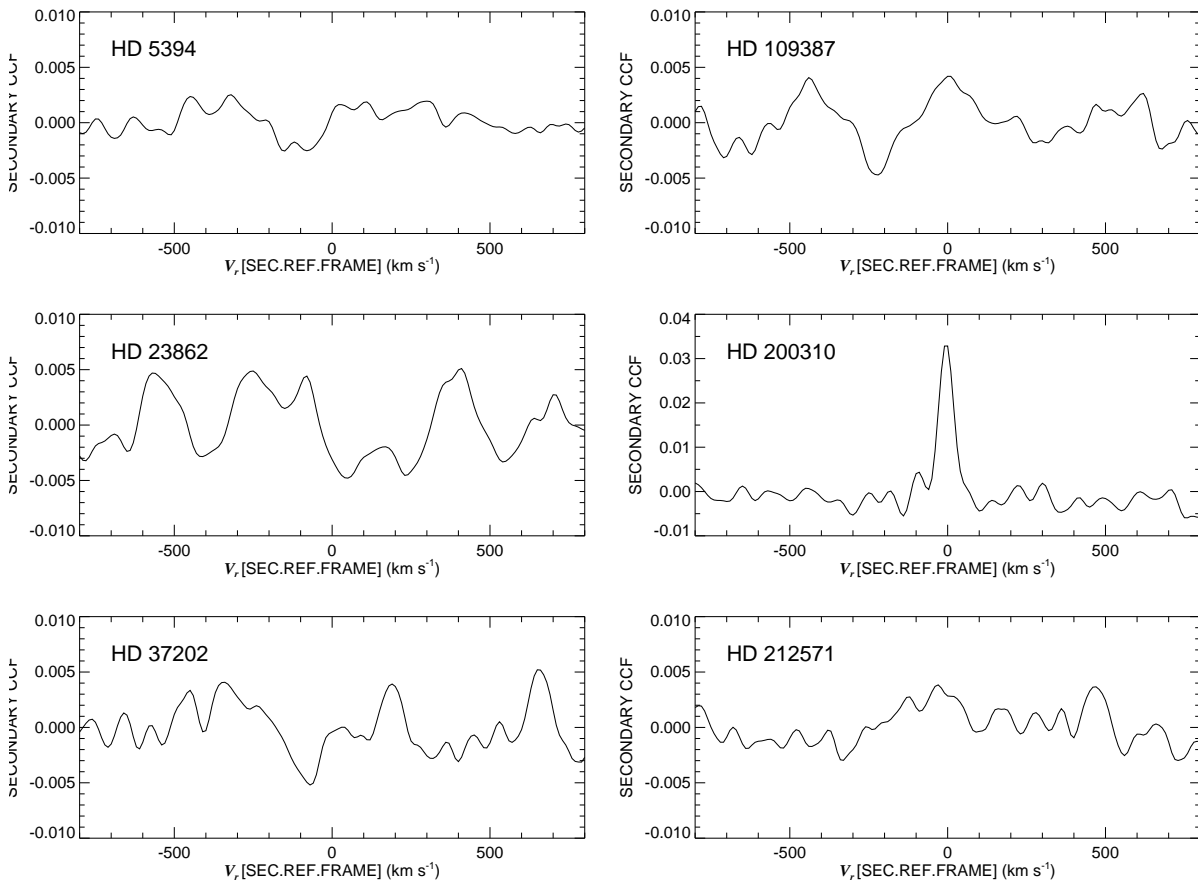


Figure 3.1: The reconstructed secondary CCFs of the six Be binary systems derived from the assumed Doppler shifts of the secondary and a model hot reference spectrum ( $T_{\text{eff}} = 45 \text{ kK}$ ). A detected peak is only seen in the case of  $60 \text{ Cyg} = \text{HD 200310}$ .

### 3.3 Implications of the detection of the companion of 60 Cyg

The detection of the spectral signature of the hot companion of 60 Cyg involved making assumptions about the mass ratio and companion effective temperature. I next explore how changing these parameters can help us find better estimates of their values. I began by repeating the analysis for a grid of assumed mass ratios, and in each case I fit a Gaussian to the peak in the reconstructed secondary CCF. The CCF peak attains a maximum at  $q =$

$M_2/M_1 = 0.146 \pm 0.023$ , where the uncertainty represents the half-range of mass ratios where the peak height is within the  $1 \sigma$  zone of the maximum CCF peak height of  $0.0335 \pm 0.0015$ . I note that this estimate of the mass ratio is the same within uncertainties as the trial mass ratio I derived from the primary mass function, mass, and system inclination (Table 3.2). I fixed the mass ratio to this result, and then repeated the analysis using TLUSTY/SYNSPEC model spectra for the cross-correlation template that ranged from  $T_{\text{eff}} = 27.5$  to 55 kK. I made a spline fit of peak height as a function of assumed temperature to arrive at an estimate of  $T_{\text{eff}} = (42 \pm 4)$  kK for the companion.

I am also interested in determining the UV flux ratio that would produce a secondary CCF with the observed peak height. I determined this quantity by first creating a subdwarf model spectrum for  $T_{\text{eff}} = 42$  kK,  $\log g = 4.75$ ,  $V \sin i = 0$ , and constructing a Be star model for  $T_{\text{eff}} = 27$  kK,  $\log g = 4.0$ ,  $V \sin i = 320 \text{ km s}^{-1}$  (Koubský et al. 2000). Then I created a model set of observations over an assumed grid of flux ratios in the following way. For each time of observation, the model spectra were shifted by the assigned orbital Doppler velocities. Next the model secondary spectrum was rescaled in flux to match that of the model primary spectrum in the range  $1500 - 1550 \text{ \AA}$ . Then the model secondary spectrum was rescaled again in flux according to the assumed monochromatic flux ratio  $f_2/f_1$ . The sum of the model primary and rescaled secondary spectra was then rectified to a unit continuum. I then repeated the CCF and tomography analysis of this model set of spectra in the same way as done with the observed spectra to derive a relationship between reconstructed secondary CCF peak height and the assumed flux ratio  $f_2/f_1$  at 1525

Å. Interpolating the observed CCF peak height in this relation led to a monochromatic flux ratio estimate of  $f_2/f_1 = 0.0339 \pm 0.0015$  at 1525 Å. This flux ratio is related to the ratio of stellar radii by

$$\frac{f_2}{f_1} = \frac{F_2}{F_1} \left( \frac{R_2}{R_1} \right)^2 \quad (3.1)$$

where  $F_2/F_1$  is the monochromatic surface flux ratio of the stars and is equal to  $F_2/F_1 = 3.88$  in the continuum at 1525 Å for the adopted temperatures of the two stars in the TLUSTY models. Using the above relation, the resulting radius ratio is  $R_2/R_1 = 0.093 \pm 0.012$ , where the uncertainty includes the range of  $F_2/F_1$  associated with the error in  $T_{\text{eff}}$ .

Koubský et al. (2000) estimate that the Be star mass and mean radius of 60 Cyg are  $M_1 = 11.8 M_\odot$  and  $R_1 = 5.1 R_\odot$ , respectively. If we adopt these values, then the mass, radius, and gravity of the subdwarf are  $M_2 = 1.7 M_\odot$ ,  $R_2 = 0.48 R_\odot$ , and  $\log g_2 = 5.3$ , respectively. This estimate of the companion mass places it above the Chandrasekhar limit of  $1.4M_\odot$ , so it is possible that the subdwarf may become a neutron star in the future. If so, then 60 Cyg may be a progenitor of a Be X-ray binary system. The estimated gravity of the subdwarf is higher than the limit in the TLUSTY grid  $\log g = 4.75$  that I used in deriving the best fit  $T_{\text{eff}}$ . The relative strengths of the spectral features in the model spectra depend on the ionization balance in the model, so if I had used a higher  $\log g$  model, I would probably arrive at a slightly higher estimate of  $T_{\text{eff}}$  and a somewhat lower value of  $R_2$ .

It is remarkable that among the now five known Be+subdwarf systems that 60 Cyg and 59 Cyg are separated by about one degree on the sky. The stars are not known as cluster members, but they may be affiliated with other early-type stars in their vicinity. I formed

a list of stars with B spectral classifications within  $2^\circ$  of the midpoint between 59 Cyg and 60 Cyg from the catalog of Skiff (2014), and then collected proper motions from the Gaia Collaboration (2016) and parallaxes from van Leeuwen (2007) for these stars. Table 3.3 shows those selected with proper motions and parallaxes within  $2\sigma$  of those of 59 Cyg (HD 200120) and 60 Cyg (HD 200310). This collection of six objects may form part of a hitherto unknown co-moving group of equal age stars. If so, then 59 Cyg and 60 Cyg may be at a similar stage of binary evolution because of their common origin and age.

Table 3.3: Co-moving Stars in the Vicinity of 59 Cyg and 60 Cyg

HD Number	$V$ (mag)	Spectral Classification	$\mu_\alpha$ (mas y <sup>-1</sup> )	$\mu_\delta$ (mas y <sup>-1</sup> )	$\pi$ (mas)	$V_r$ (km s <sup>-1</sup> )
198625	6.33	B4 Ve	$4.2 \pm 1.0$	$3.8 \pm 1.0$	$2.03 \pm 0.34$	-15
199309	8.65	B8 V	$6.4 \pm 0.6$	$2.6 \pm 0.6$	$3.08 \pm 0.70$	-25
199889	8.33	B8 V	$6.4 \pm 0.6$	$3.1 \pm 0.6$	$3.10 \pm 0.52$	-22
200120	4.75	B1.5 Vne	$7.3 \pm 1.0$	$2.5 \pm 1.0$	$2.30 \pm 0.42$	-10
200310	5.43	B1.5 IV-Vne	$6.1 \pm 1.0$	$3.4 \pm 1.0$	$2.14 \pm 0.37$	-13
200615	8.13	B8 V	$6.0 \pm 0.7$	$1.4 \pm 0.6$	$1.69 \pm 0.53$	-17

Note. –The spectral classifications are from the collection by Skiff (2014), proper motions  $\mu_\alpha$  and  $\mu_\delta$  are from the Gaia Collaboration (2016), and parallaxes are from van Leeuwen (2007). The  $V$  magnitude and radial velocity data are from SIMBAD, with the exception of the systemic velocities for 59 Cyg (Peters et al. 2013) and 60 Cyg (Koubský et al. 2000).

I found no evidence of the companion flux in the other five Be binaries. I placed a

constraint on the relative flux of the undetected companion in the same way as I found the flux ratio for 60 Cyg by creating model observation sets for the adopted stellar parameters and then finding the relation between  $f_2/f_1$  at 1525 Å and the secondary CCF peak height. I used these relations and the observed standard deviations in the derived CCFs (Fig. 3.1) to estimate a conservative upper limit on  $f_2/f_1$  that would yield a  $5\sigma$  peak in the CCF. These limits on the monochromatic flux are listed in column 9 of Table 3.2, and in general they indicate that the companions contribute no more than 1% of the flux at 1525 Å. I caution that these limits tacitly assume that the companions are hot and narrow-lined, which may not be correct in all cases. Nevertheless, the results suggest that if the companions are hot, then they must have small radii and relatively low luminosity. For example, the flux ratio limit is the smallest in the case of  $\gamma$  Cas,  $f_2/f_1 < 0.006$ , and this limit implies  $R_2/R_\odot < 0.3$  and  $\log L_2/L_\odot < 2.6$ . The faintness of such companions is probably consistent with evolutionary models that predict that such post-mass transfer remnants spend most of their remaining He-burning lifetime as faint, core He-burning objects (Schootemeijer et al. 2018).

## CHAPTER 4

### DETECTION OF ADDITIONAL BE+SDO SYSTEMS FROM *IUE* SPECTROSCOPY

#### 4.1 Search for additional subdwarf companion of Be stars from *IUE*

The detection of the subdwarf companions of the confirmed systems benefited from the large number of observations available in the *IUE* archive in order to take advantage of the  $\sqrt{n}$  improvement in S/N by combining all the observations in the analysis. However, relatively bright subdwarf companions should be detected even in a single *IUE* observation through calculations of CCFs with a model spectrum for a hot star. The goal of this work is to detect other Be+sdO systems by searching for such relatively bright companions through analysis of individual spectra for a large sample of Be stars.

#### 4.2 Search for sdO companions

##### *4.2.1 Target selection from CCFs*

The main sample of Be stars was adopted from the list of Yudin (2001), who presented an analysis of intrinsic polarization, projected rotational velocity, and IR excess of 627 Be stars. I combed through the *IUE* archive to find these targets, and I collected 3092 SWP/H spectra of 226 stars from the archive. I further expanded the sample by adding 111 SWP/H spectra of 38 rapidly rotating, non-emission stars with projected rotational velocity  $V \sin i > 300$  km s<sup>-1</sup>. These stars may also be the product of spin up by mass transfer in a binary.

I downloaded the SWP/H spectra of these 264 stars from MAST<sup>1</sup>. The spectra were reduced

---

<sup>1</sup><https://archive.stsci.edu/iue/>

and rectified following the procedures reported in Wang et al. (2017), except that I left any interstellar medium lines in place. The estimated temperatures of the five known sdO companions all have  $T_{\text{eff}} > 40$  kK. Thus, I adopted a synthetic spectrum with  $T_{\text{eff}} = 45$  kK from the grid of Lanz & Hubeny (2003) that I used earlier (Wang et al. 2017), and I cross-correlated it with all the observed spectra. I excluded the beginning and ending regions and very broad or blended line regions (including the Si III  $\lambda 1300$  complex, Si IV  $\lambda\lambda 1394, 1403$ , Si II  $\lambda\lambda 1527, 1533$ , and C IV  $\lambda 1550$ ) that were replaced by a linear interpolation across the adjacent continuum to avoid introduction of broad features into the CCFs.

I began the search for hot companions by forming the ratio of the CCF maximum height (peak signal S) within a velocity range of  $\pm 200$  km s<sup>-1</sup> (larger than the typical span of Doppler shift of the known binaries) to the standard deviation of the CCF in higher velocity portions (background noise N), and I then calculated the average peak-to-background ratio (S/N) from the individual ratios for all the available spectra for each star. The average S/N ratios of the known Be+sdO systems ( $\phi$  Per, FY CMa, 59 Cyg, and 60 Cyg) all have S/N > 3.0. Thus, I set this CCF peak-to-background ratio as the lower limit to select candidate sdO binaries. Null detections of companion stars with CCF S/N ratios below the selection criterion are listed in Table 4.1. If the stars in Table 4.1 host hot companions, then their sdO components must be too faint to detect in individual *IUE* spectra. Table 4.1 includes HR 2142 (=HD 41335), which only displays the weak signal of the companion in a subset of spectra (Peters et al. 2016). On the other hand, a strong signal appeared and met the selection criterion for 66 stars, forming a preliminary list of potential binary

systems with relatively bright subdwarf companions. I collected the spectral classifications and projected rotational velocities of these targets from the literature. The HD number, star name, HIP number, spectral classification, projected rotational velocity, number of SWP/H spectra available in the *IUE* archive, average CCF S/N ratio, and references for the spectral types and  $V \sin i$  are tabulated in Table 4.2.

Table 4.1: Stars with CCF S/N < 3

Name	Name	Name	Name	Name
144	4180	6811	10144	11415
11946	13268	14434	15642	18552
20340	21362	21551	22192	22780
23016	23302	23383	23478	23480
23552	23630	23862	24479	25940
26356	26670	26793	28459	28867
29866	32343	32990	32991	33599
34863	34959	35407	35439	36012
36408	36665	36939	37115	37202
37397	37795	37967	38087	38831
41335*	42054	42545	44458	44506
45314	45542	45725	45910	45995
46056	46485	47054	47359	50123
50820	51480	52356	52721	56139
57150	58343	58715	60606	61355
63462	65875	69106	69404	70084
71216	72014	72067	75311	75416

Continued on next page

Table 4.1 – Continued from previous page

Name	Name	Name	Name	Name
76534	77366	79351	83953	86612
87543	87901	89080	89884	89890
91120	91465	92938	93563	100673
100889	102776	105382	107348	109387
109857	110335	110432	110863	112078
112091	118246	119921	121847	124367
127973	130109	134481	135734	137432
138749	138769	139431	141637	142184
142926	142983	149485	149671	149757
155896	156468	158427	158643	160202
162732	164284	164906	165063	166014
167128	168957	169033	171406	174639
175869	177724	178475	179343	181615
182180	183133	183362	183656	183914
185037	187235	187811	189687	191423
192044	192685	192954	193182	193911
195325	198183	198625	199218	202904
203064	203467	203699	204860	205637
206773	208057	208392	208682	208886
209014	209409	209522	210129	214748
216200	217050	217086	217543	217676
217891	218393	218674	219688	224686
BD+41 3731	BD+60 594	BD+34 1058		

\*HR 2142 has a faint sdO companion (Peters et al. 2016).

Note. –Stars are listed by HD number, except for the last three that are from the Bonner Durchmusterung Catalogue.

### 4.2.2 Detection criteria for Be+sdO systems

I adopted detection criteria for Be+sdO binaries that are based upon the characteristics of the five known systems. The best known system (and the one with the highest CCF S/N ratio in our sample) is  $\phi$  Per (HD 10516), and I show in Figure 4.1, top left panel, two CCFs for  $\phi$  Per at different orbital velocity extrema. The CCF peaks are narrow (indicative of a small projected rotational velocity) and show large velocity excursions due to the large semi-amplitude associated with the low mass sdO star (Gies et al. 1998). All five known Be+sdO binaries share these properties, so I adopted two detection criteria based upon them.

The first criterion is that any CCF signal from the sdO component must be narrow with a half width at half maximum (HWHM) much smaller than the projected rotational broadening  $V \sin i$  associated with the primary Be star target. Most Be stars are rapid rotators with large  $V \sin i$ , so their associated CCFs are very broad (see the case of  $\gamma$  Cas = HD 5394 in the lower left panel of Fig. 1), although a few pole-on Be stars do show smaller projected rotational broadening (see the CCFs of HD 120991 in the lower, right panel of Fig. 4.1). Note that this assumption biases the results against detection of rapidly rotating sdO components, but I doubt such exist in general because their progenitors probably became synchronous rotators in long period orbits during the earlier mass transfer phase. Note that the CCF signal from correlation with the Be star spectral features will become larger for hotter Be stars, so that the CCF will be more dominated by the Be star signal in earlier-type targets. I show, for example, the cases of CCFs for a hot (HD 155806) and a mid-temperature (HD 174237) emission-line star in the middle left and right panels, respectively, of Figure 4.1.

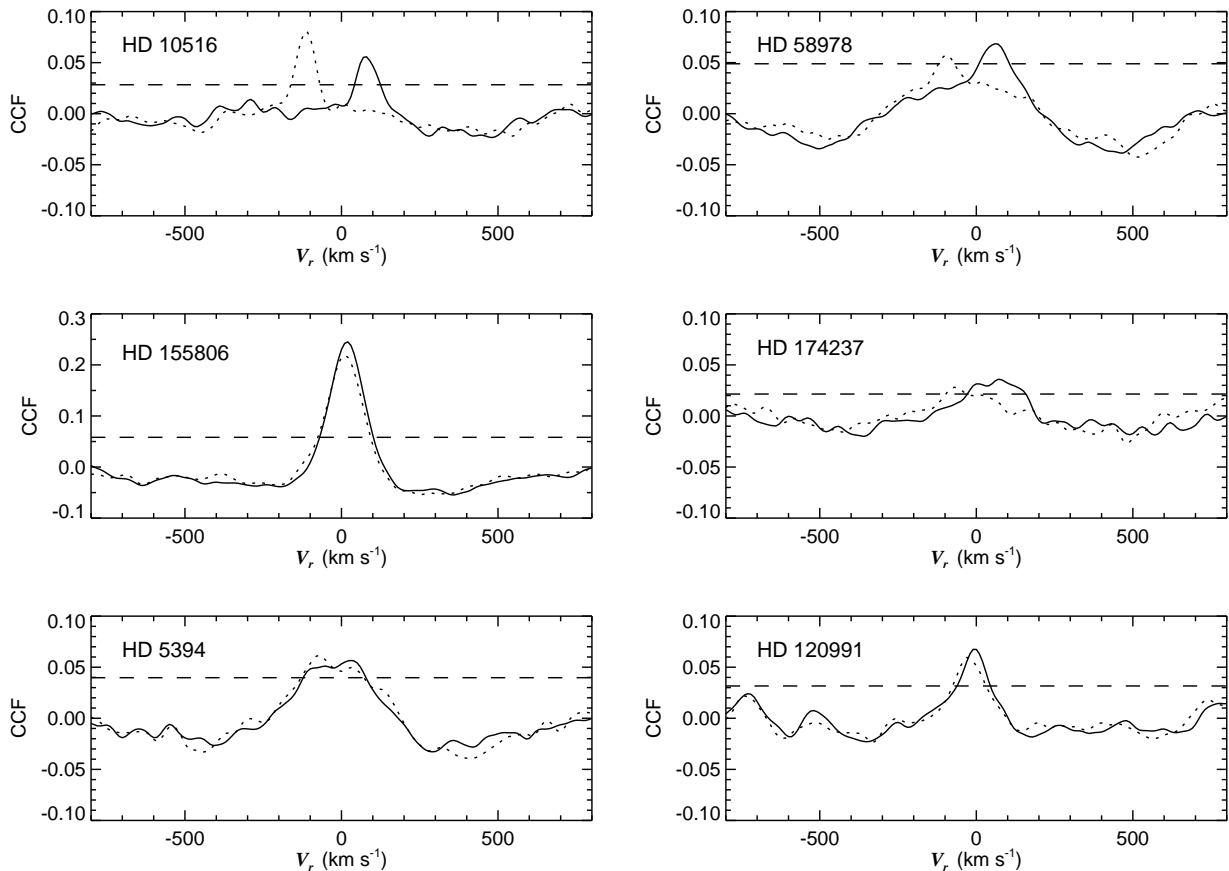


Figure 4.1: Example CCFs for two cases of hot component detection (top row) with several other cases where the peak is associated with the Be component (second and third rows). The top panels show the CCFs for HD 10516, a confirmed system with a hot subdwarf companion (Gies et al. 1998), and HD 58978, a confirmed system with a fainter subdwarf companion (Peters et al. 2008). The middle panels show how the spectrum of the emission-line star contributes more to the CCF for a hot star (HD 155806; O7.5 IIIe) than a mid-range temperature star (HD 174237; B4 IV(e)). The lower row illustrates how the CCF from the rapidly rotating Be component is usually very broad (HD 5394;  $V \sin i = 432 \text{ km s}^{-1}$ ), but sometimes narrow (HD 120991;  $V \sin i = 70 \text{ km s}^{-1}$ ). Examples of the CCFs for blue and red Doppler-shifted spectra are plotted as dotted and solid lines, respectively. The horizontal dashed lines indicate the  $S/N=3$  limit for detection.

The sensitivity of the CCFs to the temperature of the Be star means that it will become progressively more difficult to distinguish the signal from a sdO component from that of the Be star at high temperature, so our methods may be biased against detection of sdO companions among the hotter Be stars. Nevertheless, it is possible to discern the narrow sdO component against broader Be component in some cases of hotter Be stars (see the case of FY CMa = HD 53978 in the upper right panel of Fig. 4.1, which shows the narrow peak of the sdO star atop the broader signal from the Be star).

The second criterion is based upon the expected orbital motion of the sdO component. Post-mass transfer binaries are expected to have extreme mass ratios, so that the orbital semiamplitudes of the sdO components will be large ( $\approx 50 - 100 \text{ km s}^{-1}$ ) compared to those of the Be stars ( $< 10 \text{ km s}^{-1}$ ) for binaries with periods of a few months or less. Thus, my second criterion for sdO candidates is that their CCF signals should show a velocity range greater than 1/2 of the HWHM of the CCF peak. This criterion tacitly assumes that enough spectra exist to sample the full range of orbital motion, but this cannot be fulfilled in cases where only a few spectra are available. Note that application of this criterion will impose a bias against detection of binaries in low inclination and long period orbits (with small orbital semiamplitude).

### ***4.2.3 Detection of the Be+sdO systems***

The results of applying these two detection criteria are summarized in a code in the last column of Table 4.2. We find that 50 of the 66 targets in the list of large S/N cases are best explained as the result of correlation with the Be star spectrum itself (indicated by a “P”

for primary in Table 4.2). These are generally hotter Be stars in which the CCF signal has a half-width comparable to the published  $V \sin i$ , and their CCF peaks show little evidence of significant orbital Doppler shifts. Some of these cases are discussed in Appendix C. Next, the application of the two criteria led to the successful re-identification of four known Be+sdO binaries ( $\phi$  Per, FY CMa, 59 Cyg, and 60 Cyg), and these are indicated by an “S” (for subdwarf) in Table 4.2. The criteria also led to the detection of eight additional candidate Be+sdO binaries that are labeled with a “C” in Table 4.2. Finally, I list four systems in which a strong and narrow CCF peak was found, but only one or two spectra are available in the *IUE* archive so that I could not apply the second criterion of velocity variability. These four potential candidates are indicated by a “C?” code in Table 4.2. Radial velocities from Gaussian fits of the upper 80% of the CCF peaks are listed in Table 4.3 for these eight candidate and four potential candidate systems, but measurements from noisy spectra with weak CCF signals were omitted. The number and time distribution of these measurements are insufficient to find orbital periods and other elements, but they are included here for future use once orbits are determined (perhaps by ground-based spectroscopy of the Be components). All these new detections are discussed further in the next section.

Table 4.2: *IUE* Observations of sample stars

HD Number	Star Name	HIP Number	Spectral Classification	$V \sin i$ (km s <sup>-1</sup> )	Number of Observations	S/N Ratio	Spectral classification Reference	$V \sin i$ Reference	CCF Code <sup>a</sup>
Candidate and Known Be+sdO Systems									
10516	$\phi$ Per	8068	B1.5 V:e-shell	440	16	6.78	Slettebak (1982)	Frémat et al. (2005)	S
29441	V1150 Tau	21626	B2.5 Vne	311	1	3.77	Yudin (2001)	Yudin (2001)	C?
43544	...	29771	B3 V	256	1	5.51	Slettebak (1982)	Bragança et al. (2012)	C?
51354	QY Gem	33493	B3 Ve	306	2	5.39	Slettebak (1982)	Yudin (2001)	C?
58978	FY CMa	36168	B0.5 IVe	340	96	3.10	Slettebak (1982)	Peters et al. (2008)	S
60855	V378 Pup	36981	B3 IV	239	6	4.98	Slettebak (1982)	Frémat et al. (2005)	C
113120	LS Mus	63688	B2 IVne	307	3	4.35	Levenhagen & Leister (2006)	Yudin (2001)	C
137387	$\kappa^1$ Aps	76013	B2 Vnpe	250	4	5.21	Levenhagen & Leister (2006)	Frémat et al. (2005)	C
152478	V846 Ara	82868	B3 Vnpe	340	2	3.69	Levenhagen & Leister (2006)	Pogodin et al. (2012)	C
157042	$\iota$ Ara	85079	B2.5 IVe	340	4	4.09	Slettebak (1982)	Frémat et al. (2005)	C
157832	V750 Ara	85467	B1.5 Ve	266	2	4.21	Lopes de Oliveira & Motch (2011)	Lopes de Oliveira & Motch (2011)	C?
191610	28 Cyg	99303	B3 IVe	300	46	3.02	Slettebak (1982)	Frémat et al. (2005)	C
194335	V2119 Cyg	100574	B2 IIIe	360	4	4.54	Slettebak (1982)	Frémat et al. (2005)	C
200120	59 Cyg	103632	B1 Ve	379	193	3.34	Slettebak (1982)	Frémat et al. (2005)	S
200310	60 Cyg	103732	B1 Ve	320	23	4.69	Koubský et al. (2000)	Koubský et al. (2000)	S
214168	8 Lac B	111544	B1 IVe	300	20	3.03	Slettebak (1982)	Frémat et al. (2005)	C
Other Stars									
5394	$\gamma$ Cas	4427	B0.5 IVe	432	227	3.81	Slettebak (1982)	Frémat et al. (2005)	P
20336	BK Cam	15520	B2 (IV:)e	328	2	3.31	Slettebak (1982)	Frémat et al. (2005)	P
24534	X Per	18350	O9.5 III	293	43	3.75	Slettebak (1982)	Frémat et al. (2005)	P
28497	DU Eri	20922	B1 Ve	300	28	3.01	Slettebak (1982)	Frémat et al. (2005)	P
30076	DX Eri	22024	B2 Ve	168	24	3.30	Slettebak (1982)	Huang et al. (2010)	P
33328	$\lambda$ Eri	23972	B2 III(e)p	318	146	3.35	Slettebak (1982)	Frémat et al. (2005)	P
35411	$\eta$ Ori	25281	B1 V	20	19	10.28	Slettebak (1982)	De Mey et al. (1996)	P
36576	V960 Tau	26064	B1.5 IVe	265	11	3.14	Slettebak (1982)	Frémat et al. (2005)	P
37490	$\omega$ Ori	26594	B3 Ve	171	190	3.43	Levenhagen & Leister (2006)	Yudin (2001)	P
37674	...	26683	B5 V(n)	...	1	3.34	Houk & Swift (1999)	...	P
48917	FT CMa	32292	B2 V	205	5	3.48	Houk (1982)	Frémat et al. (2005)	P

Continued on next page

Table 4.2 – Continued from previous page

HD Number	Star Name	HIP Number	Spectral Classification	$V \sin i$ (km s <sup>-1</sup> )	Number of Observations	S/N Ratio	Spectral classification Reference	$V \sin i$ Reference	CCF Code <sup>a</sup>
50013	$\kappa$ CMa	32759	B2 IVe	243	3	4.55	Slettebak (1982)	Frémat et al. (2005)	P
50083	V742 Mon	32947	B2 Ve	170	2	3.90	Yudin (2001)	Frémat et al. (2005)	P
52918	19 Mon	33971	B2 Vn(e)	265	15	3.10	Houk & Swift (1999)	Huang et al. (2010)	P
53367	V750 Mon	34116	B0 IVe	86	4	11.05	Pogodin et al. (2006)	Yudin (2001)	P
54309	FV CMa	34360	B2 IVe	195	2	3.63	Slettebak (1982)	Frémat et al. (2005)	P
56014	EW CMa	34981	B3 III(e)p-shell	280	12	3.45	Slettebak (1982)	Frémat et al. (2005)	P
58050	OT Gem	35933	B2 Ve	130	4	3.65	Yudin (2001)	Frémat et al. (2005)	P
60848	BN Gem	37074	O8 Vpe	247	13	4.05	Yudin (2001)	Frémat et al. (2005)	P
66194	V374 Car	38994	B2.5 IVe	224	2	3.27	Slettebak (1982)	Yudin (2001)	P
67536	V375 Car	39530	B2 Vn	292	22	3.28	Houk & Cowley (1975)	Uesugi & Fukuda (1970)	P
68980	MX Pup	40274	B1.5 IVe	145	3	4.91	Slettebak (1982)	Frémat et al. (2005)	P
74455	HX Vel	42712	B2/3 IV/V	285	7	4.56	Houk (1978)	Uesugi & Fukuda (1970)	P
74753	D Vel	42834	B1/2 II/III(n)	288	1	3.47	Houk (1978)	Uesugi & Fukuda (1970)	P
78764	E Car	44626	B2 IVe	127	3	5.42	Slettebak (1982)	Yudin (2001)	P
88661	QY Car	49934	B2 IVe	237	14	3.71	Slettebak (1982)	Frémat et al. (2005)	P
93030	$\theta$ Car	52419	B0 Vp	145	33	8.68	Yudin (2001)	Yudin (2001)	P
96864	...	...	B1.5 IVnep	...	1	4.16	Yudin (2001)	...	P
105435	$\delta$ Cen	59196	B2 IVe	260	19	3.35	Slettebak (1982)	Frémat et al. (2005)	P
116781	V967 Cen	65637	B0 IIIne	...	1	7.55	Yudin (2001)	...	P
120324	$\mu$ Cen	67472	B2 Vnpe	159	36	4.62	Levenhagen & Leister (2006)	Frémat et al. (2005)	P
120991	V767 Cen	67861	B2 IIIep	70	5	6.09	Slettebak (1982)	Frémat et al. (2005)	P
135160	...	74750	B0 V	155	3	7.00	Slettebak (1982)	Yudin (2001)	P
148184	$\chi$ Oph	80569	B1.5 Ve	144	10	4.87	Slettebak (1982)	Frémat et al. (2005)	P
153261	V828 Ara	83323	B2 IVe	184	1	3.92	Yudin (2001)	Yudin (2001)	P
155806	V1075 Sco	84401	O7.5 IIIe	116	6	9.96	Slettebak (1982)	Yudin (2001)	P
166596	V692 CrA	89290	B2.5 IIIp	207	2	3.20	Yudin (2001)	Frémat et al. (2005)	P
170235	V4031 Sgr	90610	B1 Vnne	163	2	4.39	Levenhagen & Leister (2006)	Yudin (2001)	P
173219	V447 Sct	91946	B0 Iae	...	3	4.15	Houk & Swift (1999)	...	P
173948	$\lambda$ Pav	92609	B2 Ve	140	5	5.09	Levenhagen & Leister (2006)	Frémat et al. (2005)	P
174237	CX Dra	92133	B4 IV(e)	163	64	3.16	Slettebak (1982)	Frémat et al. (2005)	P

Continued on next page

Table 4.2 – Continued from previous page

HD Number	Star Name	HIP Number	Spectral Classification	$V \sin i$ (km s <sup>-1</sup> )	Number of Observations	S/N Ratio	Spectral classification Reference	$V \sin i$ Reference	CCF Code <sup>a</sup>
178175	V4024 Sgr	93996	B2 V(e)	86	6	5.51	Slettebak (1982)	Bragança et al. (2012)	P
184279	V1294 Aql	96196	B0 V	212	11	3.39	Levenhagen & Leister (2006)	Yudin (2001)	P
184915	$\kappa$ Aql	96483	B0.5 III	284	4	3.38	Slettebak (1982)	Simón-Díaz & Herrero (2014a)	P
187567	V1339 Aql	97607	B2.5 IVe	140	3	3.26	Yudin (2001)	Abt et al. (2002)	P
188439	V819 Cyg	97845	B0.5 III(n)	299	1	3.75	Lesh (1968)	Simón-Díaz & Herrero (2014b)	P
203374	...	105250	B0 IVpe	342	1	3.76	Yudin (2001)	Frémat et al. (2005)	P
212044	V357 Lac	110287	B0 Ve	162	1	4.33	Yudin (2001)	Yudin (2001)	P
212076	31 Peg	110386	B1.5 Ve	98	6	3.95	Slettebak (1982)	Frémat et al. (2005)	P
212571	$\pi$ Aqr	110672	B1 Ve	230	21	3.18	Mayer et al. (2016)	Frémat et al. (2005)	P

Note. Spectral classifications and projected rotational velocities are from Slettebak (1982) and Frémat et al. (2005), respectively. <sup>a</sup>S = known Be+sdO binary; C = candidate binary; C? = potential candidate binary; P = CCF signal from primary star.

### 4.3 Discussion of the candidate Be+sdO systems

I identified twelve subdwarf candidates from the CCF analysis that display a narrow peak as expected from correlation with the hot subdwarf spectrum template. I observe significant Doppler shift variations in the CCF signals of eight systems due to the orbital motion of the subdwarf companion. Figure 4.2 shows the apparent CCFs of the eight candidate systems for spectra observed near the velocity extrema (see Table 4.3). The remaining four potential subdwarf candidates in the sample display a narrow peak, but little or no information about their Doppler shifts is available due to the limited number of spectra available. The CCFs for these four cases are shown in Figure 4.3. The peak height of the CCF scales approximately with the subdwarf flux contribution if the model template is a reasonable match (Wang et al. 2017), so the new candidates contribute about 2 – 5% of the FUV monochromatic flux (and probably less at optical wavelengths).

None of the candidates are known close binaries, but all are worthy of follow-up investigation. I summarize a brief literature review for each candidate below. Many of the candidate Be+sdO systems have additional companions detected through speckle interferometry or optical imaging, but their orbital periods must be decades or longer. Consequently these visually resolved companions are unrelated to the subdwarf companions that are the remnants of interactions in close binaries. The speckle interferometry observations reveal companions in the angular separation range of  $0.035 < \rho < 1''.5$  and brighter than  $\Delta m < 3.0$  mag (Mason et al. 1997).

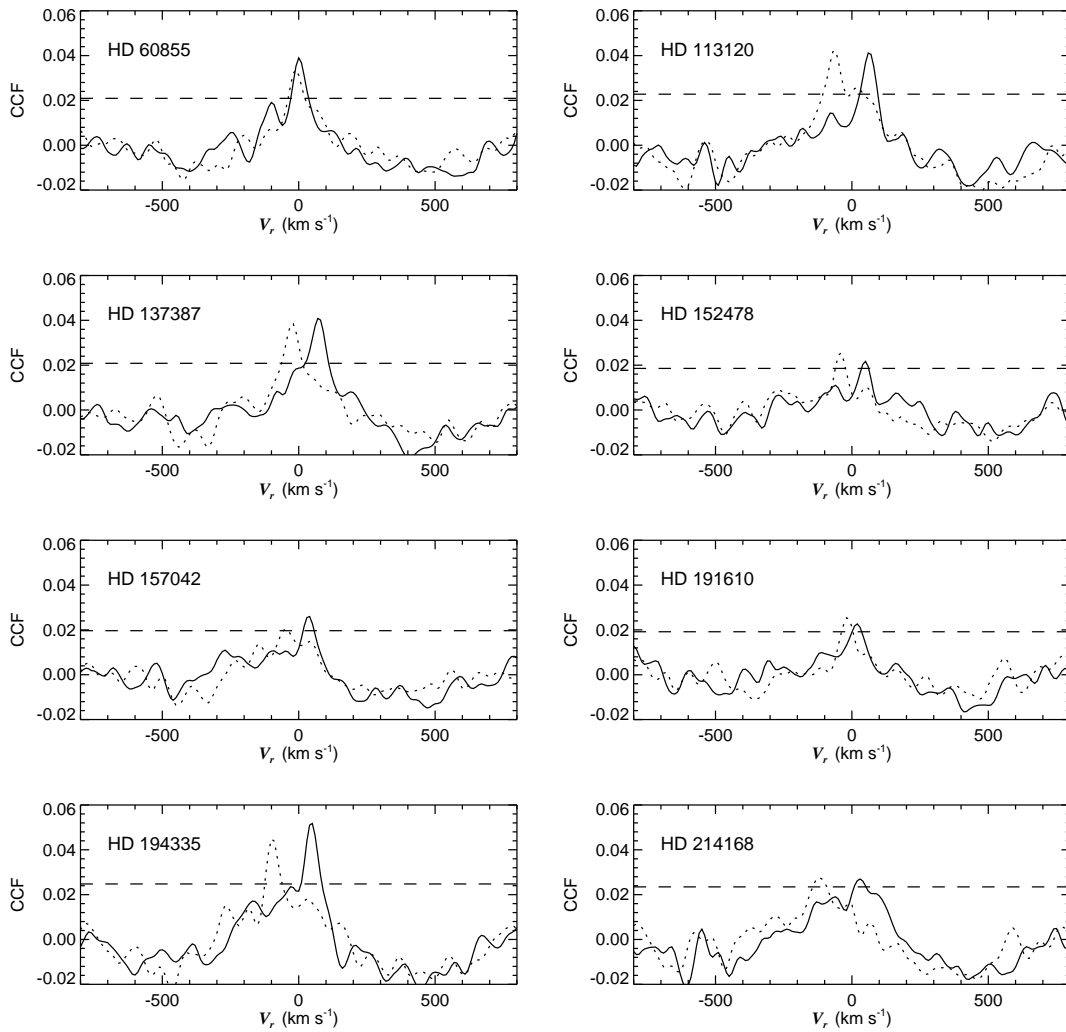


Figure 4.2: CCF plots of eight Be+sdO binary candidates in the same format as Fig. 4.1.

**HD 29441 (V1150 Tau; B2.5 Vne; S/N = 3.77).** Based on measurements of six optical spectra, Chini et al. (2012) found that the star is radial velocity constant, perhaps indicating that the sdO is a low mass object or that the orbit is very long.

**HD 43544 (B3 V; S/N = 5.51).** Huang et al. (2010) argued that the star had a significant radial velocity shift between measurements of two optical spectra, indicative of the orbital motion of the Be star. No other companions have been detected through speckle

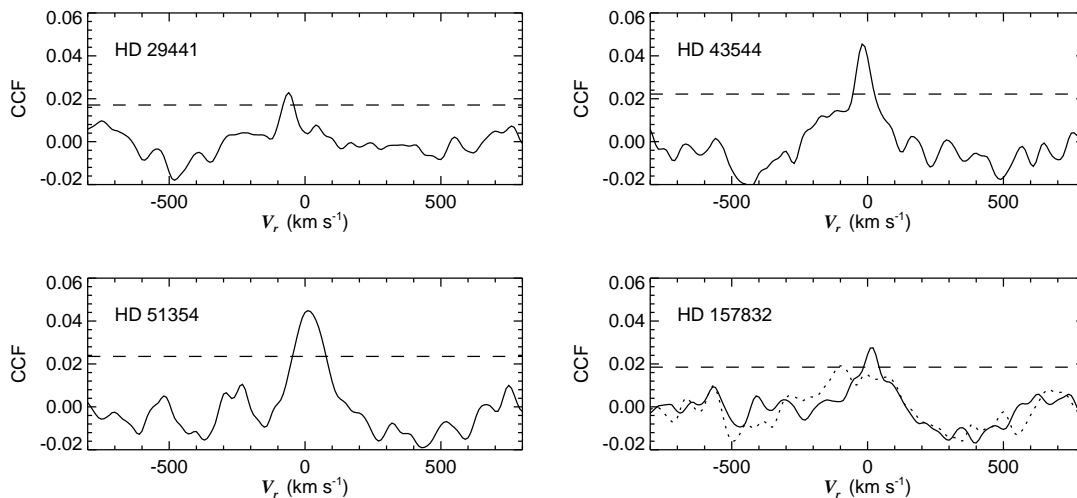


Figure 4.3: CCF plots of four potential Be+sdO binary candidates in the same format as Fig. 4.1.

interferometry from Mason et al. (1997).

**HD 51354 (QY Gem; B3 Ve; S/N = 5.39).** Chojnowski et al. (2017) observed only a small scatter of  $3.0 \text{ km s}^{-1}$  in six radial velocity measurements from the APOGEE survey.

**HD 60855 (V378 Pup; B3 IV; S/N = 4.98).** The CCFs of the star display a narrow central peak that sits atop a broader signal from the Be star. The measured velocities from the CCFs of the six available spectra did not display large velocity shifts, perhaps indicating that the sdO is in a long period, slow moving orbit. However, Huang & Gies (2006) found a significant velocity shift between their two spectra indicative of possible orbital motion of the Be star. Mason et al. (1997) found no evidence from speckle interferometry for another companion in the separation range of 0.04 to 1 arcsec. Mason et al. (2001) note that this star is a member of the NGC 2422 cluster, and the nearest companion has separation of 5.3 arcsec from the star.

**HD 113120 (LS Mus; B2 IVne; S/N = 4.35).** Based on spectroscopic measurements from five optical spectra, Chini et al. (2012) found that the star is radial velocity constant, which suggests a small orbital semi-amplitude for the Be star. Nevertheless, we observe relatively large Doppler shifts for the sdO component. Hartkopf et al. (1996) detected a companion with angular separation of 0.557 arcsec from the star through speckle interferometry.

**HD 137387 ( $\kappa^1$  Aps; B2 Vnpe; S/N = 5.21).** Lindroos (1985) reported that the star belongs to a visual binary system with a companion of estimated spectral type of K7 IV and a projected separation of 1470 AU from the star.

**HD 152478 (V846 Ara; B3 Vnpe; S/N = 3.69).** Hoogerwerf et al. (2001) mention this object as a possible runaway star. de Bruijne & Eilers (2012) list a radial velocity of 19 km s<sup>-1</sup>.

**HD 157042 ( $\iota$  Ara; B2.5 IVe; S/N = 4.09).** Based on optical studies Lindroos (1985) reported that the star has a companion with estimated spectral type of G5 III-IV and a separation of 42.8 arcsec from the primary component.

**HD 157832 (V750 Ara; B1.5 Ve; S/N = 4.21).** Based on observations from XMM-Newton and optical spectroscopy, Lopes de Oliveira & Motch (2011) classified the star as the coolest  $\gamma$  Cas analogue. Based on the presence of Fe XXI and Fe XXII recombination lines and fluorescence features, Giménez-García et al. (2015) confirmed the X-ray properties of the star and classified it as a component of high-mass X-ray binary.

**HD 191610 (28 Cyg; B3 IVe; S/N = 3.02).** Abt & Levy (1978) reported that the star

is radial velocity constant from spectroscopic studies based on 25 optical spectra. Based on an analysis of space photometry and  $H\alpha$  line profiles, Baade et al. (2016a) concluded that the large-amplitude frequencies due to multiple non-radial pulsation modes are responsible for the observed short- and medium-term variability, and these pulsation modes are also related to the modulation of mass transfer events from the star to the disk of 28 Cyg. No other companions have been found by Mason et al. (1997) through speckle interferometry.

**HD 194335 (V2119 Cyg; B2 IIIe; S/N = 4.54).** The star is listed as a shell star by Hoffleit & Jaschek (1991). Plaskett et al. (1920) suggested that the object is a possible spectroscopic binary.

**HD 214168 (8 Lac B; B1 IVe; S/N = 3.03).** Hoffleit & Jaschek (1991) also identified this star as a shell star. It is a member of the Lac OB1 association. Mason et al. (1997) identified a companion with an angular separation of 0.042 arcsec using speckle interferometry. Shatskii (1998) and Mason et al. (2007) confirmed that the star forms a double system with HD 214167 (B1.5 Vs) with an angular separation of 22.24 arcsec.

Table 4.3: Radial Velocity Measurements of Candidate sdO Components

HD Number	Date (HJD-2400000)	SWP Number	$V_{\text{peak}}$ (km s <sup>-1</sup> )	$\sigma$ (km s <sup>-1</sup> )
29441	49651.9145	52665	-60.7	2.5
43544	45698.7251	21911	-16.8	4.0
51354	45045.3074	16547	13.8	1.8
51354	45337.5616	18937	45.5	3.1
60855	45698.8371	21915	-10.4	3.1

Continued on next page

Table 4.3 – Continued from previous page

HD Number	Date (HJD-2400000)	SWP Number	$V_{\text{peak}}$ ( $\text{km s}^{-1}$ )	$\sigma$ ( $\text{km s}^{-1}$ )
60855	47654.3590	36216	2.1	3.8
60855	47808.0710	37280	-4.0	4.1
60855	47908.9317	38036	13.4	2.3
60855	48352.5316	41308	1.7	5.9
60855	49762.4824	53906	-4.2	5.8
113120	45602.3331	21155	63.8	3.2
113120	46710.9800	29397	-14.8	4.0
113120	46920.2862	30910	-64.1	4.7
137387	46225.1106	26120	-13.2	2.4
137387	46225.3690	26129	-12.1	2.0
137387	47717.4598	36649	73.1	3.3
137387	48346.7955	41240	-23.8	3.5
152478	47270.2997	33308	-42.6	5.5
152478	47652.3252	36197	48.3	4.7
157042	46527.3127	28114	19.7	5.4
157042	46711.9244	29404	25.3	4.5
157042	46920.4479	30914	36.2	8.0
157042	49442.3921	50427	-47.3	6.8
157832	49933.1996	55410	15.1	3.3
157832	49973.0096	55913	-97.6	8.9
191610	46245.3612	26301	-16.5	2.4
191610	46337.6586	26775	10.5	8.9
191610	46337.6830	26776	17.6	10.8
191610	46337.7275	26778	17.7	7.1
191610	46337.7501	26779	11.1	8.9
191610	46337.8480	26783	16.0	9.7
191610	46337.8987	26785	16.2	15.3
191610	46338.7622	26803	19.8	6.5
191610	46338.7881	26804	18.4	5.8
191610	46338.8322	26806	17.1	9.3
191610	46338.8545	26807	11.4	13.3
191610	46338.8767	26808	26.0	7.5
191610	46692.0815	29241	8.2	5.5
191610	47790.2654	37096	10.7	16.9

Continued on next page

Table 4.3 – Continued from previous page

HD	Date	SWP	$V_{\text{peak}}$	$\sigma$
Number	(HJD-2400000)	Number	( $\text{km s}^{-1}$ )	( $\text{km s}^{-1}$ )
191610	47790.3374	37098	8.5	4.7
191610	47791.2331	37124	15.9	10.6
191610	47791.3635	37128	21.3	16.4
191610	47791.4270	37130	3.5	11.8
191610	47791.5566	37134	14.5	5.8
191610	47791.6179	37136	8.0	13.4
191610	47791.7448	37140	3.3	12.1
191610	47791.8080	37142	12.4	14.7
191610	47792.0716	37148	8.4	16.5
191610	47792.2865	37150	18.2	6.5
191610	47792.4370	37154	6.7	5.9
194335	45463.4591	19938	46.3	6.5
194335	49349.8095	49705	-79.4	4.0
194335	49470.4343	50637	-96.1	9.3
194335	49686.9274	52946	29.5	3.9
214168	47691.1849	36479	-118.4	5.6
214168	47769.1105	36901	-32.9	2.3
214168	49296.6583	49099	2.3	3.6
214168	49296.7311	49102	8.3	7.3
214168	49296.7780	49104	2.4	6.5
214168	49298.6622	49130	3.0	2.8
214168	49298.7078	49132	21.2	5.3
214168	49299.6744	49145	23.4	5.8
214168	49299.7211	49147	21.6	5.0

#### 4.4 Population census of the identified Be+sdO candidate systems

I identified eight subdwarf candidates and four potential candidates, and by including the five Be+sdO systems known from previous studies, this leads to a total of 17 detections in the sample of 264 stars, for a detection rate of 6%. The CCF S/N ratios have a range

between 3.0 and 5.5 with a mean of 4.3, and these ratios are generally less than or comparable to those of the known systems. The distributions with spectral type of the known plus candidate targets and of the full sample are shown in Figure 4.4. Most of the new candidates have spectral types of B2-B3, which are relatively cooler compared to the primaries of the known Be+sdO systems with spectral types of B0.5-B1.5. However, I found no companions among the cooler, later-type B-stars, despite the fact that such hot companions should be more readily detected as they dominate more of the FUV flux distribution relative to cooler, main sequence companions. There are 109 targets with spectral types B4 and later in our sample (41%). If the Be+sdO systems had the same spectral type distribution as the whole sample, then I would expect to have found 7 of 17 systems among the B4-A0 group, yet none were detected among the cooler B-stars.

Binary star population models make different predictions about the numbers of expected Be+He star systems (which I may compare to the observed Be+sdO systems) as a function of Be star mass or spectral type. High mass He star remnants have relatively shorter lives, so the numbers of such systems are predicted to decline with higher Be star mass. On the other hand, lower mass remnants above the He-burning limit ( $\approx 0.3 M_{\odot}$ ) will have He-burning lifetimes longer than those of the rejuvenated gainer stars, so many lower mass Be stars could have He star companions. However, the expected numbers depend critically on assumptions about the initial mass ratio distribution of the binaries and which systems merge during interaction. Pols et al. (1991) show in their Figure 10(b) the numbers of Be+He systems expected for a magnitude limited sample like the Bright Star Catalogue (Hoffleit & Jaschek

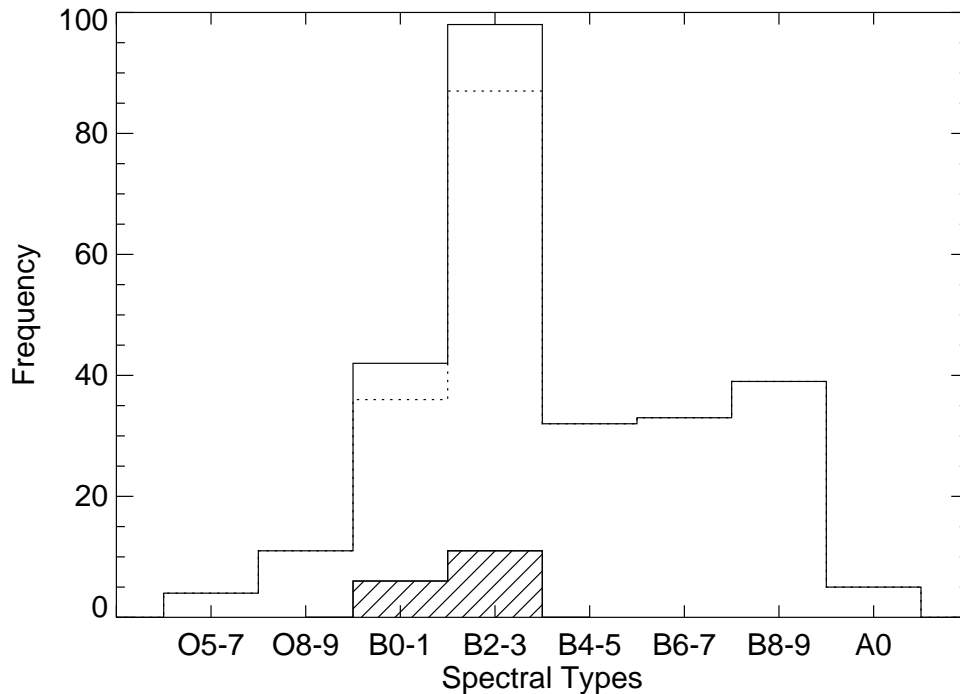


Figure 4.4: Histograms of the spectral type distributions of the full sample (solid line), those with no detections (dotted line), and those with known or candidate Be+sdO systems (line filled).

1991). If the initial mass ratio distribution is flat, then the numbers of Be+He systems peak in the B0-B5 range, because there are relatively fewer low mass systems. However, for initial mass ratio distributions that favor lower mass companions, the relative numbers of low mass Be+He systems increase. This is also seen in the simulations by Shao & Li (2014) who find the largest numbers of Be+He systems (in a volume limited sample) among the latest B-types when the assumed initial mass ratio distribution is highly skewed to low mass companions (numbers proportional to  $(M_2/M_1)^{-1}$ ; see their Fig. 7). The observed lack of Be+sdO companions among the late-type B-stars in our sample would appear to favor progenitor systems with a flat initial mass ratio distribution.

The low-mass, rapid rotators that comprise the late-type Be stars may be the result of mergers that occur more frequently among lower mass systems (Shao & Li 2014) or they may result from extreme mass transfer that creates low mass cores that quickly cool to become helium white dwarfs (Chen et al. 2017). Such low mass white dwarfs are now known to orbit some late B-type, rapid rotators including Regulus ( $0.3 M_{\odot}$ ; Gies et al. 2008), KOI-81 ( $0.2 M_{\odot}$ ; Matson et al. 2015), and possibly  $\beta$  CMi ( $0.4 M_{\odot}$ ; Dulaney et al. 2017).

If binary mass transfer is a significant mechanism in the production of Be stars, then I need to consider why hot companions are not found for all the B0-B3 stars in our sample. I suspect that many such companions spend much of their lives with a luminosity that is too low for detection by our methods. For example, Schootemeijer et al. (2018) present a path in the H-R diagram for the stripped remnant of HD 10516 ( $\phi$  Per) based on He star evolutionary models. They argue that the subdwarf companions in  $\phi$  Per, FY CMa, and 59 Cyg are most likely experiencing a late helium shell burning stage, in which the core has finished helium burning and the star swells to increased luminosity. This phase lasts about 10% of the total post-mass transfer lifetime. Thus, I expect that those stars that are bright enough to detect in this survey are representative of this advanced He-shell burning stage. The fraction of detected companions in B0-B3 range ( $17/140 = 12\%$ ) is close to the typical fraction of time spent in He-shell burning phase. On the other hand, 90% of the post-mass transfer lifetime is spent in the prior He-core burning stage, during which the subdwarfs have lower luminosity. These faint sdO companions are very difficult to detect unless a large set of spectra is available to reveal the orbital motion (for example, the case of HR 2142; Peters et al. 2016).

Consequently, it is possible that many or most of the B0-B3 stars in this sample do have sdO companions that are undetected because they are faint, He-core burning objects. Long term radial velocity and orbital-phase related emission line monitoring (Koubský et al. 2012) may prove to be effective ways to discover their binary properties.

## CHAPTER 5

### THE HOT SUBDWARF IN THE POST-MASS TRANSFER BINARY EL CVn

#### 5.1 Introduction

Over the last few years photometric surveys have revealed a class of post-mass transfer binaries that consist of a main sequence (MS) star and a hotter, smaller companion stripped of its H envelope. One of the first discoveries was made by Maxted et al. (2011) through the Wide Angle Search for Planets (WASP) photometric survey. They found that WASP 0247–25 displays a total eclipse of a small, hot star by a main-sequence A-type star. Photometry and spectroscopy revealed that the hot companion is a precursor to a low mass, He core, white dwarf (pre-He WD). Maxted et al. (2014) expanded the search through *WASP* and found another 17 similar eclipsing binaries with orbital periods between 0.7 – 2.2 d and with MS components with effective temperatures of 8800 – 15000 K. EL CVn is the brightest star in the sample, and it is the prototype of eclipsing binaries that consist of an A/F-type MS star and a low mass, helium star. The orbital period of EL CVn is 0.7956 d, and the brighter component has a spectral classification of A3 V (Maxted et al. 2014). The *Kepler* survey yielded another 13 EL CVn type systems, including KOI-74 (van Kerkwijk et al. 2010; Bloemen et al. 2012), KIC-10657664 (Carter et al. 2011), KOI-1224 (Breton et al. 2012), KIC-9164561, KOI-10727668 (Rappaport et al. 2015), KIC-4169521, KOI-3818, KIC-2851474, KIC-9285587 (Faigler et al. 2015), KOI-81 (Matson et al. 2015), KIC-8262223 (Guo et al. 2017), and KIC-8087799, KIC-10989032 (Zhang et al. 2017). Wang et al. (2018a) obtained photometry and spectroscopy of V1224 Cas and concluded that it is an EL CVn-type

binary consisting of a helium star and a MS companion displaying  $\delta$  Scuti-type pulsations. Recently, van Roestel et al. (2018) used supervised machine learning methods to search light curves from the Palomar Transient Factory, and they discovered 36 new EL CVn-type binaries. The radius and effective temperature ranges of these newly discovered helium star companions are  $0.3 - 0.7 R_{\odot}$  and  $8000 - 17000$  K, respectively.

The two main formation scenarios proposed for the EL CVn-type binaries are stable Roche-lobe overflow (RLOF) and unstable, rapid, common envelope evolution (CE). Based on calculations of binary evolution, Chen et al. (2017) argued that EL CVn-type binaries are likely formed from the stable mass transfer process instead of the CE one, because the latter generally leads to a merger of the components. The stable mass transfer scenario starts with two MS stars, and the more massive star evolves away from the main-sequence to become a red giant star. The system experiences RLOF as the massive donor star starts to transfer mass and angular momentum to the low mass gainer star. This process continues until the mass donor star loses its outer envelope and becomes a stripped red giant core (Maxted et al. 2011). Because it is not massive enough to ignite helium burning, the star undergoes H shell burning at nearly constant luminosity. After hydrogen consumption, the star will eventually fade to become a He-WD. Chen et al. (2017) applied the MESA binary evolution sequences and performed a Monte Carlo simulation for binary population synthesis. They estimated that EL CVn-type binaries with orbital period  $P \leq 2.2$  d comprise a population of about  $2 - 5 \times 10^6$  in the Galaxy. The EL CVn-type binaries discovered thus far represent a small portion of the population in the local galactic environment, so a large fraction remain to be

discovered in future photometric surveys. It is crucial to determine the physical properties of this type of binary system as tests to trace their evolutionary paths in the H-R diagram. The challenge is to measure the spectral features of the helium star directly in order to determine the orbital velocities and hence masses. Because the helium star components are hotter, their spectral contribution will be larger in the ultraviolet part of the spectrum, and the only detection so far was made through UV spectroscopy of KOI-81 by Matson et al. (2015). Here I present such a UV study that has revealed the helium star component in the prototype system EL CVn. I describe different sets of observations and their reduction procedures in Section 5.2, and analyses of the orbital radial velocity and light curves are presented in Sections 5.3 and 5.4, respectively. The orbital elements and masses are reviewed in Section 5.5, and the physical parameters derived from Doppler tomography reconstructions of the component spectra are discussed in Section 5.6. I consider the current evolutionary stage of the binary in Section 5.7, and summarize our findings in Section 5.8.

## 5.2 Observations and data reduction

I used three sets of observations to investigate the stellar features of EL CVn. These include far-UV (FUV) spectroscopic observations from the Hubble Space Telescope (*HST*), optical spectra from the Apache Point Observatory (*APO*), and optical light curves from the Roque de los Muchachos Observatory at La Palma. Details of each data set follow.

### 5.2.1 FUV HST/COS spectroscopy

I obtained the FUV spectra with *HST* using the Cosmic Origins Spectrograph (COS; Green et al. 2012). The spectra were made with the G160M grating that records the wavelength range 1405 – 1775 Å with a resolving power of 16000 – 21000. The spectrum is imaged onto two detector segments, B and A, with a gap of 21 Å between them. Four visits were executed between 2016 November 25 and December 1, and two observations were obtained each visit for central wavelengths of 1577 Å and 1600 Å. Each observation contained four sub-exposures with a total exposure time of 612 seconds. The FUV spectra were reduced and the observed flux and wavelength were calibrated using the standard COS pipeline from Fischer (2019). I used the IDL program `coadd_x1d.pro` from Danforth et al. (2010) to combine the four sub-exposures of every observation into a single spectrum in the barycentric frame. These spectra were subsequently transformed onto a uniform wavelength grid in  $\log \lambda$  steps equivalent to  $9.37 \text{ km s}^{-1} \text{ pixel}^{-1}$  and  $7.89 \text{ km s}^{-1} \text{ pixel}^{-1}$  for segments B and A, respectively. I did not attempt to remove any weak interstellar medium lines from the spectra. I formed matrices of all eight spectra (as functions of wavelength and time of observation) as separate data structures for the short wavelength (B) and long wavelength (A) ranges. I kept two versions of the spectra. The first set were rectified to a unit continuum by division of a spline fit of the relatively line-free regions. These rectified spectra were used to compute the radial velocities (Section 5.3). The second set were saved as absolute flux spectra, and these were used for reconstruction of the individual components and fitting the composite spectral energy distribution (Section 5.6). The spectrum observed on HJD 2457717.5985 for

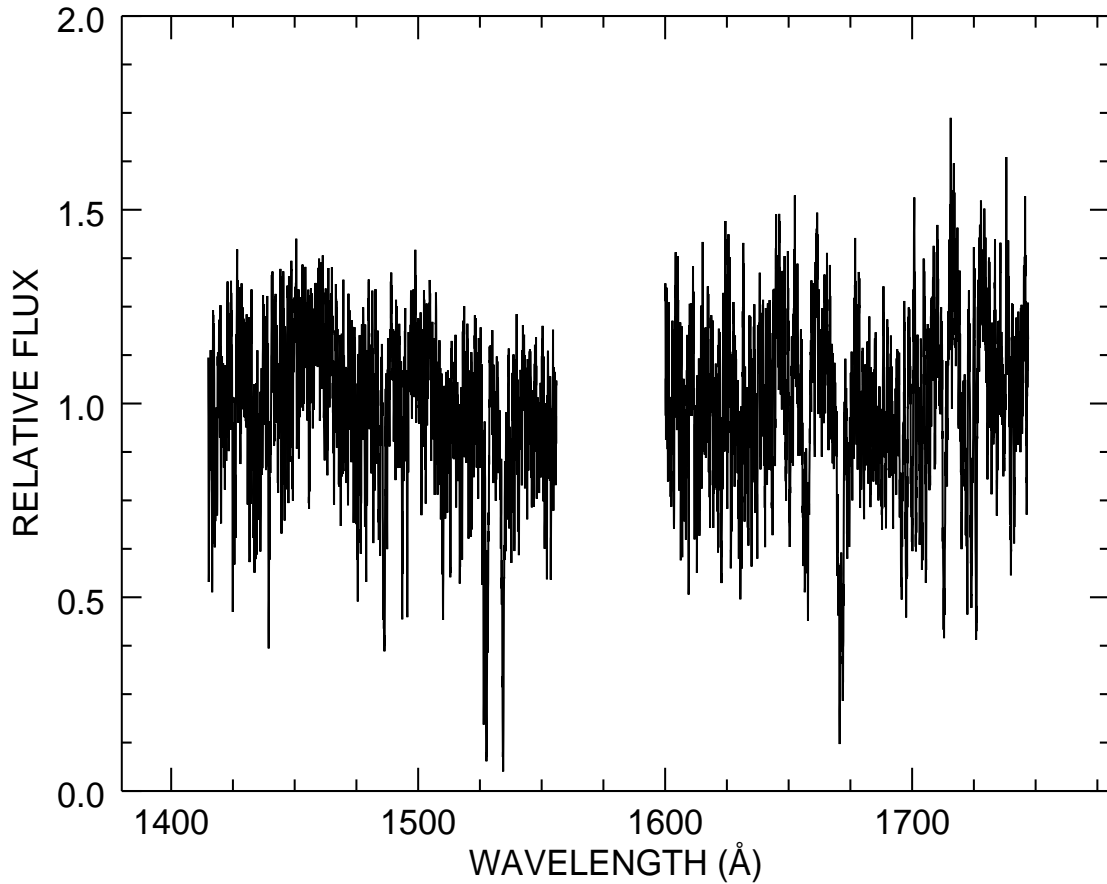


Figure 5.1: The rectified and normalized *HST*/COS spectrum observed on HJD 2457717.5985 in both short (B) and long (A) wavelength ranges.

both the short wavelength (B) and long wavelength (A) ranges is shown in Figure 5.1.

### 5.2.2 *Optical APO/ARCES spectroscopy*

I obtained eight optical spectra with the *APO* 3.5 m telescope and *ARC* Echelle Spectrograph (ARCES). These were made between 2017 February 16 and 2018 April 4. The ARCES instrument records the spectrum over the wavelength range of 3200 – 10000 Å on

a  $2048 \times 2048$  SITe CCD (Wang et al. 2003). These data have a spectral resolving power of  $R \sim 31500$ . I reduced the spectra following the standard *IRAF* procedures, including cosmic ray removal, bias subtraction, flat-fielding, aperture extraction and normalization, scattered light correction, wavelength calibration line identification, dispersion correction, and heliocentric correction. I transformed the spectra from each echelle order onto a log wavelength grid with step size of  $3.92 \text{ km s}^{-1}$  per pixel. I adopted the technique from Kolbas et al. (2015) to remove the residuals of the blaze function appearing in the spectra. The final spectra were rectified to a unit continuum and collected into a flux matrix as function of wavelength and time of observation. The spectrum of the echelle order recording the Mg II  $\lambda 4481$  line observed on HJD 2457800.9918 is shown in Figure 5.2.

### ***5.2.3 Optical PT5M light curves***

I obtained two optical light curves (LCs) from the 0.5 m robotic telescope (*pt5m*) located on the roof of the 4.2-m William Herschel Telescope building at the Roque de los Muchachos Observatory, La Palma (Hardy et al. 2015). The CCD has format of  $2184 \times 1472$  pixels with a plate scale of 0.28 arcsec per pixel. The observations were made on the nights of 2013 May 5 and 15 using an *I*-band filter, and each observation lasted for a duration of about 4 hours with individual exposure times of 20 sec and 5 sec of dead time between each exposure. These measurements recorded both of the mutual eclipses of the components. The *pt5m* data were reduced using the ULTRACAM pipeline software (Dhillon et al. 2007). The science frames were bias and dark subtracted, and then divided by a flat field obtained from images of a blank region of the twilight sky. Aperture photometry was then used to determine the total

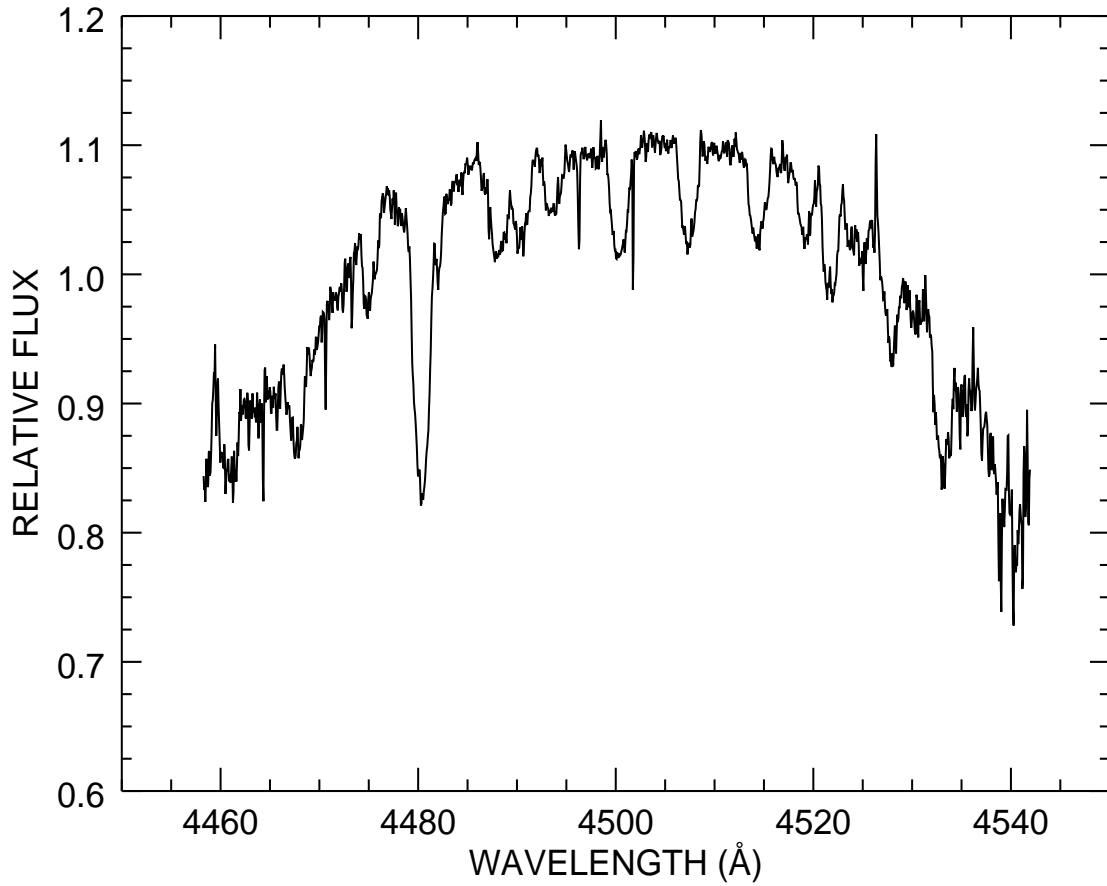


Figure 5.2: The *APO/ARCES* spectrum observed on HJD 2457800.9918 of the single echelle order recording Mg II  $\lambda 4481$ .

counts from the target and comparison stars, with the sky level estimated from an annulus surrounding each target aperture. The final result is a time series of relative magnitude as a function of heliocentric Julian date.

### 5.3 Radial velocity measurements

Based upon preliminary temperature estimates of the stars from Maxted et al. (2014), I expected that the short wavelength segment of the *HST*/COS spectra would be dominated by the flux of the hotter pre-He WD, and indeed I found that the spectral lines in that region resembled those of a late B-type star. On the other hand, the flux in the long wavelength segment of the *HST*/COS spectra is progressively more dominated by the light of the A-star. Consequently, I measured radial velocities for the pre-He WD star using only the short wavelength segment and those for the A-star using only the long wavelength segment.

I calculated the radial velocities using a cross-correlation function (CCF) algorithm described by Wang et al. (2017). I constructed individual model template spectra of both components using the UVBLUE grid of model fluxes that is based on Kurucz radiative transfer codes ATLAS9 and SYNTHE (Rodríguez-Merino et al. 2005). I adopted preliminary parameters of  $T_{\text{eff}} = 8250$  K and 12000 K and  $\log g = 4.0$  and 4.8 for the model spectra of the A-star and pre-He WD star, respectively. These model spectra are based upon solar abundances and a microturbulent velocity of  $2 \text{ km s}^{-1}$ . The model templates were rectified to a unit continuum in the same way as the *HST*/COS spectra, transformed onto the same  $\log \lambda$  wavelength grid, and smoothed according to the observed instrumental broadening. I then cross-correlated each observed spectrum of EL CVn with the model template spectrum, restricting the calculation to  $1646 - 1743 \text{ \AA}$  and  $1429 - 1502 \text{ \AA}$  for the A-star and pre-He WD star spectra, respectively. I measured the Doppler shifts of each stellar component from the location of the CCF maximum. The CCFs for each component for the spectrum observed

on HJD 2457717.5985 are shown in Figure 5.3 as an example of the procedure. The radial velocity measurements  $V_r$  and their associated uncertainties  $\sigma$  are collected in Table 5.1.

Table 5.1: Radial Velocity Measurements of EL CVn

Primary/ Secondary	Date (HJD-2400000)	Orbital Phase	$V_r^a$ (km s <sup>-1</sup> )	$\sigma$ (km s <sup>-1</sup> )	$(O - C)$ (km s <sup>-1</sup> )	Observation Source
P	57717.5985	0.5081	-74.84	3.40	1.68	<i>HST/COS</i>
P	57717.6148	0.5286	-74.93	3.64	1.16	<i>HST/COS</i>
P	57722.6693	0.8814	-28.70	3.14	-2.48	<i>HST/COS</i>
P	57722.7172	0.9416	-24.97	3.28	-4.51	<i>HST/COS</i>
P	57722.7900	0.0331	-15.98	3.47	3.18	<i>HST/COS</i>
P	57722.8526	0.1118	-29.56	2.98	-4.15	<i>HST/COS</i>
P	57723.8658	0.3853	-64.28	3.00	5.06	<i>HST/COS</i>
P	57723.9313	0.4676	-73.68	3.38	2.28	<i>HST/COS</i>
P	57800.9918	0.3226	-59.26	4.02	1.07	<i>APO/ARCES</i>
P	57801.0082	0.3432	-59.71	3.56	3.88	<i>APO/ARCES</i>
P	57821.7924	0.4663	-74.70	4.14	1.21	<i>APO/ARCES</i>
P	58089.9927	0.5591	-78.59	3.03	-4.01	<i>APO/ARCES</i>
P	58090.0258	0.6007	-72.49	2.63	-1.55	<i>APO/ARCES</i>
P	58146.9719	0.1746	-30.55	3.29	3.76	<i>APO/ARCES</i>
P	58147.0108	0.2235	-39.81	2.42	2.92	<i>APO/ARCES</i>
P	58212.7782	0.8845	-25.75	2.53	0.09	<i>APO/ARCES</i>
S	57717.5985	0.5081	184.72	1.25	-1.45	<i>HST/COS</i>
S	57717.6148	0.5286	184.95	1.21	2.27	<i>HST/COS</i>
S	57722.6693	0.8814	-220.18	1.51	3.20	<i>HST/COS</i>
S	57722.7172	0.9416	-269.97	1.26	0.27	<i>HST/COS</i>
S	57722.7900	0.0331	-284.54	1.24	-3.70	<i>HST/COS</i>
S	57722.8526	0.1118	-227.24	1.24	2.75	<i>HST/COS</i>
S	57723.8658	0.3853	122.28	1.34	-5.46	<i>HST/COS</i>
S	57723.9313	0.4676	181.10	1.23	-0.51	<i>HST/COS</i>
S	57821.7924	0.4663	186.06	2.07	4.86	<i>APO/ARCES</i>
S	58089.9927	0.5591	168.54	5.42	-1.82	<i>APO/ARCES</i>
S	58090.0258	0.6007	144.70	1.91	3.98	<i>APO/ARCES</i>
S	58212.7782	0.8845	-228.10	2.08	-1.65	<i>APO/ARCES</i>

<sup>a</sup> Offsets of  $\Delta\gamma = -0.35$  km s<sup>-1</sup> and  $\Delta\gamma = +2.93$  km s<sup>-1</sup> were added to the *APO/ARCES* measurements for the A star (P) and subdwarf (S), respectively, to place them in the *HST/COS* reference frame (see Section 5.3).

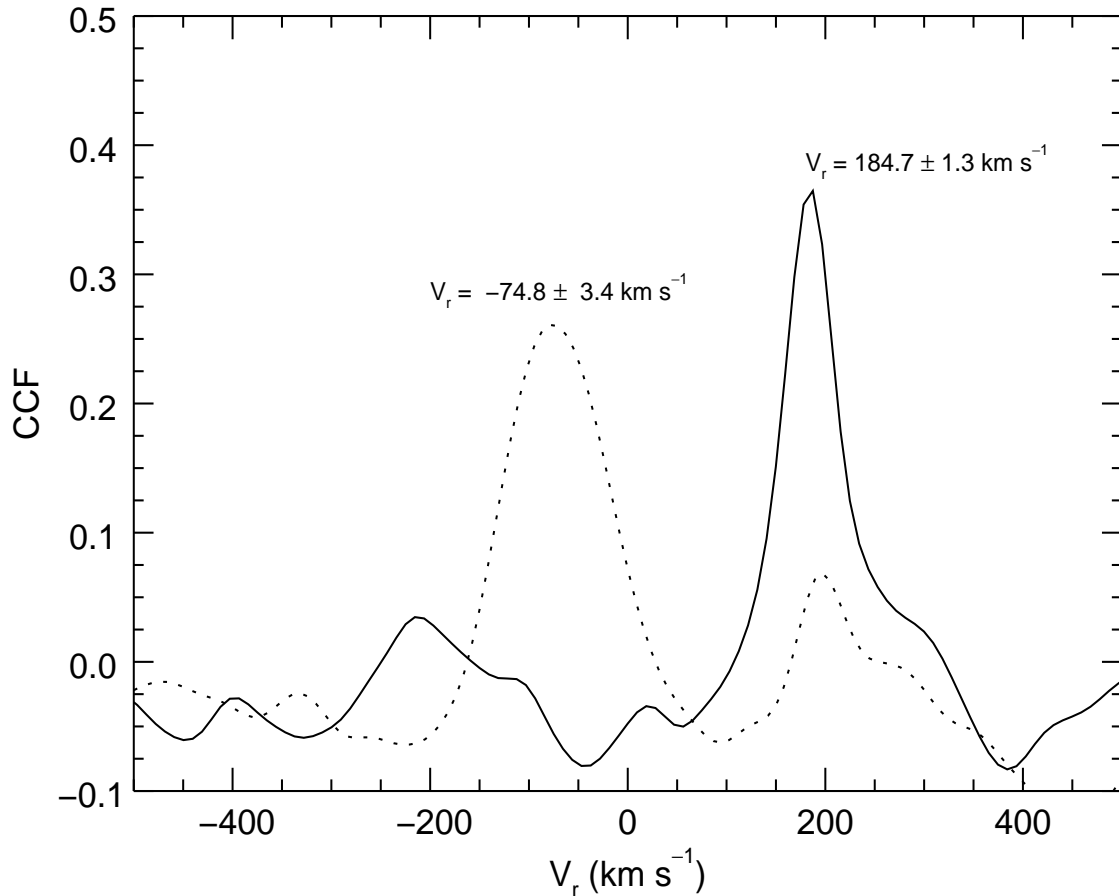


Figure 5.3: Plot of cross-correlation functions of EL CVn for each component from the *HST*/COS spectrum observed on HJD 2457717.5985. The CCF of the A-type component is plotted as a dotted line. The CCF of the pre-He WD companion is indicated as a solid line.

I also measured the radial velocities of both components using the optical spectra from *APO*. I formed a model spectrum of the A-star using the library of theoretical stellar spectra BLUERED from Bertone et al. (2008). I adopted the same parameters as adopted in the UV template spectra construction, and rectified and rebinned the spectrum in the same way as done with the *APO* spectra, and smoothed the model to the observed instrumental broad-

ening. Most of the echelle orders contain very weak metallic lines or very broad H-Balmer lines that are difficult to measure. In the end, I restricted the CCF measurements for the A-star to two echelle orders that contained the strong Ca I  $\lambda 4226$  and Mg II  $\lambda 4481$  lines.

I inspected the ARCES spectra and found that the only obvious line feature associated with the pre-He WD star is the Mg II  $\lambda 4481$  profile that displays the Doppler shifted components of both stars. I measured the line centroid of the component of the pre-He WD star in only those spectra with large velocity shifts where it was cleanly separated from the line component of the A-star.

The radial velocities from *HST*/COS and *APO*/ARCES will probably have systematic offsets because of the differences in spectral regions and measurement methods. Consequently, I made preliminary orbital velocity fits of each group separately in order to estimate any systematic offsets. I computed the circular orbital solution using the nonlinear, least-square technique from Morbey & Brosterhus (1974) by fixing the orbital period  $P$ , epoch of inferior conjunction of the A-star  $T_0$  (equal to the epoch of the light curve deeper eclipse; see Section 5.5), and semiamplitude  $K$ , and then solving for the systemic velocity  $\gamma$  alone. These estimates of systemic velocity are collected in Table 5.2 that includes a fit of 15 radial velocity measurements of the A-star from Maxted et al. (2014). The difference of derived systemic velocity for the A-star from that for *HST*/COS led to offsets of  $\Delta\gamma = -0.35 \text{ km s}^{-1}$  for the *APO*/ARCES measurements and  $\Delta\gamma = +11.43 \text{ km s}^{-1}$  for the Maxted et al. (2014) published measurements. Likewise, the difference of derived systemic velocity for the pre-He WD star from the *APO*/ARCES radial velocities led to an offset of  $\Delta\gamma = 2.93 \text{ km s}^{-1}$  from the

*HST*/COS measurements. These offsets were added to the *APO*/ARCES velocities that appear in Table 5.1 to place them in the same reference frame as the *HST*/COS measurements, which have smaller radial velocity uncertainties (Table 1). Table 5.1 lists the component (P for the A-star and S for the pre-He WD star), HJD of mid-exposure, orbital phase (Section 5.5), radial velocity, its uncertainty, the observed minus calculated (O-C) residual, and the observation source.

The final circular orbital elements were derived with fixed  $P$  and  $T_0$  (Section 5.5) by fitting all the available data in the *HST*/COS reference frame. The derived values of  $K$  and  $\gamma$  are presented for both stars in Table 5.2 along with the mass products and projected semi-major axis. The radial velocities and orbital velocity curves are shown in Figure 5.4. Note that the measured semiamplitude of the A-star,  $K_1$ , was not corrected for the effects of irradiation by the subdwarf, because any such effects are negligible given the low luminosity of the subdwarf, the comparable temperatures of the stars, and the lack of evidence of irradiation in the light curve (Maxted et al. 2014). I also derived the eccentric orbital elements of the radial velocities with the values from the light curve (Section 4), and I noticed that the fitted semiamplitudes for both components were the same between the circular and the eccentric orbit fits within errors. I finally decided to keep the results from the circular fit.

Table 5.2: Orbital elements of EL CVn

Element	Value
$P$ (days)	$0.79562735 \pm 0.00000014$
$T_{conj}$ (HJD-2,400,000)	$56418.5315 \pm 0.0003$
$K_1$ (km s <sup>-1</sup> )	$29.01 \pm 0.41$
$K_2$ (km s <sup>-1</sup> )	$236.21 \pm 1.06$
$\gamma_1$ [HST] (km s <sup>-1</sup> )	$-47.36 \pm 1.05$
$\gamma_1$ [APO] (km s <sup>-1</sup> )	$-47.01 \pm 1.25$
$\gamma_1$ [Maxted] (km s <sup>-1</sup> )	$-58.79 \pm 0.67$
$\gamma_1$ [Merged] (km s <sup>-1</sup> )	$-47.55 \pm 0.33$
$\gamma_2$ [HST] (km s <sup>-1</sup> )	$-49.86 \pm 1.12$
$\gamma_2$ [APO] (km s <sup>-1</sup> )	$-52.79 \pm 2.52$
$\gamma_2$ [Merged] (km s <sup>-1</sup> )	$-49.73 \pm 0.95$
$M_2/M_1$	$0.1228 \pm 0.0018$
$a \sin i$ ( $R_\odot$ )	$4.169 \pm 0.018$
$M_1 \sin i^3$ ( $M_\odot$ )	$1.370 \pm 0.013$
$M_2 \sin i^3$ ( $M_\odot$ )	$0.168 \pm 0.003$

#### 5.4 Light curve fit

Maxted et al. (2014) made a light curve analysis of EL CVn photometry from the WASP survey, and they reported the estimated parameters from fits with the JKTEBOP modeling code. I applied the ELC (Eclipsing Light Curve) code from Orosz & Hauschildt (2000) to the two eclipse observations made on 2013 May 5 and 2013 May 15 from the *pt5m* telescope (Section 2.3) that are illustrated in Figure 5.5. This photometry covers only the eclipse phases, so the phases between eclipses are missing and that show evidence of the tidal deformation of the A-star (see Fig. A1 in Maxted et al. 2014). On the other hand, the *pt5m*

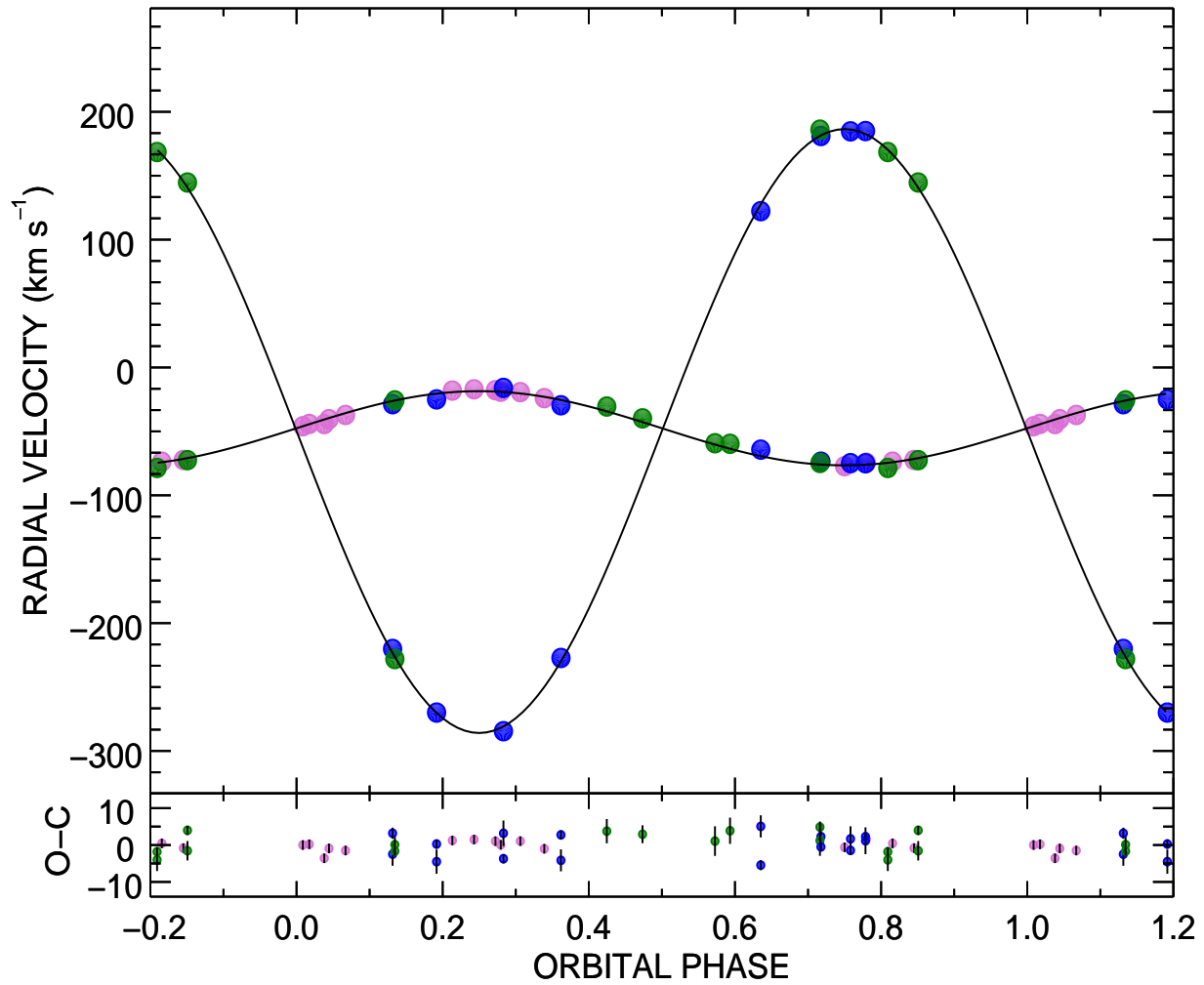


Figure 5.4: Radial velocity curve of EL CVn. In the top panel, the blue dots represent measurements from *HST*, green dots the measurements from *APO*, and published data from Maxted et al. (2014) appear as orchid dots. The bottom panel displays the difference between observed and calculated values. Orbital phase  $\phi = 0.0$  is the epoch when the A-type star reaches inferior conjunction.

photometry has approximately nine times faster cadence and three times more measurements during the eclipses than the WASP photometry presented by Maxted et al. (2014), so the new photometry is useful for a re-analysis of fitting parameters sensitive to details of the eclipses.

Our fits were made using the spectroscopic mass ratio and period (Table 5.2), and I fixed the A-star fractional radius to  $R_1/a = 0.346 \pm 0.012$  according to the results from Maxted et al. (2014). I tested the ELC fits over a grid of orbital inclination values, and I noticed that the best fit has  $i = 80.42^\circ$ . This is consistent with the value reported from Maxted et al. (2014) within their uncertainty range ( $i = 80.3^\circ \pm 1.8^\circ$ ). I thus adopted the published value. I then solved for four other parameter sets by finding the  $\chi^2$  minimum in each case. The first timing parameter is  $T_0$ , the epoch of A-star inferior conjunction (equal to the mid-point of the deeper eclipse), and the result is listed in Table 5.3. I noticed that the two eclipses were not exactly separated by half the orbital period, which indicates that the orbit has a non-zero eccentricity. I thus used the phase difference between eclipses (sensitive to  $e \cos \omega$ ) and the duration difference of eclipses (sensitive to  $e \sin \omega$ ) to optimize the fit (see appendices in Matson et al. 2016). The results are  $e \cos \omega = 0.0019 \pm 0.0005$  and  $e \sin \omega = -0.0149 \pm 0.0086$ . The durations of eclipse ingress and egress are sensitive to the fractional radius of the subdwarf, and the fits yield an estimate of  $R_2/a = 0.0671 \pm 0.0006$ . Finally, the relative eclipse depths are set by the ratio of surface brightness of the stars (dependent mainly on their effective temperatures), and the fits indicate  $T_2/T_1 = 1.44 \pm 0.04$ , where the uncertainty is due in part to the adopted absolute temperature values. The final

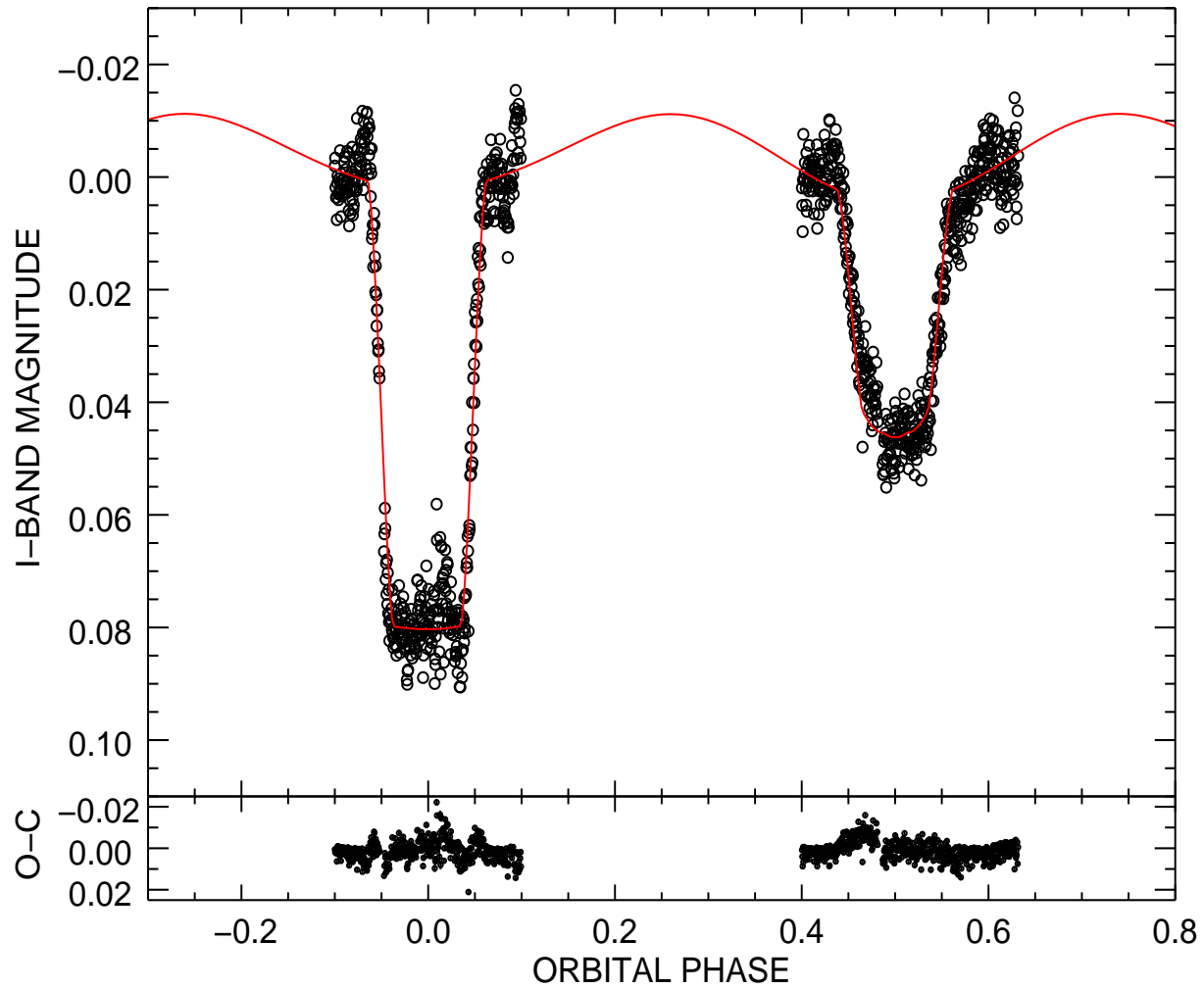


Figure 5.5: The top panel shows the light curve of EL CVn observed on the nights of 2013 May 5 and 15, and the ELC model fit is shown as a red solid line. The bottom panel displays the residuals between the observed and model light curves.

ELC model light curve based on these optimized parameters is shown in Figure 5.5.

### 5.5 Orbital elements, masses, and radii

I determined the orbital period by combining estimates of orbital epoch from published and our own values. For consistency, I define the zero phase as the epoch  $T_{conj}$  when the primary

A-type star reaches inferior conjunction. This phase reference is adopted throughout this work. The different sources of orbital epoch are collected in Table 5.3 that includes photometry from *Hipparcos* (Otero & Dubovsky 2004), WASP (Maxted et al. 2014), and *pt5m* (Section 5.4). I also include estimates from fits of subsets of the radial velocity measurements including those for the primary from McDonald Observatory spectra (Maxted et al. 2014) and from *HST*/COS and *APO*/ARCES spectra (Section 5.3) plus those for the secondary from *HST*/COS and *APO*/ARCES (Section 5.3). I calculated the number of orbits elapsed relative to  $T_{conj}$  from the *pt5m* photometry (column 3 of Table 5.3), and then I made a least-squares, linear fit of epoch as a function of orbit number (see Fig. 5.6). The derived slope and intercept yield the orbital period and global epoch, respectively (given in the first two rows of Table 5.2). The observed minus calculated ( $O - C$ ) epoch times are listed in column 4 of Table 5.3, and these are generally comparable to the uncertainties in the individual determinations of epoch (larger for the radial velocity sets). I adopted these  $P$  and  $T_{conj}$  values in the final iteration of the radial velocity orbital fit given in Table 5.2.

Table 5.3: Epochs of A-star Inferior Conjunction

Data	$T_{conj}$	$O - C$	Reference	
Source	(HJD-2,400,000)	Number	( $10^{-3}$ d)	Source
<i>Hipparcos</i> photometry	$48331.7780 \pm 0.0020$	-10164	2.9	Otero & Dubovsky (2004)
WASP photometry	$54230.5558 \pm 0.0005$	-2750	-0.4	Maxted et al. (2014)
McDonald $V_r(1)^a$	$55931.6128 \pm 0.0031$	-612	5.3	Maxted et al. (2014)
<i>pt5m</i> photometry	$56418.5313 \pm 0.0004$	0	-0.2	This work
COS and APO $V_r(1)^a$	$57723.3731 \pm 0.0047$	1640	12.8	This work
COS and APO $V_r(2)^b$	$57822.0195 \pm 0.0012$	1764	1.4	This work

<sup>a</sup> (1) is the subset of the radial velocity measurements for the primary.

<sup>b</sup> (2) is the subset of the radial velocity measurements for the secondary.

The inclination-dependent quantities in Table 5.2 may now be transformed to actual values by the adopting the orbital inclination  $i = 80.3^\circ \pm 1.8^\circ$  derived from the fit of the light curve by Maxted et al. (2014). Table 5.4 lists estimates for the semimajor axis  $a$  and the individual masses  $M_1$  and  $M_2$ . Next, the fractional radii from the light curve fits ( $R_1/a$  from Maxted et al. 2014;  $R_2/a$  from Section 5.4) may be multiplied by  $a$  to find the physical radii  $R_1$  and  $R_2$ . I find that both stars are well within their Roche radii,  $2.4 R_\odot$  and  $0.9 R_\odot$  for the A-star and subdwarf, respectively, despite the small dimensions of the orbit. Table 5.4 also lists the gravitational acceleration  $\log g$  derived from  $M$  and  $R$ . Finally, I can estimate the stellar angular diameters  $\theta$  from the ratio of the radius and distance, which is given as  $264.4 \pm 2.5$  pc from the GAIA DR2 results (Bailer-Jones et al. 2018). I will use these  $\theta$  values in the next section to help estimate the stellar effective temperatures.

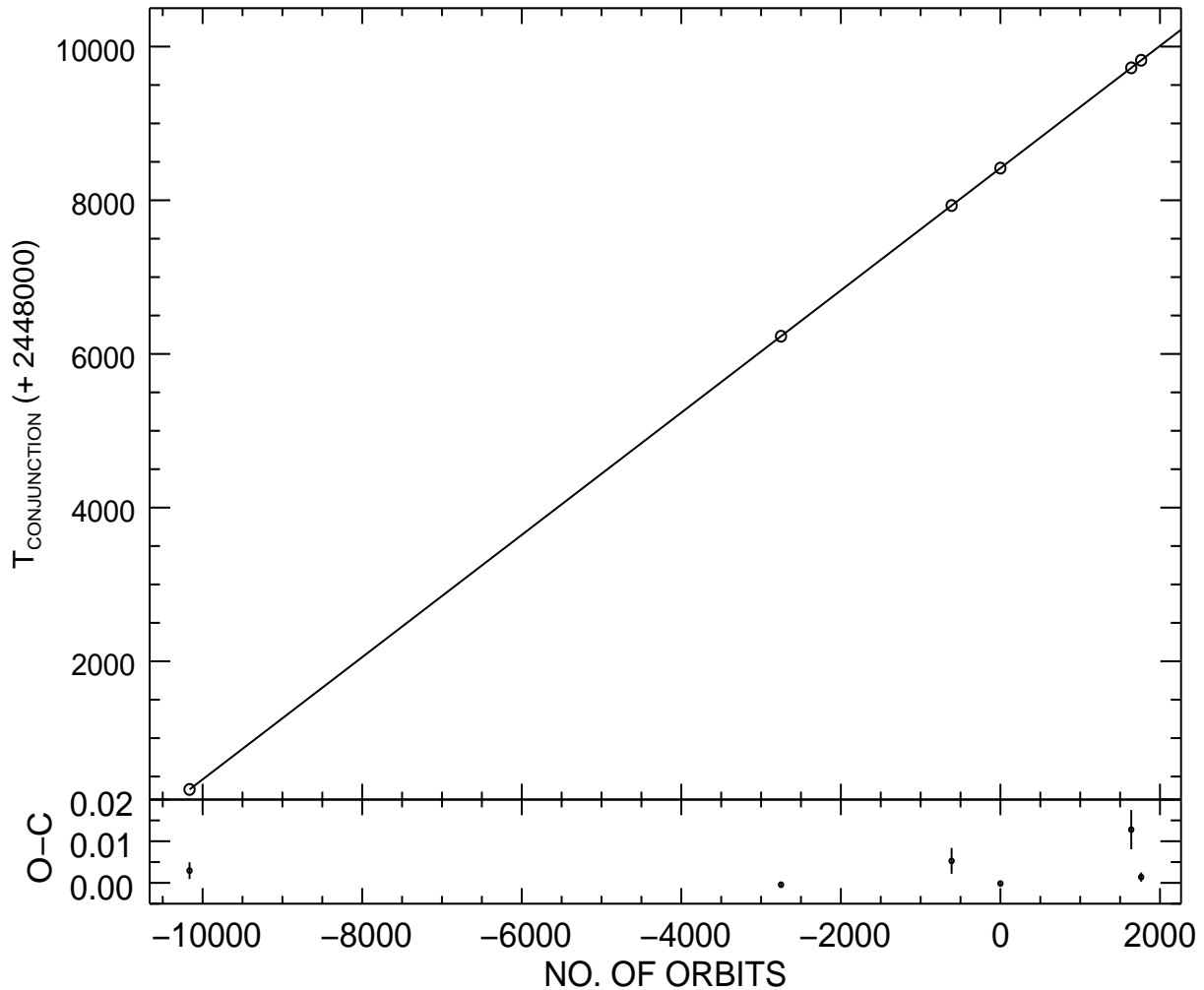


Figure 5.6: The top panel plots the epoch and orbit number of each data set in Table 3 and the corresponding, least-squares, linear fit. The derived slope (i.e., the orbital period) and intercept (global epoch) are listed in Table 2. The bottom panel displays the differences between the observed epochs and the fit.

## 5.6 Component Reconstructed Spectra and Physical Properties

The new *HST*/COS spectra contain a number of features that are important diagnostics of stellar temperature and other physical parameters. Here I present several methods to determine the effective temperatures and projected rotational velocities from both the com-

binned composite spectrum and the individual component spectra derived using a Doppler tomography reconstruction.

I begin by considering the temperatures implied by the absolute fluxes. Figure 5.7 shows the *HST*/COS spectrum from the first visit together with model spectra for both components (discussed below) rebinned to a lower resolution of  $R = 500$ . The subdwarf dominates the flux distribution at the low wavelength end, while the A-star becomes stronger beyond 1700 Å. The observed absolute flux  $f_\lambda$  is related to the emitted flux  $F_\lambda$  by

$$f_\lambda = \left(\frac{R}{d}\right)^2 F_\lambda 10^{-0.4A_\lambda} = \frac{1}{4}\theta^2 F_\lambda 10^{-0.4A_\lambda} \quad (5.1)$$

where  $\theta$  is the angular diameter and  $A_\lambda$  is the extinction. In the case at hand, I can estimate  $\theta$  from the physical radii (Table 5.4) and the distance from GAIA DR2,  $d = 264.4 \pm 2.5$  pc (Bailer-Jones et al. 2018). I adopted the extinction curve from Fitzpatrick (1999) and  $E(B-V) = 0.06$  and  $A_V/E(B-V) = 3.26$  from Gontcharov & Mosenkov (2018) to determine the wavelength dependent extinction  $A_\lambda$ . Then the observed fluxes can be directly related to the emitted fluxes that are primarily dependent on the effective temperature  $T_{\text{eff}}$ . I first created a least-squares fitting procedure that finds the best-fit angular diameters as a function of assumed temperatures based upon model spectra from the UVBLUE grid (Rodríguez-Merino et al. 2005), and then I used this procedure in an iterative scheme to find the temperatures associated with the estimated angular diameters given in Table 5.4. I adopted model spectra for the gravities listed in Table 5.4 and for metallicities of  $[M/H] = -0.5$  and 0.0 for the subdwarf and A-star, respectively (see below), but the results were relatively insensitive to metallicity. The temperature estimates from the absolute flux and angular

diameter are listed as  $T_{\text{eff}}(\theta)$  in Table 5.4, and the corresponding model spectral fit is shown in Figure 5.7. The quoted errors are based upon uncertainties in the *HST*/COS flux calibration, stellar radii, and distance, but the largest factor is the assumed extinction. For example, Maxted et al. (2014) adopted a lower reddening of  $E(B - V) = 0.02$ , and fits using this reddening led to temperatures that were lower by approximately the errors given for  $T_{\text{eff}}(\theta)$  in Table 5.4.

The next estimate of the subdwarf temperature comes from a comparison of the details of line spectrum. I reconstructed the individual component spectra of EL CVn using the Doppler tomography technique described by Bagnuolo et al. (1994). This method assigns a radial velocity to each spectrum from the adopted orbital elements (Table 5.2) and uses initial flux estimates based upon reddened UVBLUE models. The routine then uses an iterative correction scheme to find the individual spectra of the A-star and subdwarf. The tomography algorithm is very sensitive to the details of the line spectra, but less so to the shape of the continuum. Consequently, at the conclusion of the iterations I fit a fourth-order polynomial to the ratio of the high resolution versions of the reconstructed spectra to the model spectra, and then divided by this fit to facilitate a direct comparison of the line features in the reconstructed and model spectra. I repeated this comparison over a grid of temperature values and for the low and high wavelength segments separately, and a best-fit temperature  $T_{\text{eff}}(\text{spectrum})$  was found from the minimum position of the  $\chi^2_{\nu}$  residuals between the reconstructed and model spectra. The results of these trials are reported in Table 5.5. I found that the solar abundance models  $[M/H] = 0.0$  predicted lines that

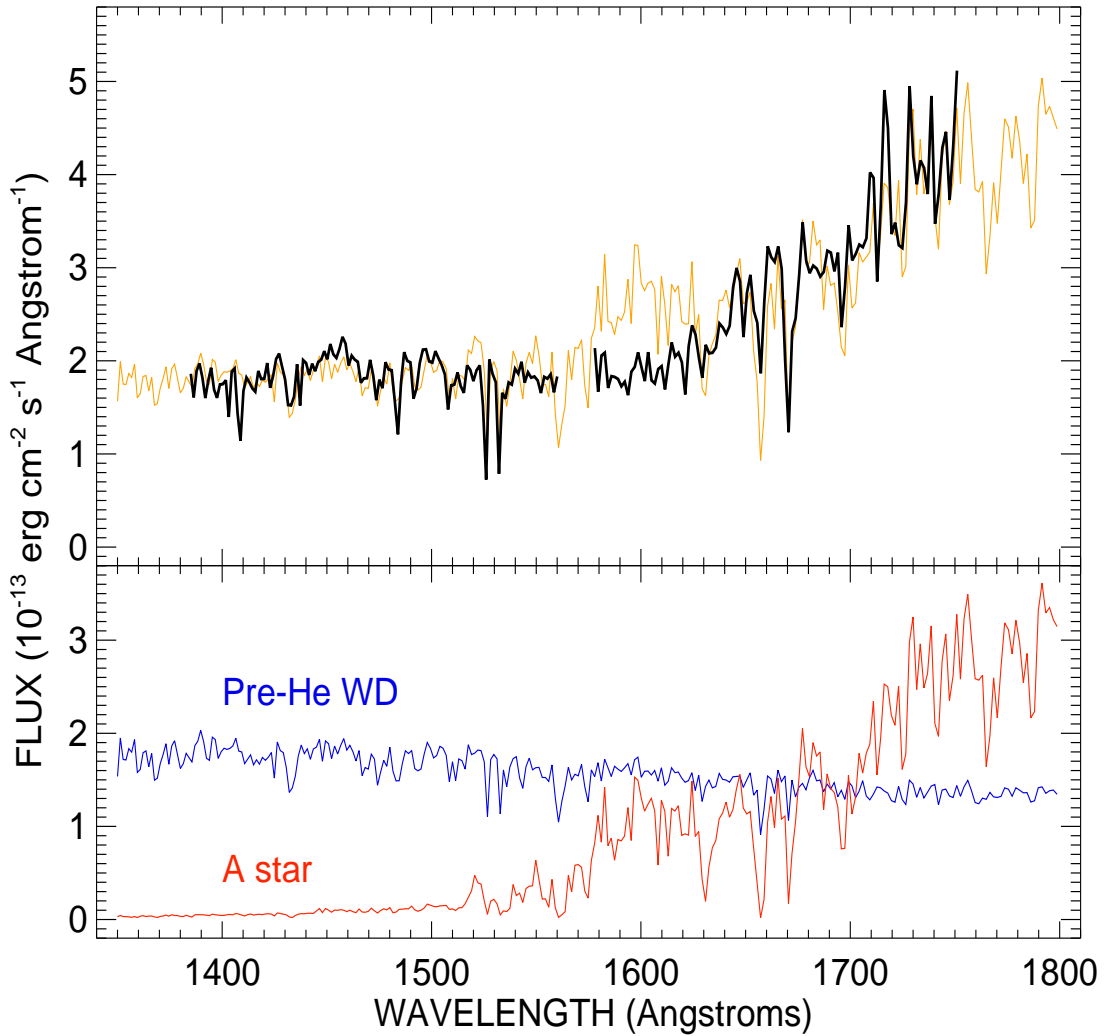


Figure 5.7: The top panel shows a rebinned, low resolution version of the *HST/COS* spectrum in black observed on HJD 2457717.5985 with the sum of the model spectra for both components in orange. The bottom panel shows the individual model spectra as described in Section 5.6 (for metallicities of  $[M/H] = 0.0$  and  $-0.5$  for the A-star and subdwarf, respectively).

were systematically too deep compared to those in the observed spectrum, and this led to a temperature that was much hotter than expected. I subsequently experimented with some of the lower metallicity models in the UVBLUE grid, and the best results in both wavelength segments were obtained with  $[M/H] = -0.5$  (Table 5.5). The average temperature from the fits in both segments is listed in Table 5.4 as  $T_{\text{eff}}(\text{spectrum})$ . This estimate of the subdwarf temperature agrees within errors with both that from the angular diameter method  $T_{\text{eff}}(\theta)$  and that from the composite fit of the spectral energy distribution made by Maxted et al. (2014) of  $T_{\text{eff}} = 12000 \pm 900$  K. The reconstructed and model spectra of the subdwarf with derived  $T_{\text{eff}}(\text{spectrum})$  are plotted in the panels of Figures 5.8 and 5.9.

The absorption line patterns of the A-star spectrum in the long wavelength segment were harder to match in detail as a temperature diagnostic. However, the shape of the spectral energy distribution and the wavelength where significant flux first appears are very sensitive to the assumed temperature. Consequently, I made comparisons of low resolution versions of the reconstructed and model spectra in the long wavelength segment to explore the variation with temperature. The comparison was made over a grid of assumed temperature to find the solution with the lowest  $\chi^2_{\nu}$ , and these best-fit estimates of  $T_{\text{eff}}(\text{spectrum})$  are given in the lower part of Table 5.5. Although sub-solar metallicity models made better fits, I adopted the solar metallicity temperature for the A-star because the lower temperatures associated with lower metallicities yield temperature ratios  $T_2/T_1$  that are much larger than that derived from our fit of the eclipse depths in the light curve (Section 5.4). This value of  $T_{\text{eff}}(\text{spectrum})$  (Table 5.4) agrees within errors with estimates from the angular size method

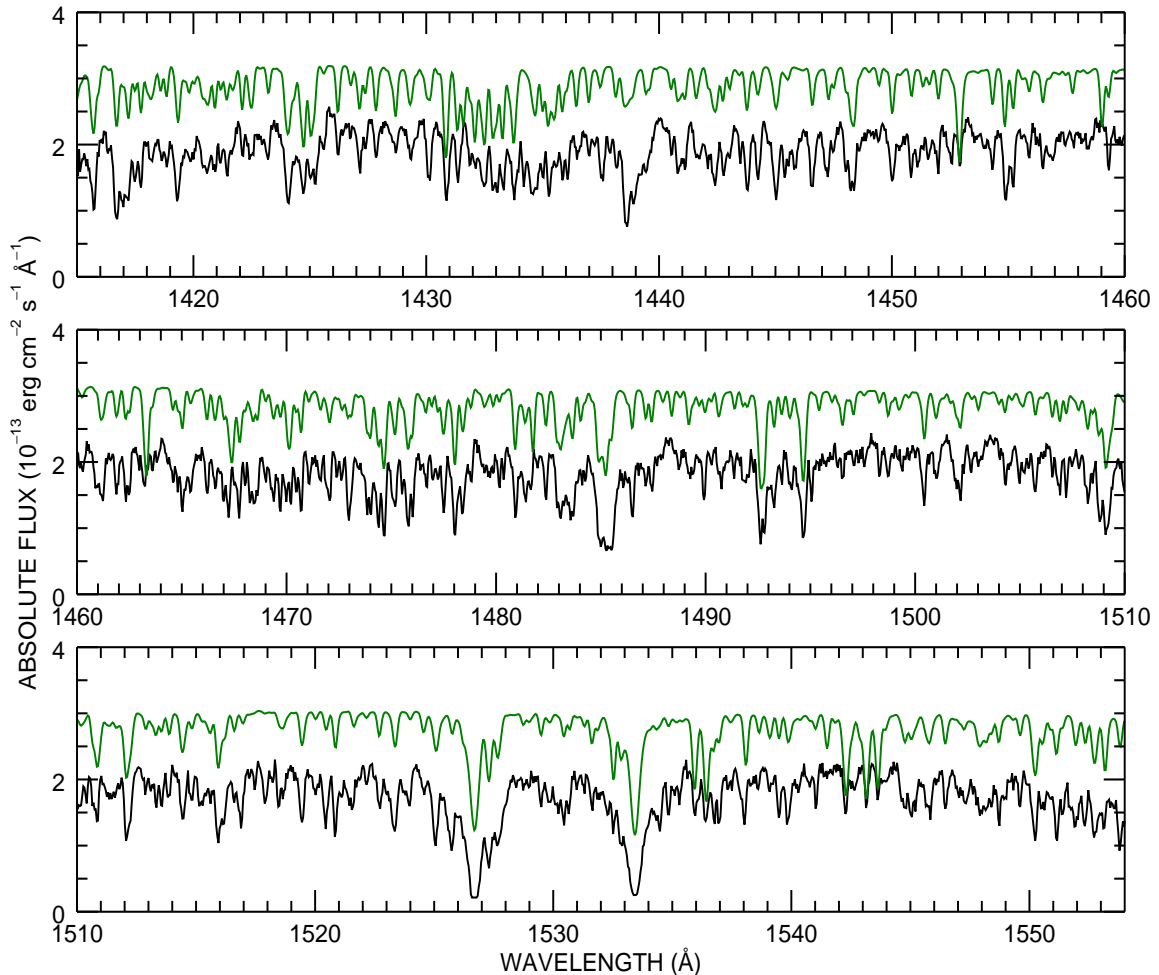


Figure 5.8: The reconstructed spectrum of the pre-He WD component of EL CVn based upon the *HST*/COS short wavelength data. I plot the absolute flux of the reconstructed pre-He WD spectrum in black and the model spectrum in green ( $[M/H] = -0.5$ ; offset by  $+1.0 \times 10^{-13}$ ).

and from Maxted et al. (2014) of  $T_{\text{eff}} = 8250 \pm 350$  K. Figure 5.10 shows the reconstructed spectra of the A-star from the long wavelength segment. The A-star flux was too low and the resulting S/N too small in the short wavelength segment for reliable feature identification.

I estimated the rotational broadening velocity by creating grids of UVBLUE model spec-

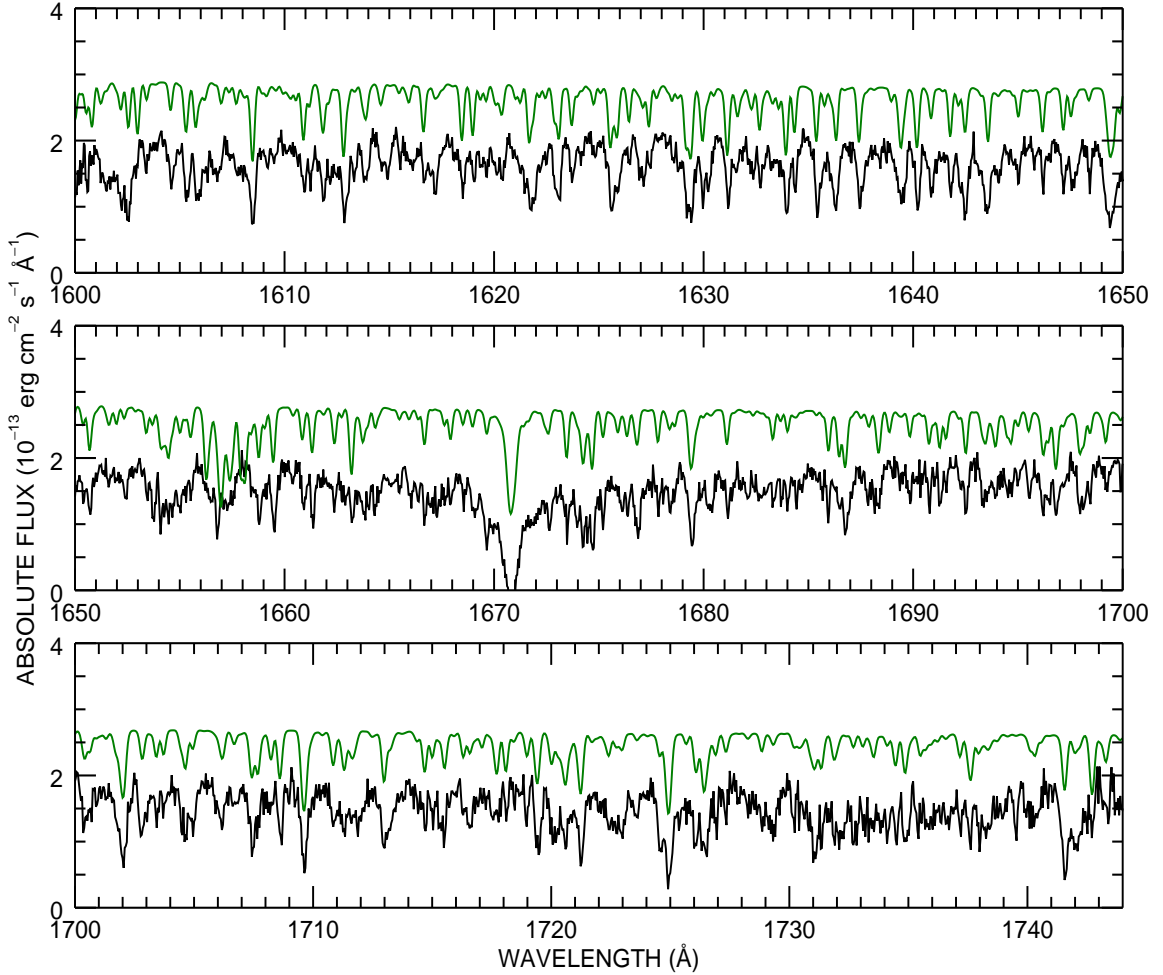


Figure 5.9: The reconstructed spectrum of the pre-He WD component of EL CVn based upon the *HST*/COS long wavelength data. I plot the absolute flux of the reconstructed pre-He WD spectrum in black and the model spectrum in green ( $[M/H] = -0.5$ ; offset by  $+1.0 \times 10^{-13}$ ).

tra convolved with a rotational broadening function for projected rotational velocity  $V \sin i$  in range of 0 to 110 km s $^{-1}$  with an increment of 5 km s $^{-1}$ . The broadened model spectra were compared with the reconstructed FUV spectra to form a distribution of reduced  $\chi^2_\nu$  as a function of  $V \sin i$ . The result for the A- star is  $V \sin i = 64.4 \pm 1.1$  km s $^{-1}$ . On the

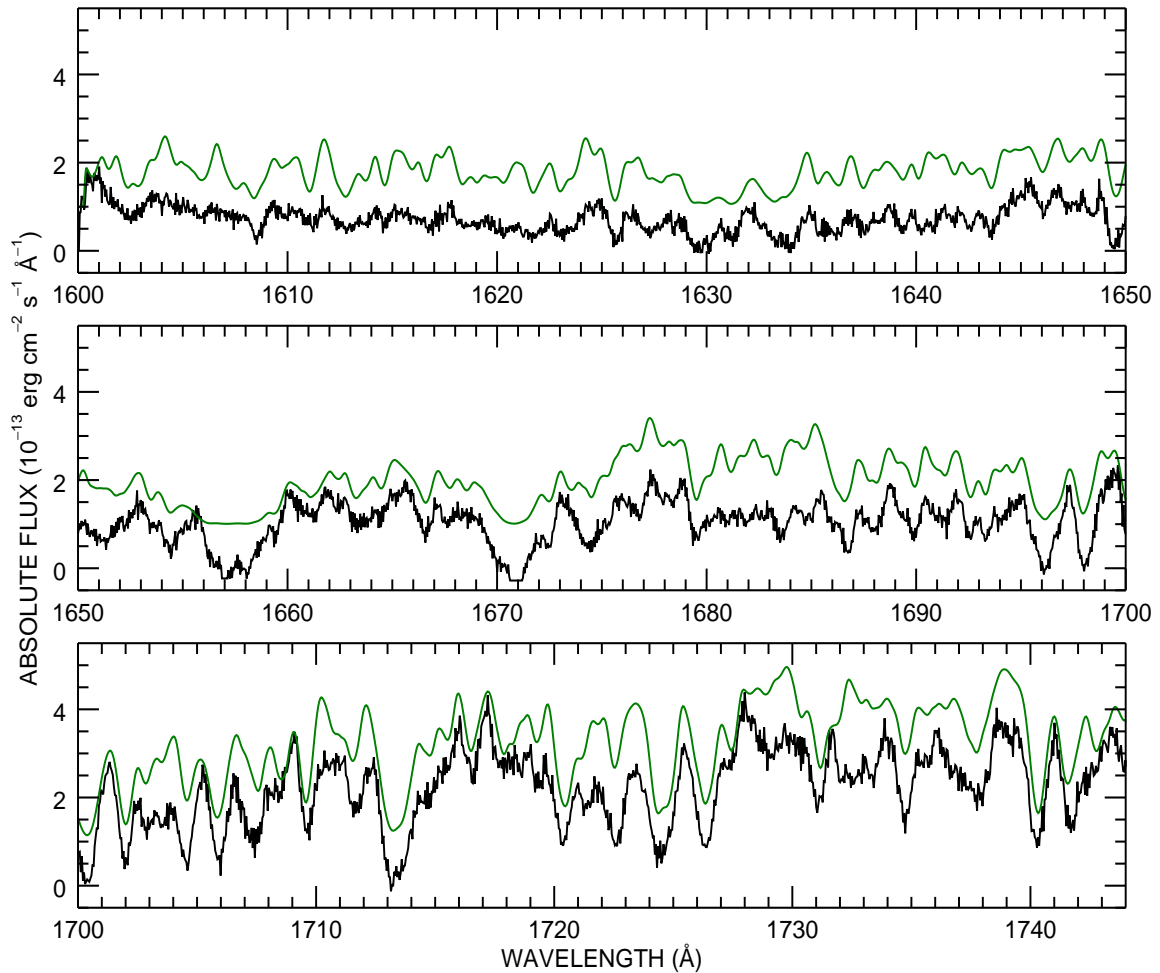


Figure 5.10: The reconstructed spectrum of the A-star component of EL CVn based upon the *HST*/COS long wavelength data. I plot the absolute flux of the reconstructed A-star spectrum in black and the model spectrum in green ( $[M/H] = 0.0$ ; offset by  $+1.0 \times 10^{-13}$ ).

other hand, the reduced  $\chi^2_\nu$  of the fits for the subdwarf spectrum indicated only an upper limit, i.e., the rotational broadening was unresolved in the *HST*/COS spectra. I also applied the Doppler tomography algorithm to the optical *APO*/ARCES spectra to reconstruct the spectral components in a few of the echelle orders. The observed and model spectra were rectified through fits of the line-free continuum regions. Once again the radial velocities

were taken from the orbital fit, but the flux ratio was fixed according to the radius ratio (Table 5.4) and the BLUERED model fluxes (Bertone et al. 2008). Figure 5.11 plots the reconstructed spectra in the vicinity of the Mg II  $\lambda 4481$  feature.

I estimated  $V \sin i$  for the optical spectra in two regions that contained a number of relatively sharp spectral lines. This was accomplished by forming the CCF of a rotationally broadened model spectrum with a  $V \sin i = 0 \text{ km s}^{-1}$  model spectrum, and then deriving the relationship between the CCF full width at half maximum (FWHM) and assumed  $V \sin i$ . Interpolation in this function at the FWHM of the CCF of the reconstructed and zero velocity model spectra led to our estimate of  $V \sin i$ . I arrived at estimates for the A-type star of  $V \sin i = 64.3 \pm 1.8 \text{ km s}^{-1}$  from Ca I  $\lambda 4226$  region and  $V \sin i = 68.1 \pm 2.2 \text{ km s}^{-1}$  from the Mg II  $\lambda 4481$  area. The final average of the *HST*/COS and *APO*/ARCES measurements is a projected rotational velocity of  $V \sin i = 64.8 \pm 1.0 \text{ km s}^{-1}$ . The model A-star spectra shown in Figures 5.8 – 5.11 are based upon this value. Estimates of the predicted synchronous projected rotational velocities are given in the final row of Table 5.4, and it appears that the A-star is rotating at only  $\approx 71\%$  of the synchronous rate. This is unusual but not unprecedented among short period binaries (Lurie et al. 2017).

Table 5.4: Physical Properties

Quantity	A-star	Pre-He WD
$M (M_{\odot})$	$1.430 \pm 0.027$	$0.176 \pm 0.004$
$R (R_{\odot})$	$1.46 \pm 0.05$	$0.284 \pm 0.003$
$\log g (\text{cm s}^{-2})$	$4.26 \pm 0.04$	$4.77 \pm 0.02$
$\theta (\mu\text{arcsec})$	$51.5 \pm 1.9$	$9.98 \pm 0.13$
$T_{\text{eff}}(\theta) (\text{K})$	$8159 \pm 135$	$11636 \pm 420$
$T_{\text{eff}}(\text{spectrum}) (\text{K})$	$8048 \pm 50$	$11890 \pm 490$
$V \sin i (\text{km s}^{-1})$	$64.8 \pm 1.0$	$< 20$
Synchronous $V \sin i (\text{km s}^{-1})$	91	18

Our initial inspection of *APO*/ARCES spectra revealed only a single feature, Mg II  $\lambda 4481$  that could be reliably associated with the hot subdwarf. Nevertheless, I used the Doppler tomography to reconstruct the spectra as tool to search for other subdwarf lines in the echelle orders recording Mg II  $\lambda 4481$ , H $\beta$   $\lambda 4861$ , and H $\alpha$   $\lambda 6563$ . I adopted flux ratios using radii and model surface fluxes (for  $T_{\text{eff}}(\text{spectrum})$ ) based on the results in Table 5.4 ( $f_2/f_1 = 0.11, 0.10$ , and  $0.08$  for the three features, respectively). The reconstructed spectra show a low frequency variation in the continuum placement, and I relied upon forming ratios with the model spectra to rectify the reconstructed spectra for comparison purposes. The reconstructed optical spectra and corresponding models are shown in Figures 5.11 - 5.13, and I was gratified to see that this process revealed the presence of the H $\beta$  and H $\alpha$  lines of the subdwarf. The H $\alpha$  feature of the subdwarf shows a narrow core that is often observed in DA white dwarfs and results from non-LTE effects in the upper atmosphere (Koester &

Herrero 1988) that are not treated in the LTE models I used.

Table 5.5:  $T_{\text{eff}}$ (spectrum) Estimates from Spectral Models

Metallicity [ $M/H$ ]	$T_{\text{eff}}$ [short $\lambda$ ] (K)	$\chi^2_{\nu}$ [short $\lambda$ ]	$T_{\text{eff}}$ [long $\lambda$ ] (K)	$\chi^2_{\nu}$ [long $\lambda$ ]
WD				
+0.0	$13618 \pm 79$	1.78	$12533 \pm 119$	2.65
-0.5	$12376 \pm 88$	1.54	$11404 \pm 68$	2.60
-1.0	$10800 \pm 64$	1.75	$10112 \pm 46$	2.71
A-star				
+0.0	...	...	$8048 \pm 6$	2.91
-0.5	...	...	$7730 \pm 9$	2.27
-1.0	...	...	$7424 \pm 10$	1.95

## 5.7 Evolutionary State of EL CVn

Chen et al. (2017) investigated the formation of EL CVn-type binaries using the Modules for Experiments in Stellar Astrophysics (MESA). They assume that these systems are Population I low-mass binaries that have experienced non-conservative, stable mass transfer when the mass donor entered the red giant stage. They find that the most common pre-He WDs have mass within  $0.17 - 0.21 M_{\odot}$  and have companions in the mass range of  $1.3 - 1.5 M_{\odot}$ . The components of EL CVn have masses that fall within these ranges. Mass transfer during the red giant stage will depend on the radius of the envelope and thus on its core mass. Models predict that following envelope loss, there will be a close relationship between the mass of

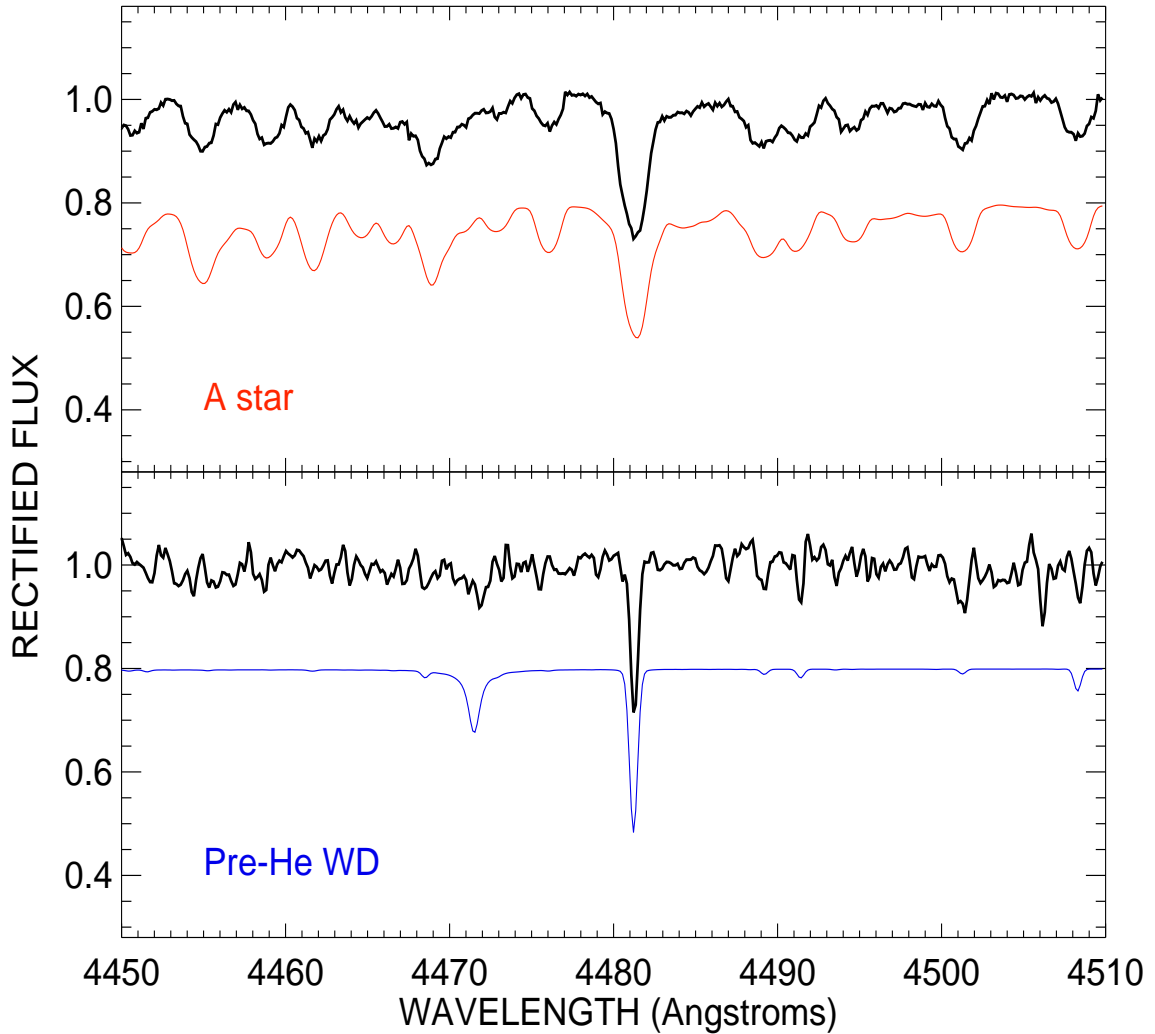


Figure 5.11: The reconstructed spectra of EL CVn in the vicinity of the Mg II  $\lambda 4481$  line (from *APO/ARCES* data). The spectra were rebinned to a lower resolution of  $R \sim 17000$ . The top panel shows the rectified flux of the reconstructed spectrum of the A-star in black and the model spectrum in red ( $[M/H] = 0.0$ ; offset by  $-0.2$ ). The bottom panel displays the reconstructed spectrum of the pre-He WD in black and the model spectrum in blue ( $[M/H] = -1.0$ ; offset by  $-0.2$ ). Note that the He I  $\lambda 4471$  line predicted in the model is absent from the reconstructed spectrum of the subdwarf.

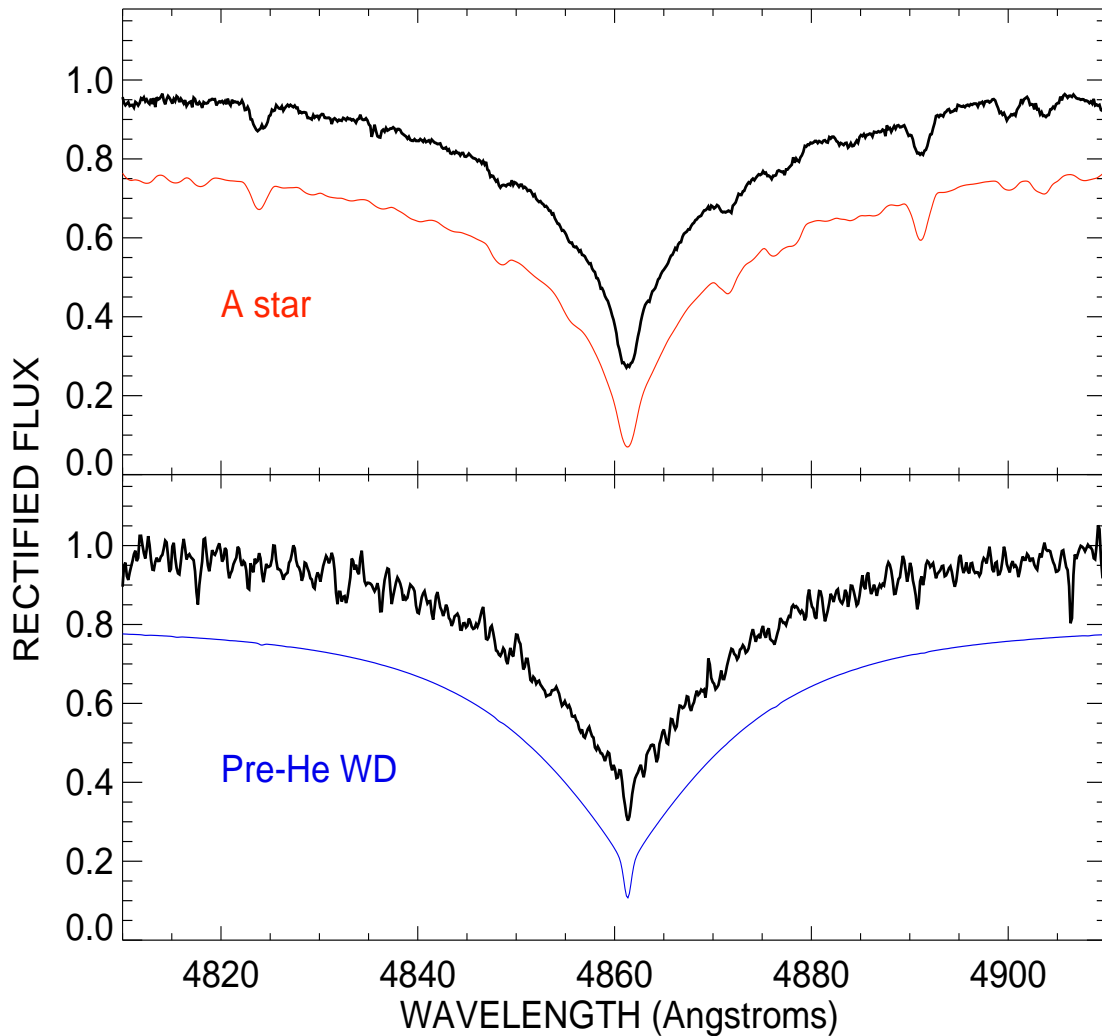


Figure 5.12: The reconstructed spectra of EL CVn in the vicinity of  $H\beta$  (from *APO/ARCES* data). The spectra were rebinned to a lower resolution of  $R \sim 17000$ . The top panel shows the rectified flux of the reconstructed spectrum of the A-star in black and the model spectrum in red ( $[M/H] = 0.0$ ; offset by  $-0.2$ ). The bottom panel displays the reconstructed spectrum of the pre-He WD in black and the model spectrum in blue ( $[M/H] = -1.0$ ; offset by  $-0.2$ ).

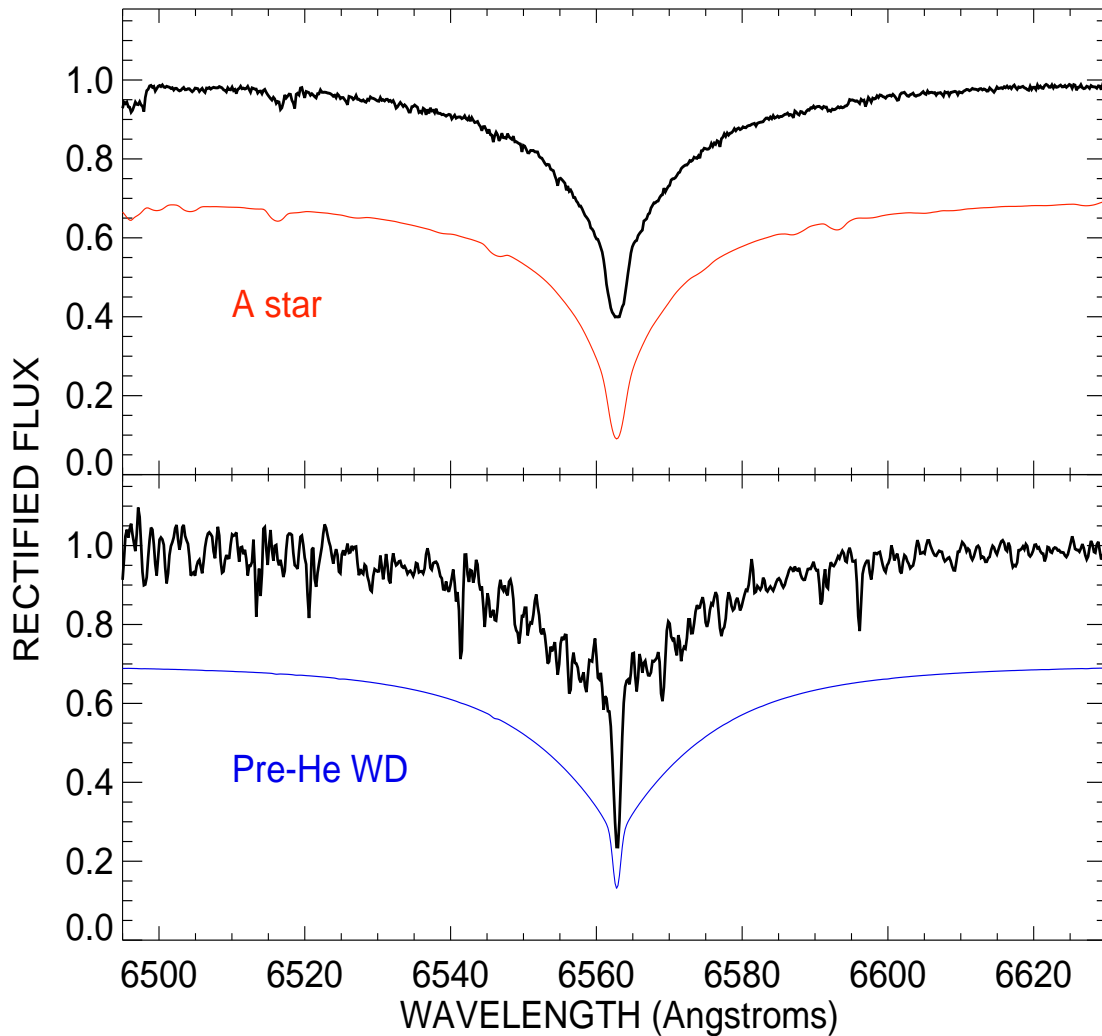


Figure 5.13: The reconstructed spectra of EL CVn in the vicinity of  $H\alpha$  (from *APO/ARCES* data). The spectra were rebinned to a lower resolution of  $R \sim 17000$ . The top panel shows the rectified flux of the reconstructed spectrum of the A-star in black and the model spectrum in red ( $[M/H] = 0.0$ ; offset by  $-0.3$ ). The bottom panel displays the reconstructed spectrum of the pre-He WD in black and the model spectrum in blue ( $[M/H] = -1.0$ ; offset by  $-0.3$ ).

the remnant core and the orbital period. The fact that the subdwarf mass and orbital period of EL CVn agree well with these predictions (e.g., Fig. 19 in Istrate et al. 2016 and Fig. 6 in van Roestel et al. 2018) offers indirect evidence that it formed through mass transfer during the red giant stage of the progenitor of the subdwarf.

Following the completion of mass transfer, the stripped cores may have a thick hydrogen envelope that can continue to power nuclear burning. Althaus et al. (2013) used the stellar evolutionary code LPCODE to generate evolutionary tracks of extremely low mass WDs with He cores in the mass range of  $0.15 - 0.45 M_{\odot}$ , and they used their results to estimate cooling ages. They show that the stars may experience intermittent H-burning as CNO shell flashes that will change their evolutionary trajectory in the  $(T_{\text{eff}}, g)$  plane. van Roestel et al. (2018) applied the evolutionary sequences to 36 newly discovered EL CVn-type binaries discovered through the Palomar Transient Factory, and the observationally determined masses and temperatures of these systems are in broad agreement with the models. Similar evolutionary sequences of extremely low mass WDs were investigated by Calcaferro et al. (2018), and they focused on remnants with thinner H-envelopes. They find that a thinner envelope yields remnants with higher gravities and shorter cooling times. The derived gravity of the subdwarf in EL CVn is much lower than found from their calculations, so instead the pre-He WD in EL CVn probably has a thick H-envelope as suggested by Maxted et al. (2014).

In Figure 5.14, I show the evolutionary sequences from Althaus et al. (2013) in the  $(T_{\text{eff}}, R)$  plane for several assumed masses. I also plot these parameters for the subdwarf in EL CVn. I see that the observed temperature and radius would fall on a mass track for an object of

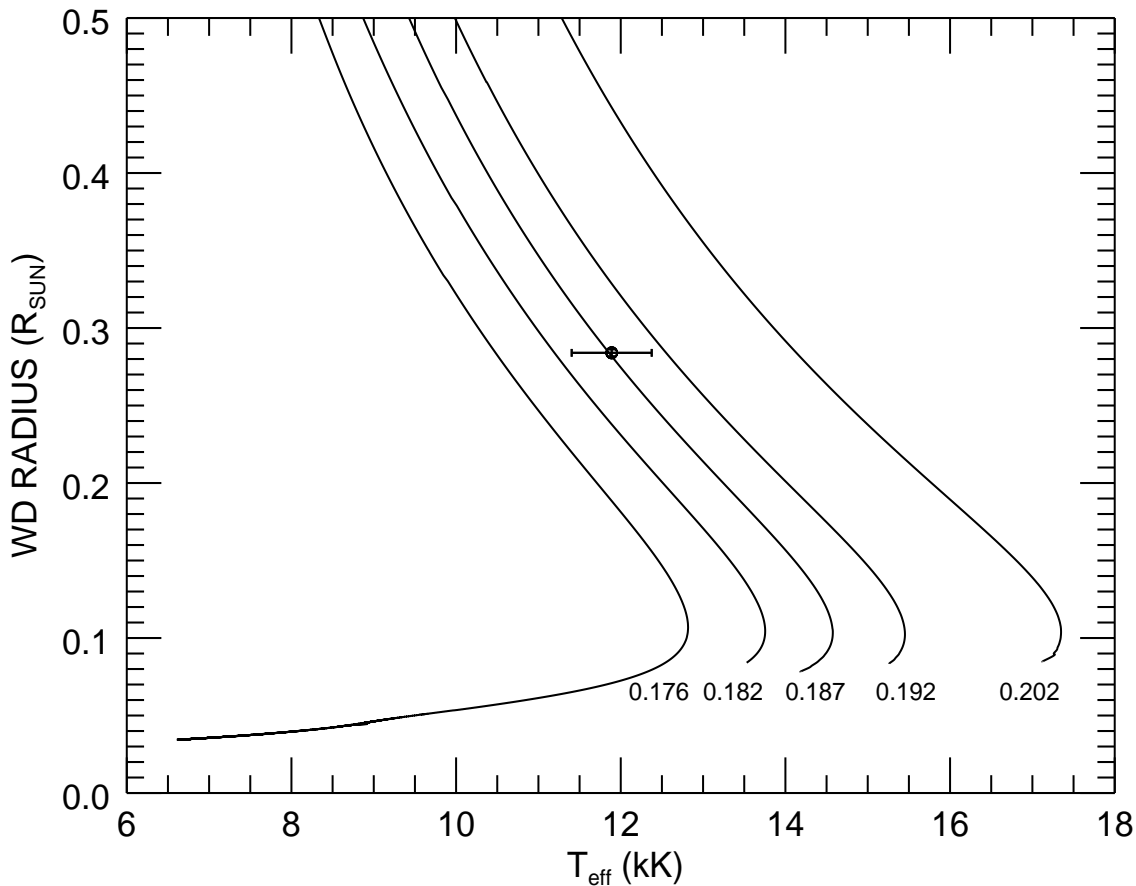


Figure 5.14: Evolutionary tracks from Althaus et al. (2013) in the  $(T_{\text{eff}}, R)$  plane for several assumed masses (labeled in units of  $M_{\odot}$ ). I plot the measured  $T_{\text{eff}}$  and  $R$  of the pre-He WD component (Sections 5.5, 5.6) as an open circle with the associated uncertainties.

0.187  $M_{\odot}$  or about 6% ( $3\sigma$ ) more massive than I find. This suggests that the subdwarf is somewhat overluminous for its mass in the context of these evolutionary tracks. I also used Table 5.3 from Althaus et al. (2013) to estimate the cooling age, i.e., the time elapsed since the end of Roche-lobe overflow, from the observed temperature and gravity. These models suggest that the cooling age is about 155 Myr.

The relatively long time span since the conclusion of Roche lobe overflow means that the subdwarf has had sufficient time for elemental diffusion processes to occur. I found that the metal lines of the subdwarf indicated a sub-solar metallicity that could be the result of such processes. Furthermore, an inspection of the *HST*/COS reconstructed spectrum of the subdwarf indicates a number of differences from the predictions of the UVBLUE model for a metallicity of  $[M/H] = -0.5$ . I see that several lines are much stronger than predicted (Si II  $\lambda\lambda 1526.7, 1533.4$ ; Al II  $\lambda 1670.8$ ), while others are weaker or absent (P II  $\lambda\lambda 1542.9, 1535.9, 1536.4, 1542.3, 1543.1, 1543.6$ ; C I  $\lambda\lambda 1459.0, 1463.3, 1467.4, 1470.1, 1481.8, 1656.3, 1657.0, 1657.9$ ). In the optical spectrum only Mg II  $\lambda 4481$  is readily visible, and I found that it is also weaker than expected for solar metallicity. The best match from the BLUERED grid was made with  $[M/H] = -1.0$  (Fig. 5.11). Note that for our derived subdwarf temperature, the model predicts that He I  $\lambda 4471$  should be present in the spectrum, but in the reconstructed spectrum it appears to be absent (Fig. 5.11). This suggests that the atmosphere is depleted in He. These differences are probably related to elemental diffusion processes in the subdwarf atmosphere that will cause hydrogen to rise and heavier elements to sink. Istrate et al. (2016) discuss how the outcome of these processes will depend on the competition between gravitational settling and rotational mixing. These clues from spectroscopy suggest that the atmosphere of EL CVn is enriched in hydrogen and depleted in most heavier elements.

## CHAPTER 6

### CONCLUSIONS AND FUTURE WORK

#### 6.1 Implications of the candidate Be+sdO systems and follow-up observations

##### *6.1.1 Future FUV spectroscopy of Be+sdO candidate systems using the HST/STIS*

A rapidly rotating Be star is conspicuous by its high rotational velocity and unique, decretion circumstellar disk. The origin of its fast spinning is still debated. Many studies indicate growing evidence that favors the hypothesis of a post-mass-transfer scenario in a close binary system, in which the former massive star evolved away from the main-sequence and lost its outer envelope. The final fate of the stripped star is dominated by its mass: it may either explode to form a BeXRB if the remnant mass is above the Chandrasekhar mass limit ( $1.4 M_{\odot}$ ) or shrink down to the extreme horizontal branch (EHB) to become a white dwarf or subdwarf star.

There were only three Be+sdO binary systems known at the start of my work, and all were detected through *IUE* spectroscopy ( $\phi$  Per, FY CMa, and 59 Cyg). Inspired by these positive detections, I expanded the search to identify additional hot subdwarf stars. Based on spectroscopic analyses using archival spectra from *IUE*, now the number of such Be+sdO binaries has increased to 16 out of a sample of 264 stars, which yields a 6% detection rate. It is important to constrain the population of the Be+sdO binary systems and investigate their fundamental physical parameters in order to trace the evolutionary history of the binary.

These few discoveries of stripped-down cores in binaries probably represent the “tip of the

iceberg” of a much larger population (Di Stefano 2011), but we need more examples to estimate reliably their actual numbers. A recent study by Schootemeijer et al. (2018) concludes that the few detections thus far represent only the brightest cases that might be found. They constructed evolutionary tracks for the stripped-down mass donor stars to compare with the properties of the subdwarf in  $\phi$  Per and those in other Be+sdO systems. Their models indicate that the subdwarfs spend most of their remaining lifetime as faint, He-core burning stars. It is only in the last 2% of its lifetime as a subdwarf that the star brightens as nuclear burning begins in a He-shell phase, and the subdwarf appears to have a luminosity that corresponds to this brighter stage of evolution. If correct, then there should be about 50 Be+sdO (faint) systems for every 1 Be+sdO (bright) system observed. Thus, it is crucial to conduct a census of Be binaries to find if their numbers are sufficient to explain the rapid rotation of Be stars in general as the result of binary mass exchange.

The key to understanding the missing link in the evolution of massive binaries is to determine if all the known Be+sdO binaries are indeed in the bright stage of He-shell burning. Then it would be possible to estimate the total number of faint and bright companion cases from their associated timescales in evolutionary models. Furthermore, the characteristics of Be+sdO systems will help our understanding of the extent of envelope removal by mass transfer, the mass transfer efficiency, wind mass loss of the stripped stars, and the physical properties of stellar cores. However, until recently it was not feasible to launch such an investigation because there were too few known Be+sdO binaries and most Be stars probably have companions that are too faint to detect even with sensitive FUV spectroscopy from

*HST*. The situation now has changed, and there is now a much larger sample of 13 candidate systems (12 systems from Chapter 4, and HD 55606 identified to be Be+sdO binary through optical and *H*-band spectroscopy from Chojnowski et al. 2018) with a detected companion bright enough for measurement with *HST*. This new sample gives us the opportunity to triple the number of Be+sdO systems with stellar parameters that can be measured from their FUV spectra. I plan to obtain the first high S/N, FUV spectra of these systems with *HST*/STIS and to extract the subdwarf spectra in the short wavelength regime where they appear brightest. Three visits per target will be needed to measure the Doppler shifts of both the Be and sdO stars, to determine the mass ratio, and also to derive orbital parameters. Analysis of the extracted subdwarf star spectrum will yield its effective temperature and monochromatic flux ratio relative to the Be star. Then through a reassessment of the Be star's temperature and radius (from existing data on the spectral energy distribution and *Gaia* parallax), the radius and luminosity of the sdO will be determined, so that its properties can be compared to model evolutionary tracks in the HRD.

This approved and scheduled *HST*/STIS program to characterize the hot companions orbiting Be stars will be used to determine the fundamental parameters of stars that have been stripped of their envelopes to reveal their hot cores. The results will establish the luminosity distribution of the subdwarfs and will demonstrate whether all the known Be+sdO systems occupy the short-lived, He-shell burning stage of evolution. Using the evolutionary timescales from models, the work will enable reliable estimates of the numbers of fainter Be+sdO systems where the hot remnant remains undetected. The new sample will triple the number

of known Be+sdO systems with known parameters, and it will complete the picture of how binary interactions lead to Be+sdO stars, Be+WD (Li et al. 2012), Be+NS (Reig 2011), and Be+BH binaries (Casares et al. 2014). The future work using the *HST*/STIS to characterize the Be+sdO candidate systems is important for studies of massive star evolution, because a large fraction of massive stars have nearby stellar companions (Sana et al. 2012) and binary interactions play a key role in their destinies (de Mink et al. 2014).

### ***6.1.2 Future optical spectroscopy of candidate Be+sdO systems using the SMARTS/CHIRON and APO/ARCES***

The FUV spectroscopy from the *HST*/STIS will be valuable to reveal the fundamental physical parameters and properties of the Be+sdO binary systems. However, time-domain optical spectroscopy is needed to characterize the orbital parameters of these binaries and complements to the FUV spectral analysis as well. In this new sample of 13 Be+sdO candidates systems, active observing programs have begun for targets that are visible in the northern sky using the *APO*/ARCES. In addition, I have proposed spectroscopic observations using the CHIRON spectrometer (Tokovinin et al. 2013) on the 1.5 m *SMARTS* telescope at CTIO to collect optical spectra of the remaining targets in the sample visible in the southern hemisphere. The target names, coordinates,  $V$  magnitudes, exposure times, and number of planned exposures for each star are listed in Table 6.1. The Be stars probably have orbital periods between 40 and 200 days. In order to compute accurate orbital periods of these Be+sdO candidate systems, I thus need a large set of observations over six months to have sufficient temporal and orbital phase coverage. I will compute the primary Be star radial

velocities from CCFs in two ways. First, I will construct model spectra from BLUERED for use as a template to compute the CCFs with the observed absorption line features, and then radial velocities will be determined from the CCF bisector as discussed in Chapter 2. Second, I will use the same bisector technique to compute the RVs of the Balmer emission lines. Once I obtain the RV measurements of the Be component, I will apply the periodogram technique to estimate the orbital period of the star. I then will use the method from Morbey & Brosterhus (1974) to determine the spectroscopic orbital elements from the measured RVs. Maintz et al. (2005) argued that the absorption line feature at He II  $\lambda 4686 \text{ \AA}$  is associated with the hot sdO companion in the 59 Cyg system. A similar feature was confirmed by Chojnowski et al. (2018) for the Be+sdO system HD 55606 as well. I thus will compute the RVs of the sdOs using this line profile if present. From spectral model fitting, I will estimate the temperature of the Be stars, derive their physical size from their spectral energy distribution and distance from *Gaia*, and also estimate their projected rotational broadening  $V \sin i$ . Furthermore, by combining the *APO/ARCES* and *SMARTS/CHIRON* observations with the *IUE* measurements (Chapter 4), as well as the pending *HST/STIS* FUV observations, I will be able to determine the orbital elements and to apply the iterative Doppler tomography algorithm (Chapter 3) to extract the individual spectra of both components of these Be+sdO binary systems. I thus will be able to determine the temperatures,  $\log g$ , and sizes of both components from model fitting.

Table 6.1: Target Table of 5 Be+sdO Candidate Systems For *SMARTS/CHIRON*

HD Number	Right Ascension (hh:mm:sec)	Declination (deg:mm:sec)	Spectral Type	$V$ (mag)	Exposure Time (sec)	Number of Observations
113120	13 03 05.3	-71 28 32.6	B2 IVne	6.03	340	35
137387	15 31 30.8	-73 23 22.5	B2 Vnpe	5.49	210	33
152478	16 56 08.8	-50 40 29.2	B3 Vnpe	6.33	450	32
157042	17 23 16.0	-47 28 05.5	B2.5 IVe	5.25	170	30
157832	17 27 54.8	-47 01 34.4	B1.5 Ve	6.66	600	30

### 6.1.3 Shell line variations in other Be+sdO systems

In Chapter 2, I reported the absorption shell line features shown in both the *IUE* and  $H\alpha$  spectra of HR 2142. By adopting a circumbinary disk model, these shell line variations are suggested to be associated with moving gas crossing the gap in the disk, which is created by the subdwarf companion. Due to the gravitational attraction of the subdwarf, a tidal wake is created and gas heated by the wake strikes the outer boundaries of the Be disk to form density enhancements. At orbital phases when these structures are seen projected against the Be star, we observe the shell line variations. In addition to direct heating by the subdwarf, tidal wake induced heating results in the presence of the emission line profile of He I  $\lambda 6678$  in several known Be+sdO systems; for example,  $\phi$  Per (Štefl et al. 2000), FY CMa (Peters et al. 2008), and 59 Cyg (Peters et al. 2013). However, HR 2142 has a very weak variation of this emission profile, mainly due to the low flux contribution from the

subdwarf companion. It will be helpful to inspect the line variability of this optical profile in the spectral of 60 Cyg and those Be+sdO candidate systems reported in Chapter 4, for which the subdwarf companions were detected in FUV solely.

Gies et al. (1998) reported that  $\phi$  Per shows similar shell line features at  $\phi = 0.958$  among lines near the 1647 region. These shell spectrum features are primarily lines of Fe IV. Peters et al. (2016) argued that the small number of such cases displaying phase-variable shell lines is mainly limited by three factors. First, the Be disk is massive enough to have a significant density towards the outer region of the disk. Then the action of the tidal wake created by the subdwarf companion will be sufficient to build up a large density enhancement that leads to the formation of the shell line features. Second, HR 2142 has an orbital inclination of about  $85^\circ$  and  $\phi$  Per has an estimation of  $i > 77^\circ$ , thus the Be+sdO systems need to have a high inclination (near  $i \sim 90^\circ$ ) so that the tidal density enhancements will cross the line of sight to the observer. Last, the subdwarf has moderate mass that creates a gap of size that allows the gas to move across the gap and to strike the outer edge of the Be disk. Otherwise, the gap is either too small (in the case of a low mass subdwarf) or too wide (in the case of a high mass subdwarf) to produce the shell line features from gap-crossing gas. Nevertheless, it will be useful to search for similar shell line variations among the Be+sdO candidate systems. Any new examples of shell line variability will help us to constrain the circumstellar disk models and to estimate the size and geometry of these circumbinary systems.

#### *6.1.4 Resolving the problem of missing late-type Be stars in Be+sdO candidate systems*

In Chapter 4, I reported the work to search for additional Be+sdO binary systems using archival FUV spectra from *IUE*. This led to the detection of another 12 Be+sdO candidate systems. The total number of Be+sdO binary system has increased to 17 in a sample of 264 stars, which corresponds to a detection rate of 6%. A histogram of the spectral type distribution of the full sample (including both the null detections in the dotted line and positive detections in the filled line) is shown in Figure 4.4, and the distribution suggests that all known and newly detected Be+sdO systems have spectral types among B0–B3. No Be+sdO candidate systems were detected among late-type Be stars. Pols et al. (1991) argue that if Be+sdO binary systems have a flat initial mass ratio distribution, then the number of Be+sdO systems may peak in the B0–B5 range; otherwise, the spectral distribution for these binary system will skew towards the late-type Be stars. In Table 6.2, I have summarized the spectral type, individual mass, orbital period, secondary radius, and references of the five known Be+sdO binary systems. The sample is too small to show if there is a trend of decreasing subdwarf mass towards the late-type stars as suggested by stellar evolution or if there is a relationship between the orbital period and mass of the subdwarf.

Table 6.2: Physical properties of known Be+sdO binary systems

HD Number	Star Name	Spectral Classification	$M_1$ ( $M_\odot$ )	$M_2$ ( $M_\odot$ )	$P$ (day)	$R_2$ ( $R_\odot$ )	$T_{\text{eff}}$ (K)	Spectral classification Reference	Primary mass Reference
10516	$\phi$ Per	B1.5 V:e-shell	9.3	1.1	126.673	1.3	$53 \pm 3$	Slettebak (1982)	Gies et al. (1998)
41335	HR 2142	B1.5 IV-Vnne	10.5	0.76	$80.913 \pm 0.018$	0.13	$43 \pm 5$	Peters (2001)	Peters (2001)
58978	FY CMa	B0.5 IVe	13.2	1.3	$37.257 \pm 0.003$	0.6	$45 \pm 5$	Slettebak (1982)	Harmanec (1988)
200120	59 Cyg	B1 Ve	6.3-9.4	0.62-0.91	$28.187 \pm 0.001$	0.34-0.43	$52 \pm 5$	Slettebak (1982)	Peters et al. (2013)
200310	60 Cyg	B1 Ve	11.8	1.7	$146.6 \pm 0.6$	0.48	$42 \pm 4$	Koubský et al. (2000)	Koubský et al. (2000)

It is important to point that in this dissertation work to search for Be+sdO binary systems, I adopted a template spectrum for a hot subdwarf with effective temperature of 45 kK. This assumption is based on the estimated temperatures of the subdwarfs in the three known Be+sdO systems (Table 6.2). However, it is possible that some of the subdwarfs may not be as hot as previously suggested. Thus, it will be helpful to adopt a cooler template spectrum for the subdwarfs to search for their spectral features in the late-type Be stars.

## 6.2 Implications of the EL CVn binary system

EL CVn is the prototype of post-mass transfer binaries in which the stripped mass donor star has not yet contracted to WD dimensions, and, given a favorable orientation, they can be detected as eclipsing binaries with extremely fast ingress and egress durations. Determining the physical properties of the hot remnant star requires spectroscopic analysis in the ultraviolet part of the spectrum where their flux dominates. This *HST*/COS study of EL CVn demonstrates the scientific rewards of high resolution spectroscopy in the wavelength domain where the spectrum of the hot remnant shines clearly.

The first task was to identify the spectral lines of the hot subdwarf and to use their orbital Doppler shifts to find the mass ratio (Chapter 5). The *HST*/COS spectra revealed a host of the subdwarf metallic lines in the FUV, and the *APO*/ARCES spectra showed the presence of the Mg II  $\lambda 4481$  line associated with the subdwarf. By combining radial velocity measurements for both components with a reconsideration of the eclipsing light curve, I find that the masses of the components are  $1.46 \pm 0.05$  and  $0.176 \pm 0.004 M_{\odot}$  for the A-star and

subdwarf, respectively. From the eclipse duration data I estimate the corresponding radii of  $1.46 \pm 0.05$  and  $0.284 \pm 0.003 R_{\odot}$ , respectively.

I applied several methods to estimate the effective temperatures of both stars. The absolute flux of the stars depends on their temperatures, angular sizes, and interstellar extinction, and by setting the angular size from the physical radii and distance from GAIA DR2, I was able to infer the temperatures of both components. I obtained another temperature estimate by comparing the line patterns of the subdwarf and the flux distribution of the A-star in *HST*/COS spectra with model spectra. The two results agree within errors and with the temperature ratio derived by fitting the eclipse depths:  $T_{\text{eff}} = 8100 \pm 100$  K and  $11800 \pm 400$  K for the A-star and subdwarf, respectively. I caution, however, that these results rely on model atmospheres for standard abundance distributions that may not be appropriate for the subdwarf star.

The mass gainer star has a mass and radius like that of an F-type star, but has a temperature associated with a mid-A-type star. The fact that it is overluminous for its mass may be a consequence of mixing of new nuclear fuel from mass accretion during the mass transfer stage. Mass transfer may have also led to a spin-up of the star, but surprisingly the A-star appears to be rotating slower than synchronously.

The properties of the hot pre-He WD star agree in many ways with the predictions of model evolutionary sequences. The star's mass and orbital period place it precisely in the  $(M, P)$  relation expected for stars that were stripped of their envelopes during the red giant stage. However, the star is slightly hotter than expected for its mass and radius relative to the

evolutionary tracks from Althaus et al. (2013). The metallic line spectrum in the FUV is suggestive of a subsolar metallicity that is unexpected given the relative youth implied by the total system mass and its thin disk kinematics (Maxted et al. 2014). I suggest that the low metal abundances are rather the result of elemental diffusion processes in the outer envelope that play a major role in setting the chemistry of WD atmospheres (Koester & Chanmugam 1990). Diffusion will cause H to float upwards and heavier elements to sink, and indeed the optical spectra show that the H-Balmer lines are strong while He lines are weak or absent. Furthermore, I find that not all the heavier elements are reduced in similar proportions. For example, the ultraviolet spectra indicate that the C and P lines are very weak while the Si and Al lines are relatively stronger. The chemistry of the atmosphere of the hot pre-He WD star offers a key insight into the processes that lead eventually to the striking abundance differences among the white dwarf stars.

### **6.3 Concluding remarks**

A large fraction of massive stars have close stellar companions, and these pairs are bound to interact in profound ways over their lifetime. In the first stage, the initially more massive star will lose its envelope by Roche lobe overflow, and it will be left as a hot, low mass helium core. In this work, I have shown how a spectroscopic search can find the hot subdwarf companions of massive, early-type, binary systems. Determining the physical parameters of such binary systems will constrain their location in the HRD and will help trace their evolutionary history. These hot subdwarfs may have lost their hydrogen envelope entirely

through binary interaction, and they emerge as a helium star. Massive helium remnant stars may explode as hydrogen deficient supernovae (SN Ib and SN Ic; Eldridge et al. 2013). These helium subdwarf stars are also the potential progenitors of neutron stars, and neutron star pairs can merge over long time scales to create bright gravitational wave sources, such as GW170817 (Abbott et al. 2017; Tauris et al. 2017). The hot subdwarf companions may contribute significantly to the UV flux of stellar populations (Han et al. 2010; Götberg et al. 2018), and may represent a missing component in spectral synthesis models (Bruzual & Charlot 2003). My spectroscopic investigations have helped to open the window on this evolved stellar population that was hidden from view in the glare of their companions.

## REFERENCES

- Abbott, B. P. et al. 2017, *ApJ*, 850, L40
- Abt, H. A., Levato, H., & Grosso, M. 2002, *ApJ*, 573, 359
- Abt, H. A., & Levy, S. G. 1978, *ApJS*, 36, 241
- Althaus, L. G., Miller Bertolami, M. M., & Córscico, A. H. 2013, *A&A*, 557, A19
- Baade, D. et al. 2016a, *A&A*, 588, A56
- . 2016b, *A&A*, 588, A56
- Bagnuolo, Jr., W. G., Gies, D. R., Hahula, M. E., Wiemker, R., & Wiggs, M. S. 1994, *ApJ*, 423, 446
- Bailer-Jones, C. A. L., Rybizki, J., Fouesneau, M., Mantelet, G., & Andrae, R. 2018, *AJ*, 156, 58
- Bate, M. R., Lubow, S. H., Ogilvie, G. I., & Miller, K. A. 2003, *MNRAS*, 341, 213
- Bertone, E., Buzzoni, A., Chávez, M., & Rodríguez-Merino, L. H. 2008, *A&A*, 485, 823
- Bjorkman, K. S., Miroshnichenko, A. S., McDavid, D., & Pogrosheva, T. M. 2002, *ApJ*, 573, 812
- Bloemen, S. et al. 2012, *MNRAS*, 422, 2600
- Boubert, D., & Evans, N. W. 2018, *MNRAS*, 477, 5261
- Bragança, G. A., Daflon, S., Cunha, K., Bensby, T., Oey, M. S., & Walth, G. 2012, *AJ*, 144, 130
- Breton, R. P., Rappaport, S. A., van Kerkwijk, M. H., & Carter, J. A. 2012, *ApJ*, 748, 115

- Bruzual, G., & Charlot, S. 2003, MNRAS, 344, 1000
- Calcaferro, L. M., Althaus, L. G., & Córscico, A. H. 2018, A&A, 614, A49
- Campbell, W. W. 1895, ApJ, 2
- Carciofi, A. C. 2011, in IAU Symposium, Vol. 272, Active OB Stars: Structure, Evolution, Mass Loss, and Critical Limits, ed. C. Neiner, G. Wade, G. Meynet, & G. Peters, 325–336
- Carter, J. A., Rappaport, S., & Fabrycky, D. 2011, ApJ, 728, 139
- Casares, J., Negueruela, I., Ribó, M., Ribas, I., Paredes, J. M., Herrero, A., & Simón-Díaz, S. 2014, Nature, 505, 378
- Chen, X., Maxted, P. F. L., Li, J., & Han, Z. 2017, MNRAS, 467, 1874
- Chini, R., Hoffmeister, V. H., Nasserri, A., Stahl, O., & Zinnecker, H. 2012, MNRAS, 424, 1925
- Chojnowski, S. D. et al. 2018, ApJ, 865, 76
- . 2017, AJ, 153, 174
- Coe, M. J. et al. 2010, MNRAS, 406, 2533
- Cramer, N., Doazan, V., Nicolet, B., de La Fuente, A., & Barylak, M. 1995, A&A, 301, 811
- Danforth, C. W., Keeney, B. A., Stocke, J. T., Shull, J. M., & Yao, Y. 2010, ApJ, 720, 976
- de Bruijne, J. H. J., & Eilers, A.-C. 2012, A&A, 546, A61
- De Mey, K., Aerts, C., Waelkens, C., & Van Winckel, H. 1996, A&A, 310, 164
- de Mink, S. E., Sana, H., Langer, N., Izzard, R. G., & Schneider, F. R. N. 2014, ApJ, 782, 7
- Delplace, A. M. 1971, A&A, 10, 246
- Dermott, S. F., & Murray, C. D. 1981, Icarus, 48, 1

- Dhillon, V. S. et al. 2007, MNRAS, 378, 825
- Di Stefano, R. 2011, AJ, 141, 142
- Doazan, V., Bourdonneau, B., & Thomas, R. N. 1988, A&A, 205, L11
- Doazan, V., de La Fuente, A., Barylak, M., Cramer, N., & Mauron, N. 1993, A&A, 269, 415
- Dulaney, N. A. et al. 2017, ApJ, 836, 112
- Eggleton, P. P. 1983, ApJ, 268, 368
- Eldridge, J. J., Fraser, M., Smartt, S. J., Maund, J. R., & Crockett, R. M. 2013, MNRAS, 436, 774
- Faigler, S., Kull, I., Mazeh, T., Kiefer, F., Latham, D. W., & Bloemen, S. 2015, ApJ, 815, 26
- Fischer, W. J. 2019, Cosmic Origins Spectrograph Instrument Handbook, Version 11.0, 11th edn. (Baltimore: STScI)
- Fitzpatrick, E. L. 1999, PASP, 111, 63
- Frémat, Y., Zorec, J., Hubert, A.-M., & Floquet, M. 2005, A&A, 440, 305
- Gaia Collaboration. 2016, VizieR Online Data Catalog, 1337
- Gies, D. R., Bagnuolo, Jr., W. G., Ferrara, E. C., Kaye, A. B., Thaller, M. L., Penny, L. R., & Peters, G. J. 1998, ApJ, 493, 440
- Gies, D. R. et al. 2008, ApJ, 682, L117
- Giménez-García, A., Torrejón, J. M., Eikmann, W., Martínez-Núñez, S., Oskinova, L. M., Rodes-Roca, J. J., & Bernabéu, G. 2015, A&A, 576, A108
- Gontcharov, G. A., & Mosenkov, A. V. 2018, MNRAS, 475, 1121

- Götberg, Y., de Mink, S. E., Groh, J. H., Kupfer, T., Crowther, P. A., Zapartas, E., & Renzo, M. 2018, *A&A*, 615, A78
- Green, J. C. et al. 2012, *ApJ*, 744, 60
- Grundstrom, E. D., & Gies, D. R. 2006, *ApJ*, 651, L53
- Guo, Z., Gies, D. R., Matson, R. A., García Hernández, A., Han, Z., & Chen, X. 2017, *ApJ*, 837, 114
- Haberl, F. et al. 2012, *A&A*, 545, A128
- Hamaguchi, K., Oskinova, L., Russell, C. M. P., Petre, R., Enoto, T., Morihana, K., & Ishida, M. 2016, *ApJ*, 832, 140
- Han, Z., Podsiadlowski, P., & Lynas-Gray, A. 2010, *Ap&SS*, 329, 41
- Hardy, L. K., Butterley, T., Dhillon, V. S., Littlefair, S. P., & Wilson, R. W. 2015, *MNRAS*, 454, 4316
- Harmanec, P. 1988, *Bulletin of the Astronomical Institutes of Czechoslovakia*, 39, 329
- Hartkopf, W. I., Mason, B. D., McAlister, H. A., Turner, N. H., Barry, D. J., Franz, O. G., & Prieto, C. M. 1996, *AJ*, 111, 936
- Hoffleit, D., & Jaschek, C. 1991, *The Bright Star Catalogue* (5th ed.; New Haven, CT: Yale University Observatory)
- Hoogerwerf, R., de Bruijne, J. H. J., & de Zeeuw, P. T. 2001, *A&A*, 365, 49
- Houk, N. 1978, *Michigan Catalogue of Two-dimensional Spectral Types for the HD stars. Declinations  $-52$  to  $-41$ , Vol. 2* (Ann Arbor, MI: University of Michigan)
- . 1982, *Michigan Catalogue of Two-dimensional Spectral Types for the HD stars. Declinations  $-41$  to  $-30$ , Vol. 1* (Ann Arbor, MI: University of Michigan)

- nations  $-40$  to  $-26$ , Vol. 3 (Ann Arbor, MI: University of Michigan)
- Houk, N., & Cowley, A. P. 1975, Michigan Catalogue of Two-dimensional Spectral Types for the HD stars. Declinations  $-90$  to  $-53$ , Vol. 1 (Ann Arbor, MI: University of Michigan)
- Houk, N., & Swift, C. 1999, Michigan Catalogue of Two-dimensional Spectral Types for the HD stars. Declinations  $-12$  to  $5$ , Vol. 5 (Ann Arbor, MI: University of Michigan)
- Huang, W., & Gies, D. R. 2006, ApJ, 648, 580
- Huang, W., Gies, D. R., & McSwain, M. V. 2010, ApJ, 722, 605
- Hynek, J. A., & Struve, O. 1942, ApJ, 96, 425
- Istrate, A. G., Marchant, P., Tauris, T. M., Langer, N., Stancliffe, R. J., & Grassitelli, L. 2016, A&A, 595, A35
- Klement, R. et al. 2019, in preparation, ApJ
- Koester, D., & Chanmugam, G. 1990, Reports on Progress in Physics, 53, 837
- Koester, D., & Herrero, A. 1988, ApJ, 332, 910
- Kolbas, V. et al. 2015, MNRAS, 451, 4150
- Koubský, P. et al. 2000, A&A, 356, 913
- Koubský, P., Kotková, L., Votruba, V., Šlechta, M., & Dvořáková, Š. 2012, A&A, 545, A121
- Lanz, T., & Hubeny, I. 2003, ApJS, 146, 417
- Lee, U., Osaki, Y., & Saio, H. 1991, MNRAS, 250, 432
- Lesh, J. R. 1968, ApJS, 17, 371
- Levenhagen, R. S., & Leister, N. V. 2006, MNRAS, 371, 252
- Li, K. L. et al. 2012, ApJ, 761, 99

- Lindroos, K. P. 1985, *A&AS*, 60, 183
- Lopes de Oliveira, R., & Motch, C. 2011, *ApJ*, 731, L6
- Lurie, J. C. et al. 2017, *AJ*, 154, 250
- Maintz, M., Rivinius, T., Stahl, O., Stefl, S., & Appenzeller, I. 2005, *Publications of the Astronomical Institute of the Czechoslovak Academy of Sciences*, 93, 21
- Mason, B. D., Hartkopf, W. I., Wycoff, G. L., & Wieder, G. 2007, *AJ*, 134, 1671
- Mason, B. D., ten Brummelaar, T., Gies, D. R., Hartkopf, W. I., & Thaller, M. L. 1997, *AJ*, 114, 2112
- Mason, B. D., Wycoff, G. L., Hartkopf, W. I., Douglass, G. G., & Worley, C. E. 2001, *AJ*, 122, 3466
- Matson, R. A., Gies, D. R., Guo, Z., & Orosz, J. A. 2016, *AJ*, 151, 139
- Matson, R. A., Gies, D. R., Guo, Z., Quinn, S. N., Buchhave, L. A., Latham, D. W., Howell, S. B., & Rowe, J. F. 2015, *ApJ*, 806, 155
- Maxted, P. F. L. et al. 2011, *MNRAS*, 418, 1156
- . 2014, *MNRAS*, 437, 1681
- Mayer, A., Deschamps, R., & Jorissen, A. 2016, *A&A*, 587, A30
- McAlister, H. A. 1976, *PASP*, 88, 957
- Mennickent, R. E., Sterken, C., & Vogt, N. 1998, *A&A*, 330, 631
- Meynet, G., Georgy, C., Revaz, Y., Walder, R., Ekström, S., & Maeder, A. 2010, in *Revista Mexicana de Astronomía y Astrofísica*, vol. 27, Vol. 38, *Revista Mexicana de Astronomía y Astrofísica Conference Series*, 113–116

- Meynet, G., & Maeder, A. 2002, *A&A*, 390, 561
- Morbey, C. L., & Brosterhus, E. B. 1974, *PASP*, 86, 455
- Mourard, D. et al. 2015, *A&A*, 577, A51
- Neiner, C., de Batz, B., Cochard, F., Floquet, M., Mekkas, A., & Desnoux, V. 2011, *AJ*, 142, 149
- Nemravová, J. et al. 2012, *A&A*, 537, A59
- . 2010, *A&A*, 516, A80
- Nichols, J. S., & Linsky, J. L. 1996, *AJ*, 111, 517
- Ogilvie, G. I., & Lubow, S. H. 2002, *MNRAS*, 330, 950
- Okazaki, A. T., Bate, M. R., Ogilvie, G. I., & Pringle, J. E. 2002, *MNRAS*, 337, 967
- Orosz, J. A., & Hauschildt, P. H. 2000, *A&A*, 364, 265
- Otero, S. A., & Dubovsky, P. A. 2004, *Information Bulletin on Variable Stars*, 5557, 1
- Panoglou, D., Carciofi, A. C., Vieira, R. G., Cyr, I. H., Jones, C. E., Okazaki, A. T., & Rivinius, T. 2016, *MNRAS*, 461, 2616
- Parthasarathy, M., & Lambert, D. L. 1987, *Journal of Astrophysics and Astronomy*, 8, 51
- Peters, G. J. 1971, *ApJ*, 163, L107
- . 1972, *PASP*, 84, 334
- . 1983, *PASP*, 95, 311
- . 2001, *Publications of the Astronomical Institute of the Czechoslovak Academy of Sciences*, 89, 30
- Peters, G. J., Gies, D. R., Grundstrom, E. D., & McSwain, M. V. 2008, *ApJ*, 686, 1280

- Peters, G. J., Pewett, T. D., Gies, D. R., Touhami, Y. N., & Grundstrom, E. D. 2013, *ApJ*, 765, 2
- Peters, G. J., Wang, L., Gies, D. R., & Grundstrom, E. D. 2016, *ApJ*, 828, 47
- Plaskett, J. S., Harper, W. E., Young, R. K., & Plaskett, H. H. 1920, *Publications of the Dominion Astrophysical Observatory Victoria*, 1, 163
- Plaskett, J. S., & Pearce, J. A. 1931, *Publications of the Dominion Astrophysical Observatory Victoria*, 5, 1
- Pogodin, M. A., Drake, N. A., Jilinski, E. G., Daflon, S., Herencia, M. I. Z., de la Reza, R., & Ortega, V. G. 2012, in *Circumstellar Dynamics at High Resolution*, ASP Conf. Vol. 464, ed. A. C. Carciofi & T. Rivinius (San Francisco, CA: ASP), 227
- Pogodin, M. A., Malanushenko, V. P., Kozlova, O. V., Tarasova, T. N., & Franco, G. A. P. 2006, *A&A*, 452, 551
- Pollmann, E. 2007, *Information Bulletin on Variable Stars*, 5778
- Pols, O. R., Cote, J., Waters, L. B. F. M., & Heise, J. 1991, *A&A*, 241, 419
- Rappaport, S., Nelson, L., Levine, A., Sanchis-Ojeda, R., Gandolfi, D., Nowak, G., Palle, E., & Prsa, A. 2015, *ApJ*, 803, 82
- Reig, P. 2011, *Ap&SS*, 332, 1
- Renson, P., & Manfroid, J. 2009, *A&A*, 498, 961
- Rivinius, T., Carciofi, A. C., & Martayan, C. 2013, *A&A Rev.*, 21, 69
- Rodríguez-Merino, L. H., Chavez, M., Bertone, E., & Buzzoni, A. 2005, *ApJ*, 626, 411
- Ruždjak, D. et al. 2009, *A&A*, 506, 1319

- Saad, S. M. et al. 2005, *Ap&SS*, 296, 173
- Sana, H. et al. 2012, *Science*, 337, 444
- Schootemeijer, A., Götberg, Y., de Mink, S. E., Gies, D., & Zapartas, E. 2018, *A&A*, 615, A30
- Secchi, A. 1866, *Astronomische Nachrichten*, 68, 63
- Shafter, A. W., Szkody, P., & Thorstensen, J. R. 1986, *ApJ*, 308, 765
- Shao, Y., & Li, X.-D. 2014, *ApJ*, 796, 37
- Shatskii, N. I. 1998, *Astronomy Letters*, 24, 257
- Silaj, J., Jones, C. E., Sigut, T. A. A., & Tycner, C. 2014, *ApJ*, 795, 82
- Simón-Díaz, S., & Herrero, A. 2014a, *A&A*, 562, A135
- . 2014b, *A&A*, 562, A135
- Skiff, B. A. 2014, *VizieR Online Data Catalog*, 1
- Slettebak, A. 1982, *ApJS*, 50, 55
- Smith, M. A., Lopes de Oliveira, R., & Motch, C. 2016, *Advances in Space Research*, 58, 782
- Smith, M. A. et al. 2012, *A&A*, 540, A53
- Stee, P. et al. 2012, *A&A*, 545, A59
- Tauris, T. M. et al. 2017, *ApJ*, 846, 170
- Thaller, M. L., Bagnuolo, Jr., W. G., Gies, D. R., & Penny, L. R. 1995, *ApJ*, 448, 878
- Tokovinin, A., Fischer, D. A., Bonati, M., Giguere, M. J., Moore, P., Schwab, C., Spronck, J. F. P., & Szymkowiak, A. 2013, *PASP*, 125, 1336

- Uesugi, A., & Fukuda, I. 1970, Catalogue of rotational velocities of the stars (Kyoto: University of Kyoto)
- Underhill, A., & Doazan, V. 1982, B Stars with and without emission lines (NASA SP-456)
- van Kerkwijk, M. H., Rappaport, S. A., Breton, R. P., Justham, S., Podsiadlowski, P., & Han, Z. 2010, *ApJ*, 715, 51
- van Leeuwen, F. 2007, *A&A*, 474, 653
- van Roestel, J. et al. 2018, *MNRAS*, 475, 2560
- Vanbeveren, D., De Loore, C., & Van Rensbergen, W. 1998, *A&A Rev.*, 9, 63
- Vanbeveren, D., & Mennekens, N. 2017, in *Astronomical Society of the Pacific Conference Series*, Vol. 508, *The B[e] Phenomenon: Forty Years of Studies*, ed. A. Miroshnichenko, S. Zharikov, D. Korčáková, & M. Wolf, 121
- Vieira, R. G., Carciofi, A. C., & Bjorkman, J. E. 2015, *MNRAS*, 454, 2107
- Štefl, S., Hummel, W., & Rivinius, T. 2000, *A&A*, 358, 208
- Wang, K., Luo, C., Zhang, X., Zhang, B., Deng, L., & Luo, Z. 2018a, *AJ*, 156, 187
- Wang, L., Gies, D. R., & Peters, G. J. 2017, *ApJ*, 843, 60
- . 2018b, *ApJ*, 853, 156
- Wang, S.-i. et al. 2003, in *Society of Photo-Optical Instrumentation Engineers (SPIE) Conference Series*, Vol. 4841, *Proc. SPIE*, ed. M. Iye & A. F. M. Moorwood, 1145–1156
- Waters, L. B. F. M., & van Kerkwijk, M. H. 1989, *A&A*, 223, 196
- Yudin, R. V. 2001, *A&A*, 368, 912
- Zhang, X. B., Fu, J. N., Liu, N., Luo, C. Q., & Ren, A. B. 2017, *ApJ*, 850, 125

Zharikov, S. V. et al. 2013, *A&A*, 560, A30

Zizka, E. R., & Beardsley, W. R. 1981, *AJ*, 86, 1944

Zucker, S. 2003, *MNRAS*, 342, 1291

**APPENDIX A**  
**SHELL LINE VARIATIONS IN HR 2142**

Shell line features are shown for absorption lines of S III  $\lambda 1200$ , S II  $\lambda 1250$ , Si II  $\lambda 1260$ , Si II  $\lambda 1264$ , Si III  $\lambda 1299$ , Si II  $\lambda 1304$ , C II  $\lambda 1335$ , Si III  $\lambda 1393$ , Si IV  $\lambda 1402$ , Si II  $\lambda 1526$ , C IV  $\lambda\lambda 1548, 1550$ , Al II  $\lambda 1670$ , Al III  $\lambda 1854$ , Al III  $\lambda 1862$ , Fe III  $\lambda 1895$ , Mg II  $\lambda 2796$ , and Mg II  $\lambda 2803$ .

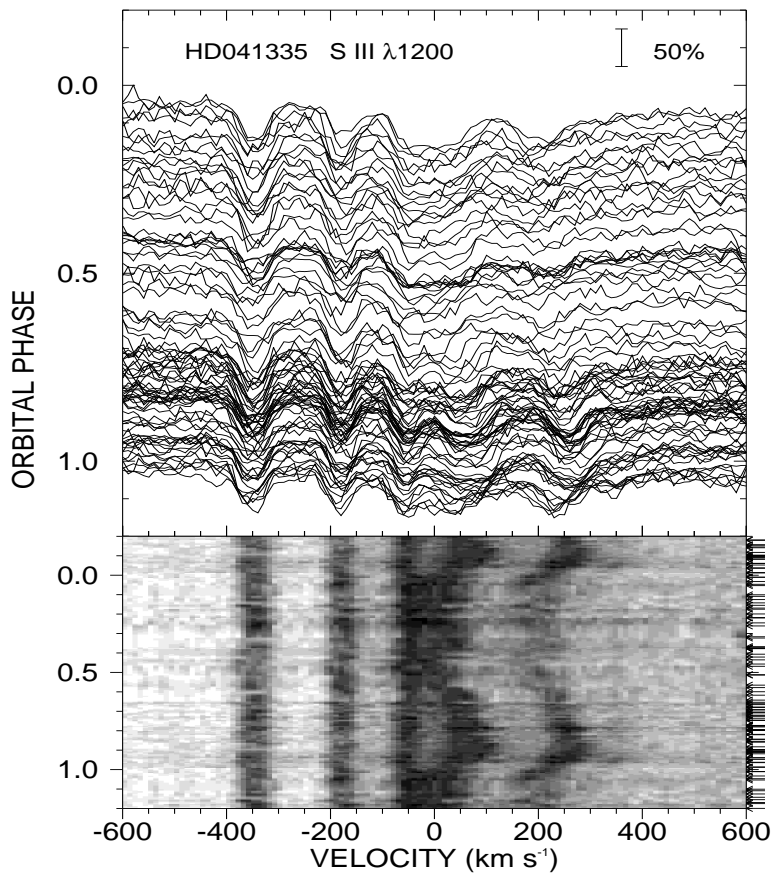


Figure A.1: The top panel displays the individual spectra of S III  $\lambda 1200$  against the velocity, with each spectrum offset by its orbital phase. The depth of the absorption features relative to the continuum is shown by the scale on the upper right of the figure. The bottom panels showed the sample spectra interpreted in a gray scale format between deepest absorption (black) and maximum spectra flux (white). This line profile shows the complete shell line variations, which appear at  $\phi = 0.5$ , and they gradually develop strength and reach maximum near  $\phi = 0.95$ . Right after  $\phi = 0.0$ , the shell line features display a short-lived, blue-shifted component.

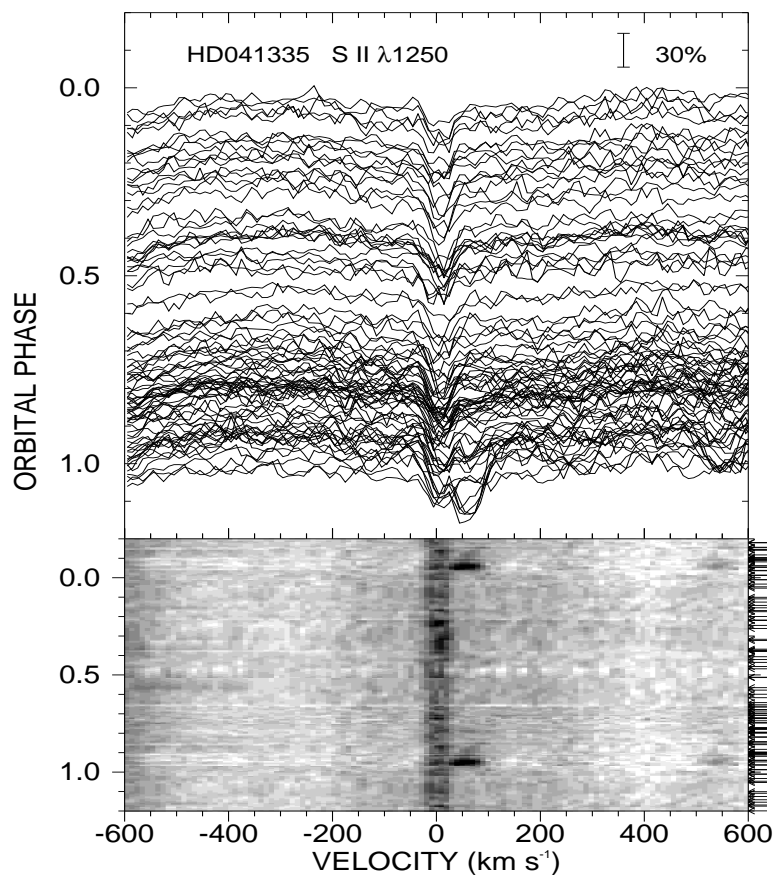


Figure A.2: The top panel displays the individual spectra of S II  $\lambda 1250$  against the velocity, with each spectrum offset by its orbital phase. The depth of the absorption features relative to the continuum is shown by the scale on the upper right of the figure. The bottom panels showed the sample spectra interpreted in a gray scale format between deepest absorption (black) and maximum spectra flux (white). This line profile shows the partial shell line variations, and only the primary shell line feature near  $\phi = 0.95$  is displayed.

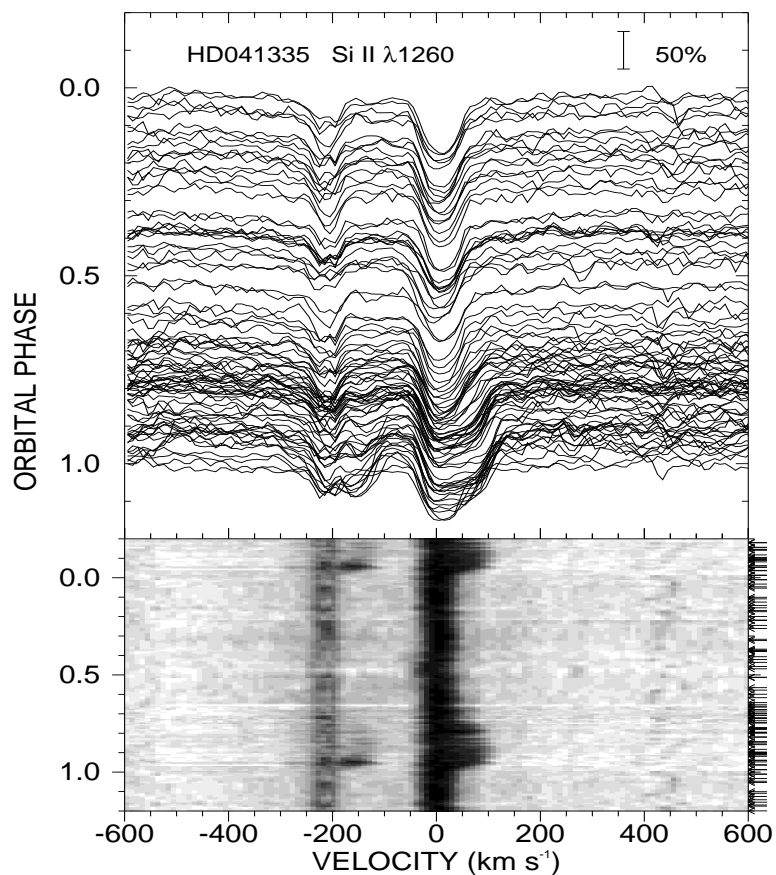


Figure A.3: The top panel displays the individual spectra of Si II  $\lambda 1260$  against the velocity, with each spectrum offset by its orbital phase. The depth of the absorption features relative to the continuum is shown by the scale on the upper right of the figure. The bottom panels showed the sample spectra interpreted in a gray scale format between deepest absorption (black) and maximum spectra flux (white). This line profile shows the partial shell line variations, and only the primary shell line feature near  $\phi = 0.95$  is displayed.

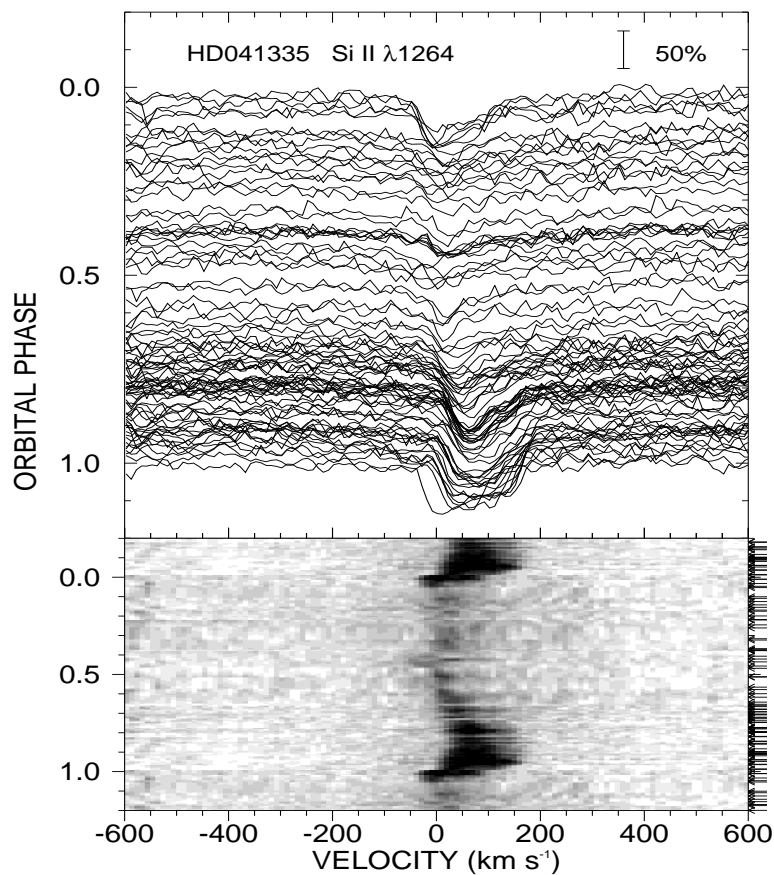


Figure A.4: The top panel displays the individual spectra of Si II  $\lambda 1264$  against the velocity, with each spectrum offset by its orbital phase. The depth of the absorption features relative to the continuum is shown by the scale on the upper right of the figure. The bottom panels showed the sample spectra interpreted in a gray scale format between deepest absorption (black) and maximum spectra flux (white). This line profile shows the complete shell line variations, which appear at  $\phi = 0.5$ , and they gradually develop strength and reach maximum near  $\phi = 0.95$ . Right after  $\phi = 0.0$ , the shell line features display a short-lived, blue-shifted component.

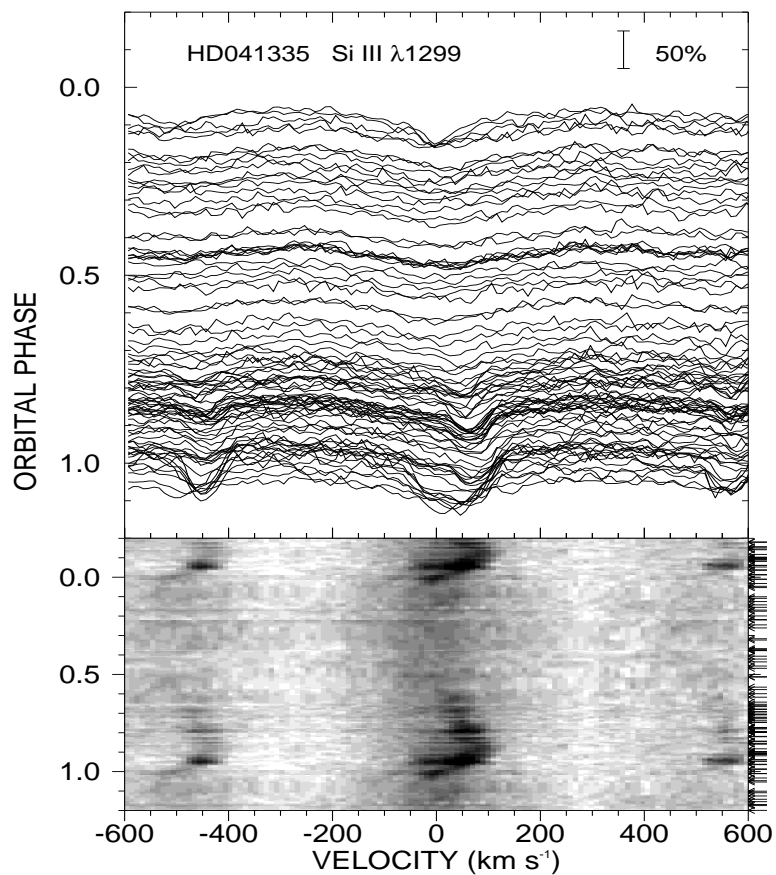


Figure A.5: The top panel displays the individual spectra of Si III  $\lambda 1299$  against the velocity, with each spectrum offset by its orbital phase. The depth of the absorption features relative to the continuum is shown by the scale on the upper right of the figure. The bottom panels showed the sample spectra interpreted in a gray scale format between deepest absorption (black) and maximum spectra flux (white). This line profile shows the complete shell line variations, which appear at  $\phi = 0.5$ , and they gradually develop strength and reach maximum near  $\phi = 0.95$ . Right after  $\phi = 0.0$ , the shell line features display a short-lived, blue-shifted component.

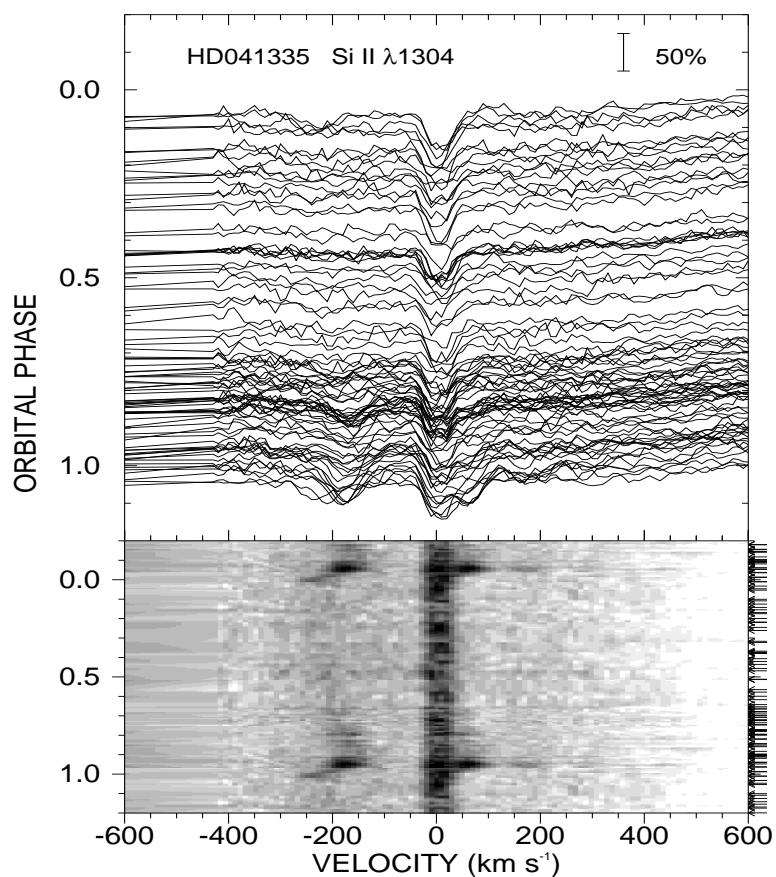


Figure A.6: The top panel displays the individual spectra of Si II  $\lambda 1304$  against the velocity, with each spectrum offset by its orbital phase. The depth of the absorption features relative to the continuum is shown by the scale on the upper right of the figure. The bottom panels showed the sample spectra interpreted in a gray scale format between deepest absorption (black) and maximum spectra flux (white). This line profile shows the partial shell line variations, and only the primary shell line feature near  $\phi = 0.95$  is displayed.

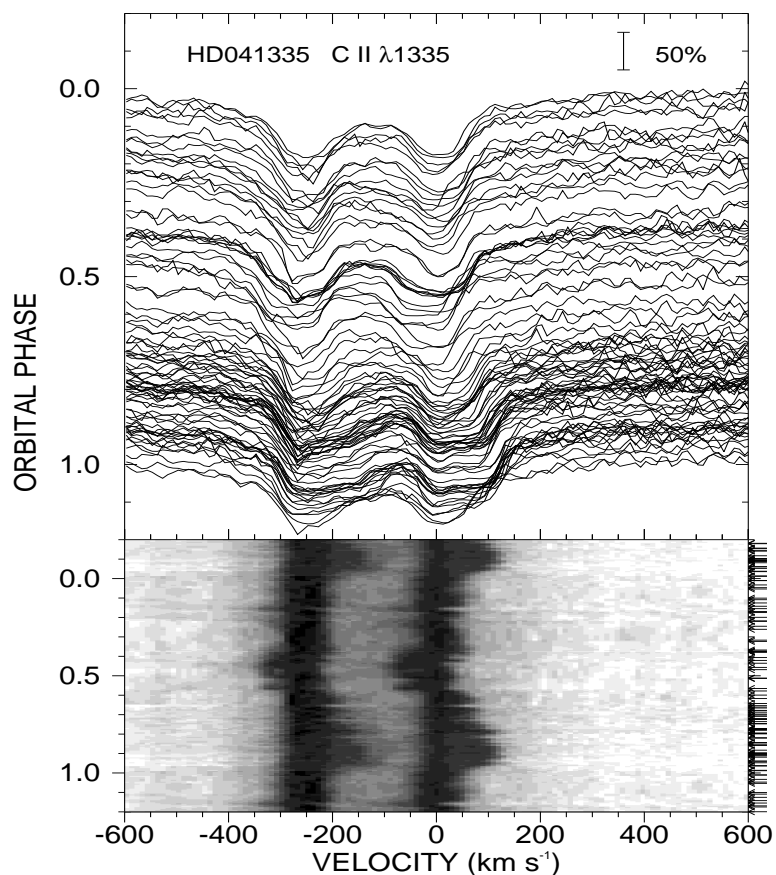


Figure A.7: The top panel displays the individual spectra of C II  $\lambda 1334,1335$  against the velocity, with each spectrum offset by its orbital phase. The depth of the absorption features relative to the continuum is shown by the scale on the upper right of the figure. The bottom panels showed the sample spectra interpreted in a gray scale format between deepest absorption (black) and maximum spectra flux (white). This line profile shows shell line variations for both blueshifts near  $\phi = 0.5$  (Be star is at inferior conjunction relative to the observer), and extreme redshifts near  $\phi = 0.95$ .

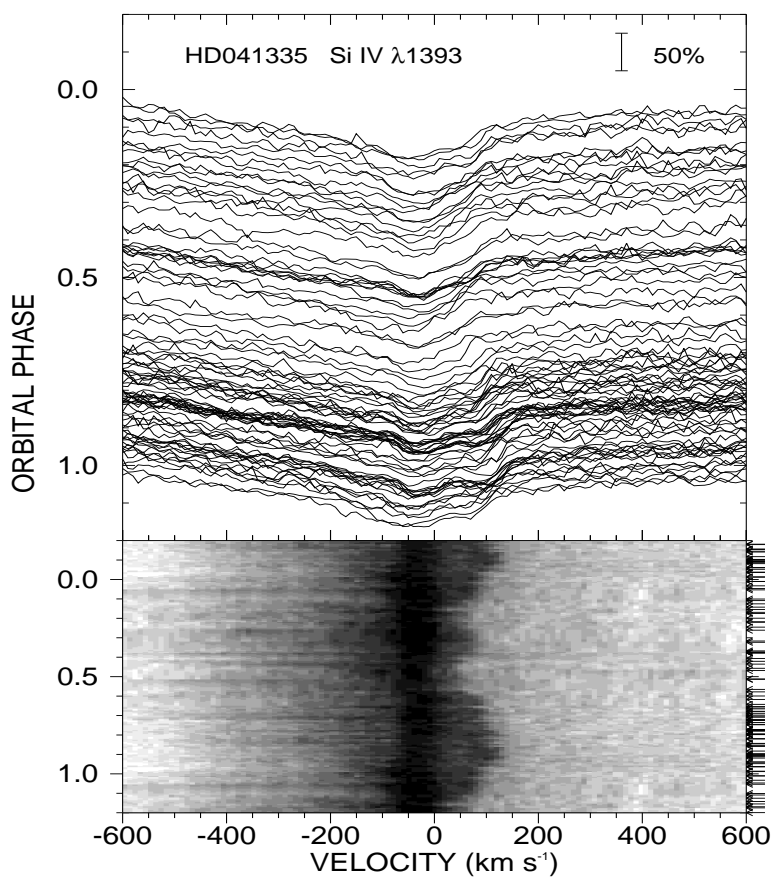


Figure A.8: The top panel displays the individual spectra of Si IV  $\lambda 1393$  against the velocity, with each spectrum offset by its orbital phase. The depth of the absorption features relative to the continuum is shown by the scale on the upper right of the figure. The bottom panels showed the sample spectra interpreted in a gray scale format between deepest absorption (black) and maximum spectra flux (white). This line profile shows the stellar wind features of the Be star, and the signature of primary absorption shell line features appear near  $\phi = 0.6 - 1.0$ .

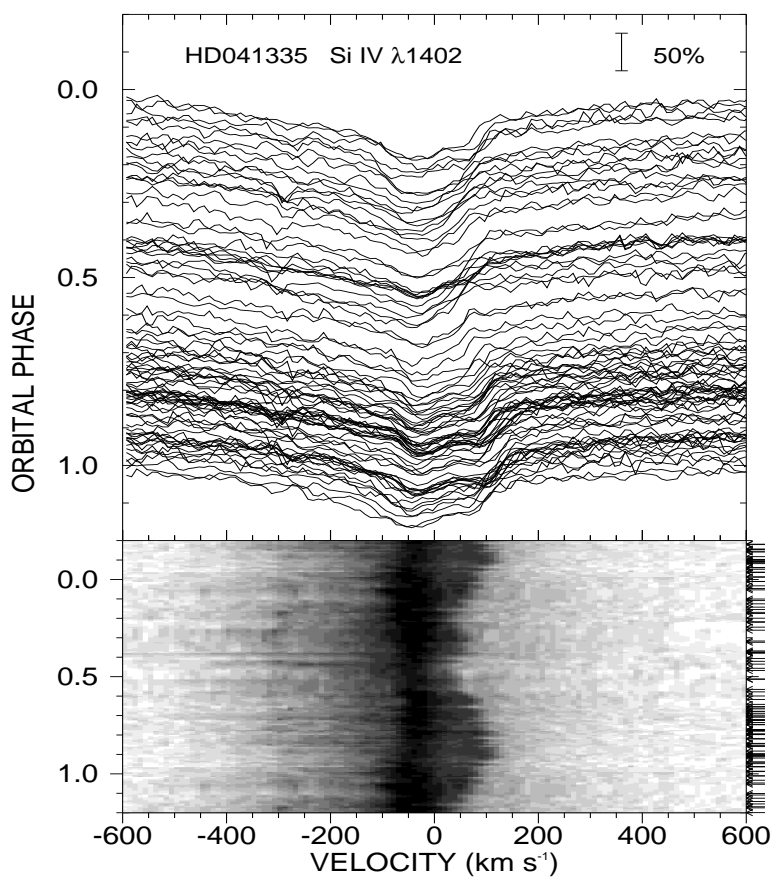


Figure A.9: The top panel displays the individual spectra of Si IV  $\lambda 1402$  against the velocity, with each spectrum offset by its orbital phase. The depth of the absorption features relative to the continuum is shown by the scale on the upper right of the figure. The bottom panels showed the sample spectra interpreted in a gray scale format between deepest absorption (black) and maximum spectra flux (white). This line profile shows the stellar wind features of the Be star, and the signature of primary absorption shell line features appear near  $\phi = 0.6 - 1.0$

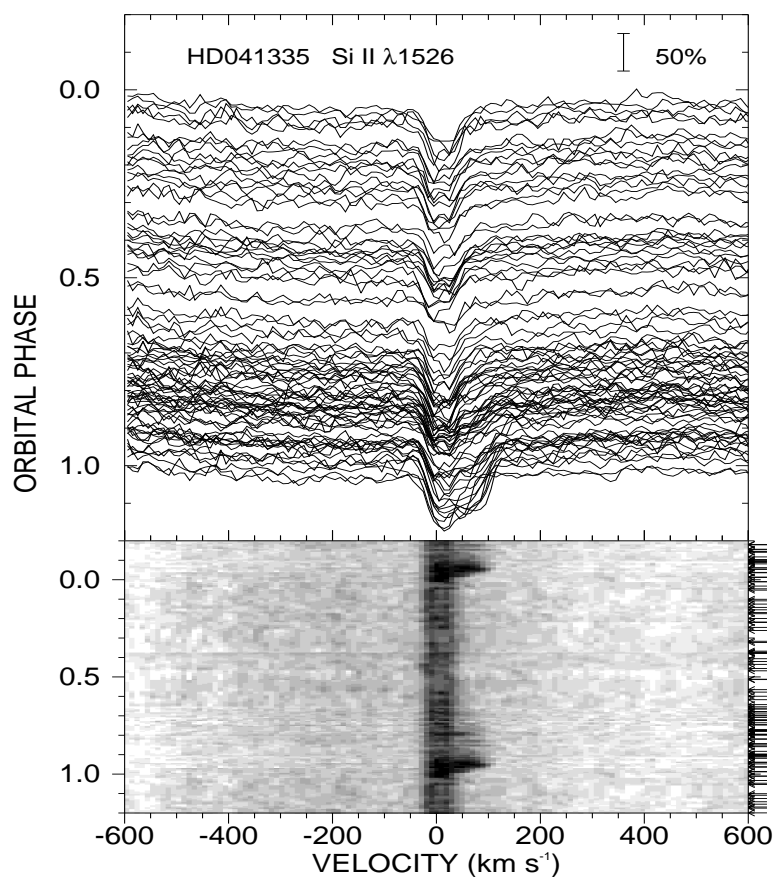


Figure A.10: The top panel displays the individual spectra of Si II  $\lambda 1526$  against the velocity, with each spectrum offset by its orbital phase. The depth of the absorption features relative to the continuum is shown by the scale on the upper right of the figure. The bottom panels showed the sample spectra interpreted in a gray scale format between deepest absorption (black) and maximum spectra flux (white). This line profile shows the partial shell line variations, and only the primary shell line feature near  $\phi = 0.95$  is displayed.

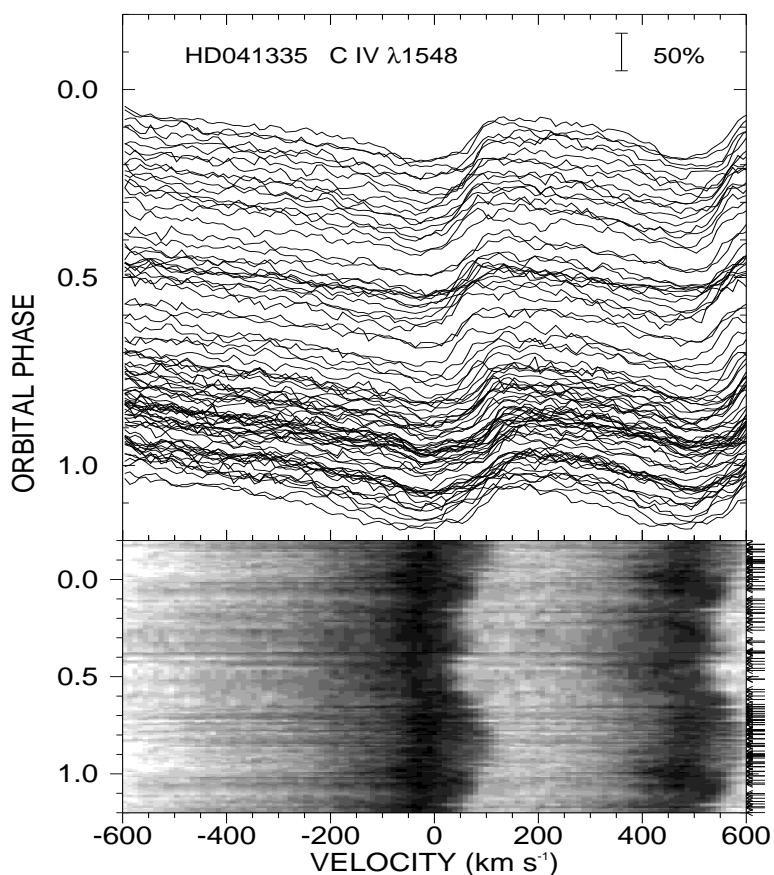


Figure A.11: The top panel displays the individual spectra of C IV  $\lambda 1548, 1550$  against the velocity, with each spectrum offset by its orbital phase. The depth of the absorption features relative to the continuum is shown by the scale on the upper right of the figure. The bottom panels showed the sample spectra interpreted in a gray scale format between deepest absorption (black) and maximum spectra flux (white). This line profile shows the stellar wind features of the Be star, the signature of primary absorption shell line features appear near  $\phi = 0.6 - 1.0$ , and blue-shifted absorption features appear near  $\phi = 0.5$ .

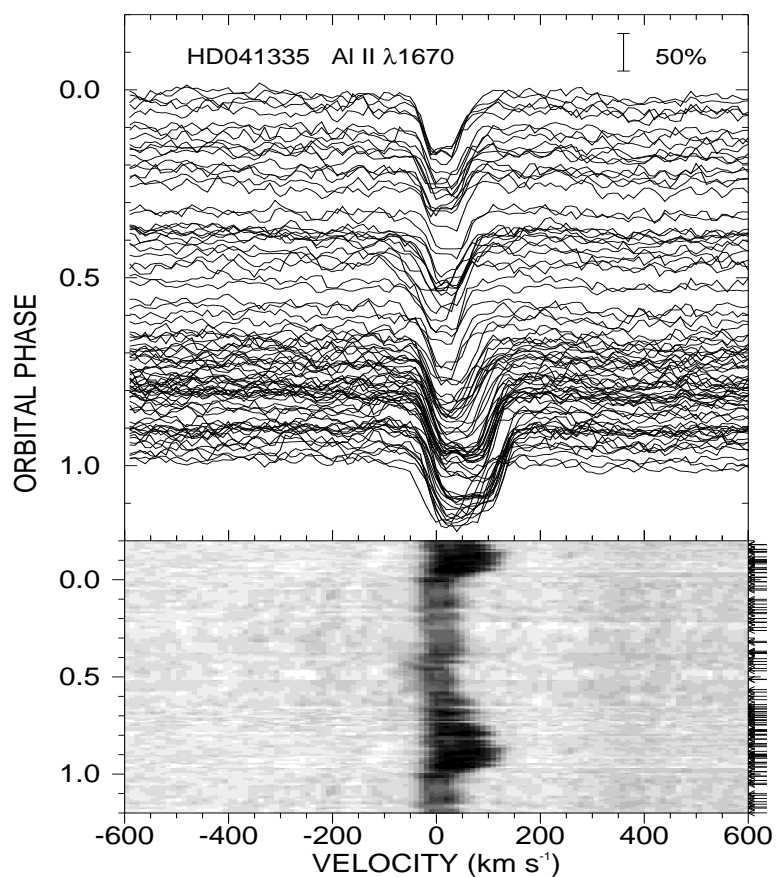


Figure A.12: The top panel displays the individual spectra of Al II  $\lambda 1670$  against the velocity, with each spectrum offset by its orbital phase. The depth of the absorption features relative to the continuum is shown by the scale on the upper right of the figure. The bottom panels showed the sample spectra interpreted in a gray scale format between deepest absorption (black) and maximum spectra flux (white). This line profile shows the partial shell line variations, and only the primary shell line feature near  $\phi = 0.95$  is displayed.

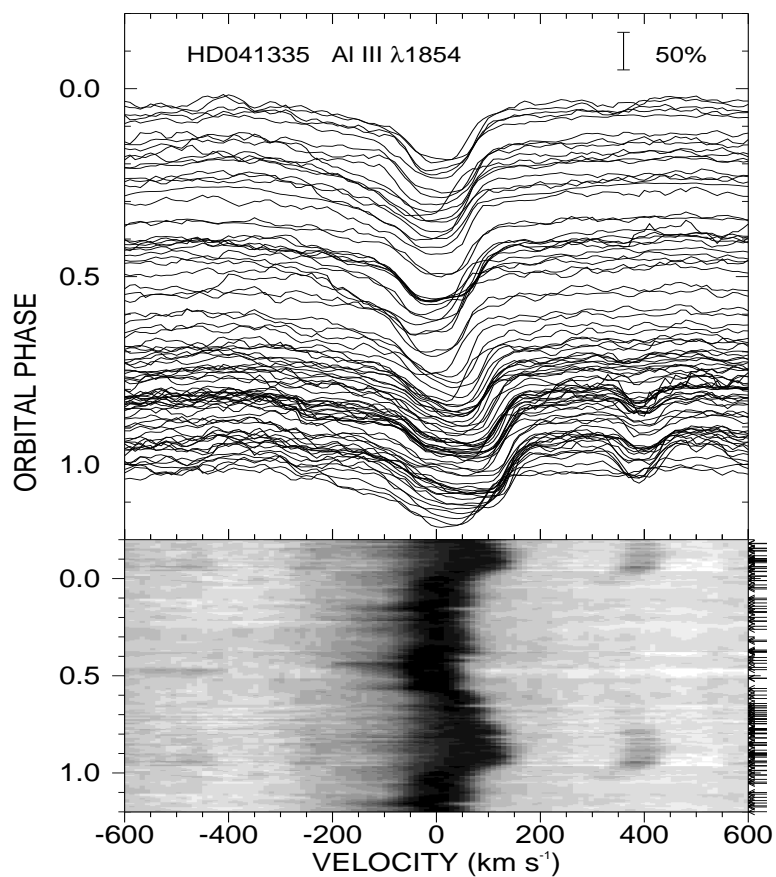


Figure A.13: The top panel displays the individual spectra of Al III  $\lambda 1854$  against the velocity, with each spectrum offset by its orbital phase. The depth of the absorption features relative to the continuum is shown by the scale on the upper right of the figure. The bottom panels showed the sample spectra interpreted in a gray scale format between deepest absorption (black) and maximum spectra flux (white). This line profile shows shell line variations for both blueshifts near  $\phi = 0.5$  (Be star is at inferior conjunction relative to the observer), and extreme redshifts near  $\phi = 0.95$ .

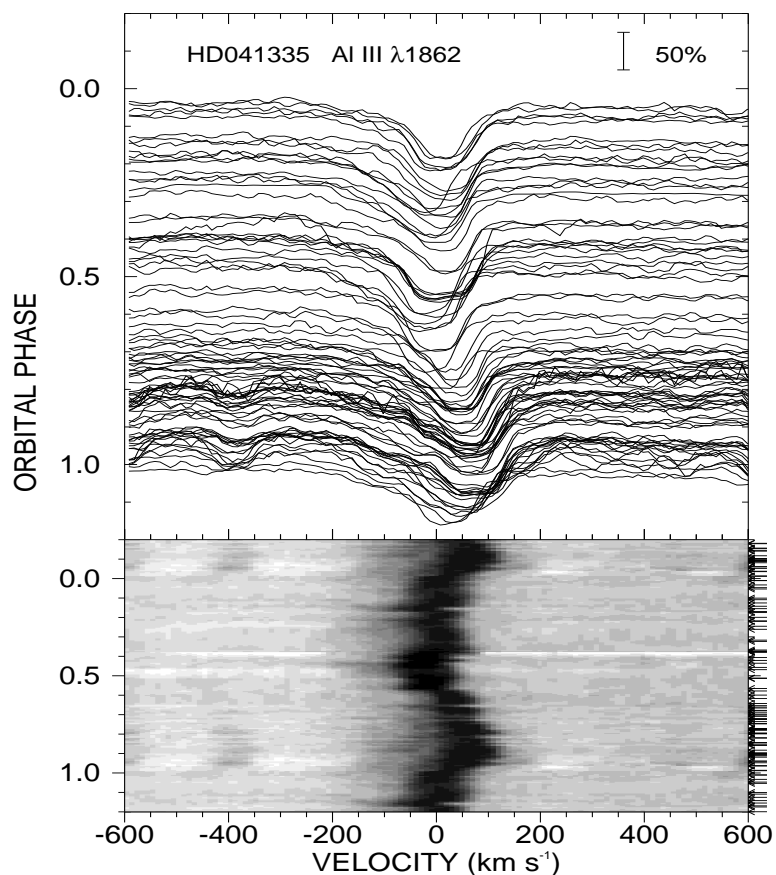


Figure A.14: The top panel displays the individual spectra of Al III  $\lambda 1862$  against the velocity, with each spectrum offset by its orbital phase. The depth of the absorption features relative to the continuum is shown by the scale on the upper right of the figure. The bottom panels showed the sample spectra interpreted in a gray scale format between deepest absorption (black) and maximum spectra flux (white). This line profile shows shell line variations for both blueshifts near  $\phi = 0.5$  (Be star is at inferior conjunction relative to the observer), and extreme redshifts near  $\phi = 0.95$ .

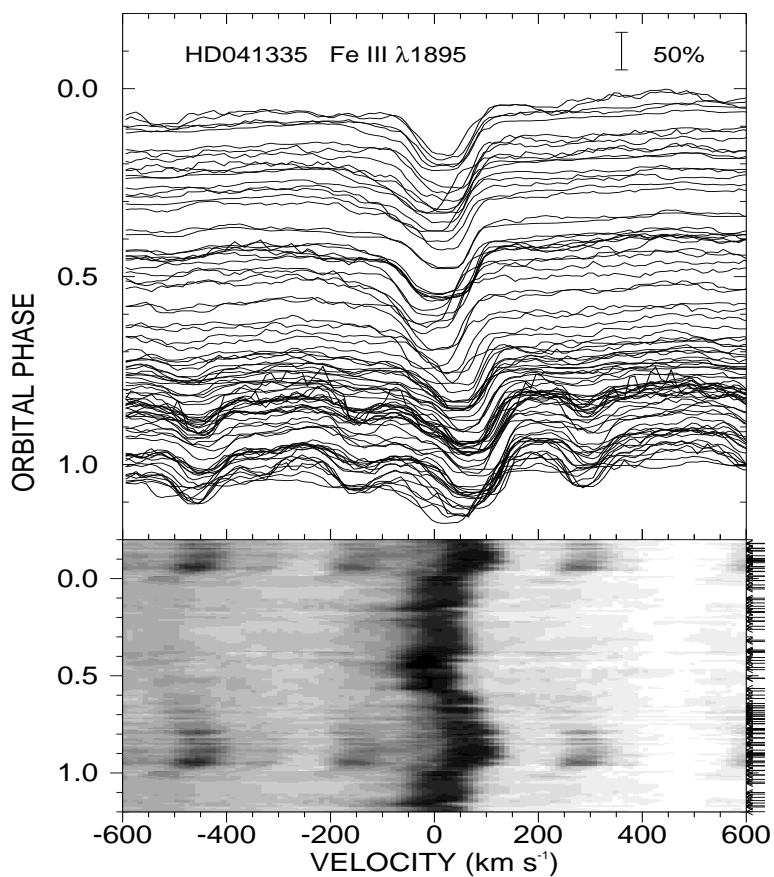


Figure A.15: The top panel displays the individual spectra of Fe III  $\lambda 1895$  against the velocity, with each spectrum offset by its orbital phase. The depth of the absorption features relative to the continuum is shown by the scale on the upper right of the figure. The bottom panels showed the sample spectra interpreted in a gray scale format between deepest absorption (black) and maximum spectra flux (white). This line profile shows shell line variations for both blueshifts near  $\phi = 0.5$  (Be star is at inferior conjunction relative to the observer), and extreme redshifts near  $\phi = 0.95$ .

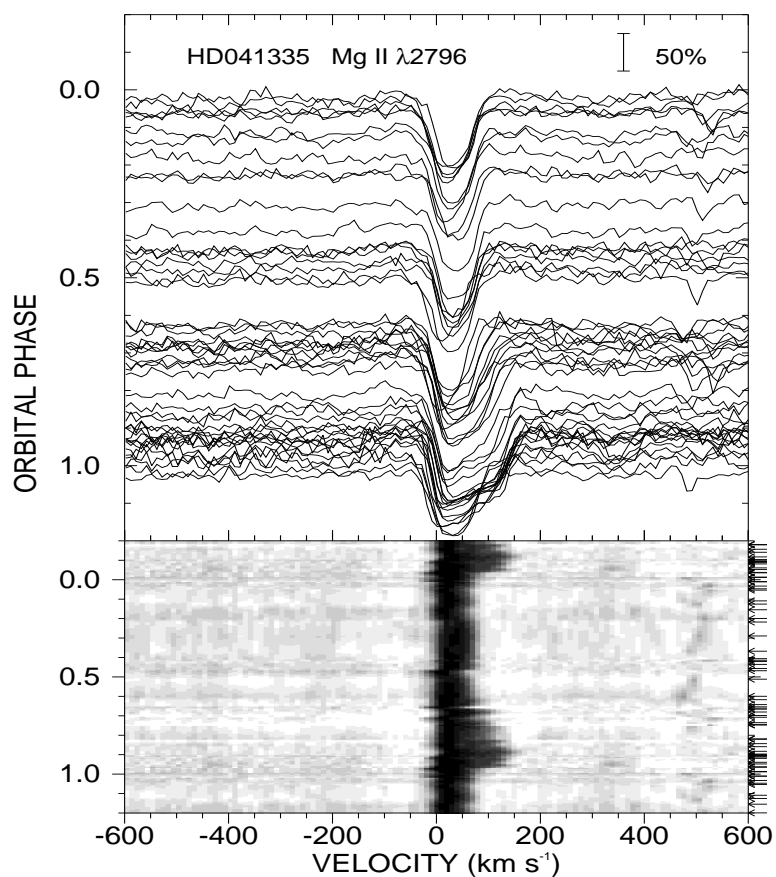


Figure A.16: The top panel displays the individual spectra of Mg II  $\lambda 2796$  against the velocity, with each spectrum offset by its orbital phase. The depth of the absorption features relative to the continuum is shown by the scale on the upper right of the figure. The bottom panels showed the sample spectra interpreted in a gray scale format between deepest absorption (black) and maximum spectra flux (white). This line profile shows the partial shell line variations, and only the primary shell line feature near  $\phi = 0.95$  is displayed.

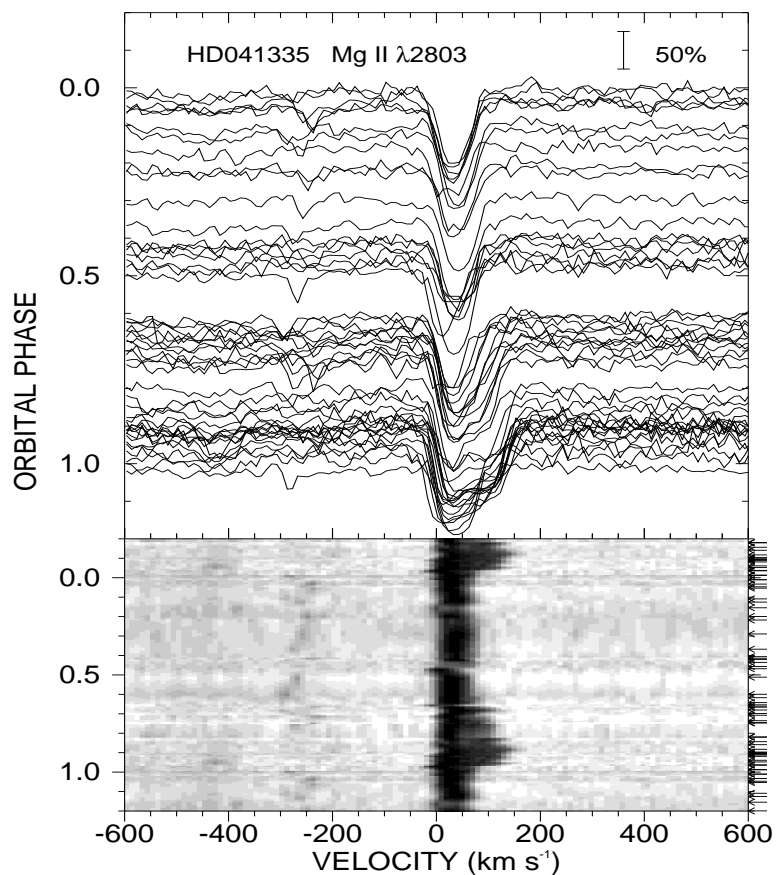


Figure A.17: The top panel displays the individual spectra of Mg II  $\lambda 2803$  against the velocity, with each spectrum offset by its orbital phase. The depth of the absorption features relative to the continuum is shown by the scale on the upper right of the figure. The bottom panels showed the sample spectra interpreted in a gray scale format between deepest absorption (black) and maximum spectra flux (white). This line profile shows the partial shell line variations, and only the primary shell line feature near  $\phi = 0.95$  is displayed.

## APPENDIX B

### SHELL EPISODE OF PLEIONE

Pleione shows long term variations in brightness and color during the B, Be, and Be-shell phase transitions. During a shell phase the optical spectrum of hydrogen and metallic lines show narrow absorption cores with significant growth in line strength, and these spectral variations probably result from physical changes in the circumstellar disk as projected against the photosphere of the star. Cramer et al. (1995) summarized the light variations of Pleione from 1880 to 1993 through optical photometry, and they documented how the  $B$ -magnitude of Pleione changed during the shell episode from 1973 to 1993. A significant drop in brightness occurred prior to the shell phase in 1973, and then the star's brightness gradually increased as the shell lines faded and Pleione returned to the Be phase. Doazan et al. (1988) investigated the spectral variability of the metallic lines in far-UV during this time, and Doazan et al. (1993) showed how the energy flux between 1250 and 3000 Å varied from 1979 to 1991. The full set of *IUE* spectra record the shell line changes from 1979 to 1995, and I plot the average flux of Pleione in the UV from 1160 to 1450 Å in Figure B.1 (top panel). The average UV flux dropped significantly after 1979, reached a minimum in 1982, and then slowly increased back to the average level. The three low flux measurements (1980 – 1982) were recorded through the small aperture of the camera, which may underestimate the actual flux. Nevertheless, a similar local minimum was also recorded at the same time in the  $B$ -band photometry from Cramer et al. (1995). There are shell lines in the UV spectra that are very narrow and that are the same ionic species as observed in cooler objects like A-type

stars. Thus, I measured the strength of shell lines of Pleione by calculating CCFs with a star that has a line spectrum similar to the shell features. I adopted the supergiant star HD 197345 (Deneb, A2Ia) to cross-correlate with the spectrum of Pleione, and shell line regions including 1450 – 1500 Å, 1510 – 1583 Å, 1650 – 1700 Å, and 1828 – 1875 Å were chosen to calculate the CCFs. In Figure B.1, the middle panel shows how the shell line strength decreased as the star brightened. I also calculated the relative radial velocity of the shell lines from the peak position of CCFs with the Deneb spectrum. Parthasarathy & Lambert (1987) reported that Deneb has a mean radial velocity of  $-13.67 \text{ km s}^{-1}$ , so I added this velocity to the CCF relative velocities to obtain the absolute radial velocities of the shell lines that are plotted in bottom panel of Figure B.1. The shell line velocities appear to become more negative relative to Pleione (systemic velocity of  $-0.15 \text{ km s}^{-1}$  from Nemravová et al. 2010) as the shell episode declines. However, near the final stage of the shell episode, the CCFs are weak, so the measured velocities have large uncertainties. Our results are consistent with those reported by Underhill & Doazan (1982) in their Figure 11–43, which show that the velocities have greatest expansion at the epoch of shell line disappearance. The shell line spectra show significant blue-shifts during the Be-shell to Be phase transition, and the negative velocities suggest that the opaque gas associated with the shell lines moves away from the star as the shell episode concludes.

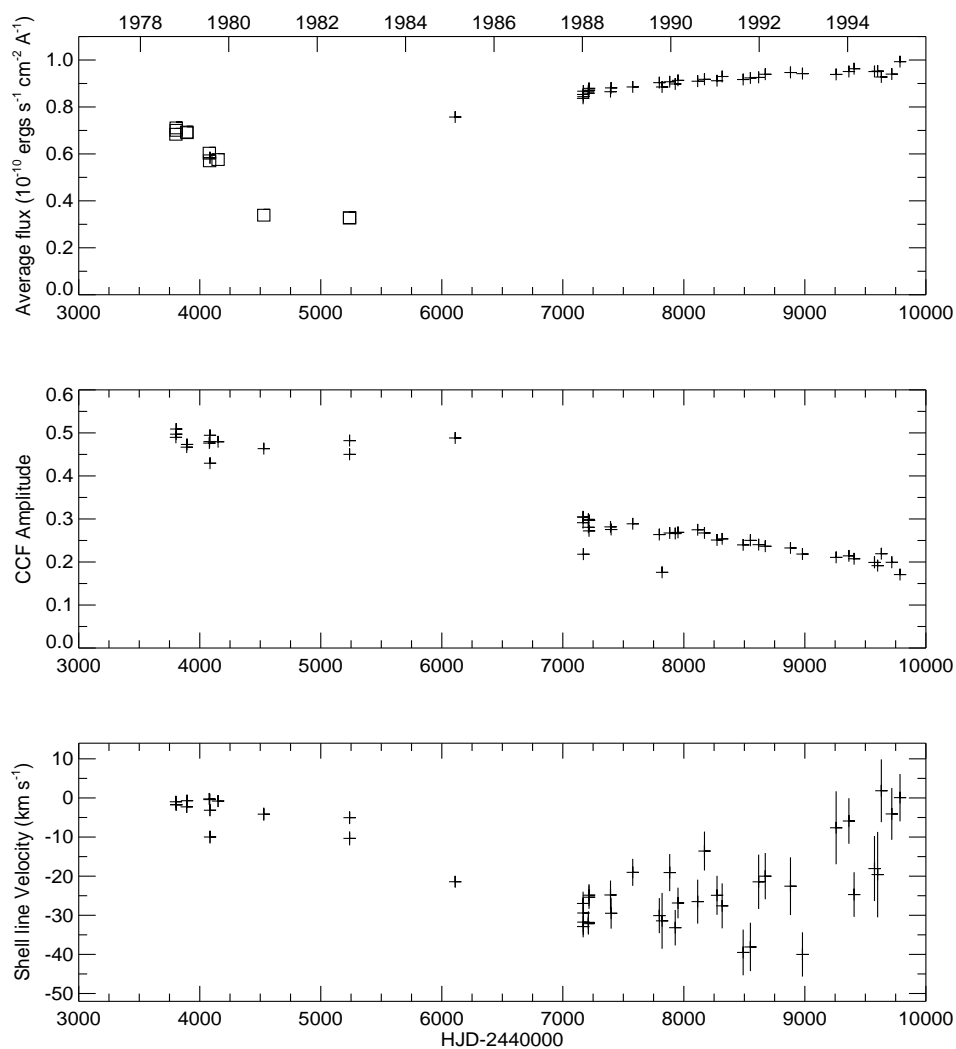


Figure B.1: The shell line variations of Pleione in UV from 1979 to 1995. *Top panel:* the average flux is computed in the wavelength region  $[1160, 1450]$   $\text{\AA}$ ; spectra recorded in large and small apertures are denoted as crosses and squares, respectively. *Middle panel:* cross-correlation strength between the spectra of Pleione and supergiant star Deneb. *Bottom panel:* absolute radial velocities from the cross-correlation functions of the shell lines.

## APPENDIX C

NOTES ON INDIVIDUAL STARS IN THE *IUE* SUBDWARF SURVEY

**HD 35411 ( $\eta$  Ori; B1 IV).** Zizka & Beardsley (1981) measured the spectroscopic radial velocities of the inner binary system and concluded that the Aa1, Aa2 pair has an orbital period of 7.989 d. The first speckle measurements done by McAlister (1976) showed that there is a third star (B3 IV) that orbits around the inner eclipsing and spectroscopic binary system Aa1, Aa2 (B1 IV and B3 IV, respectively) in an orbit with an angular semimajor axis of 44 mas and a period of 9.2 yr. The *IUE* spectra recorded the flux of all three components. The cross-correlation functions of the spectra show a sharp peak, and the peak half-width is comparable to the projected rotational velocity of Aa1. Furthermore, the measured CCF peak velocities appear to match the Aa1 radial velocity curve from De Mey et al. (1996) in their Figure 3. Thus, I conclude that the CCF peaks result from correlation with the spectral features of the primary Aa1 component of the inner binary system.

**HD 53367 (V750 Mon; B0 IVe).** Based on spectroscopic studies of the optical lines, Pogodin et al. (2006) proposed that the system consists of a primary main-sequence star ( $\sim 20M_{\odot}$ ) and a pre-main sequence secondary ( $\sim 5 M_{\odot}$ ). I compared the measured peak velocities with the primary radial velocity curve in Figure 6 of Pogodin et al. (2006), and the similarity of the velocities suggests that the CCF peak is mostly due to correlation with the spectral features of the primary component. However, I noticed that two spectra (SWP38685 and SWP38686) yielded a peak velocity variation of  $\sim 50 \text{ km s}^{-1}$  in less than 3 hours. I examined the spectra and found that the star drifted in position across the dispersion in

the large aperture of the camera between exposures. Thus, this rapid velocity variation is instrumental in origin.

**HD 135160 (B0 IV).** The CCFs show both a sharp peak and an extended wing feature that varies in velocity. Chini et al. (2012) detected spectral lines of both components of this suspected spectroscopic binary. The Doppler shifts apparent in the CCFs tend to confirm the spectroscopic binary nature of the system.

**HD 166596 (V692 CrA; B2.5 IIIp).** *IUE* recorded two spectra of this star within  $\sim 1$  hour. The peak velocities of the CCFs indicate a significant shift of  $\sim 37 \text{ km s}^{-1}$  between the observations. Renson & Manfroid (2009) report that the target is a silicon star with a rotational period of  $\sim 1.7$  d. I suggest that the rapid velocity variation is probably related to rotational Doppler shifts of regions with chemical peculiarities.

**HD 178175 (V4024 Sgr; B2 IV(e)).** The CCFs show a sharp peak. Based on spectroscopic studies, Bragança et al. (2012) reported that the star has  $V \sin i = 86 \text{ km s}^{-1}$ , similar to the half-width of the CCF peak. However, Bragança et al. (2012) estimate that the star's temperature is  $T_{\text{eff}} = 19.6 \text{ kK}$ , and I would usually expect little correlation with the features of such a relatively cooler object. However, the CCFs show no significant peak velocity variations. Thus, I conclude that the CCFs are most likely due to correlation with the features of the Be star that are narrow enough in this case to produce a detectable CCF peak.